

Assessment of Residual Strength of Corrosion Damaged  
Concrete Structures

Sallehuddin Shah Ayop

Submitted for the degree of Doctor of Philosophy

Heriot-Watt University

School of the Energy, Geoscience, Infrastructure and Society

April 2017

The copyright in this thesis is owned by the author. Any quotation from the thesis or use of any of the information contained in it must acknowledge this thesis as the source of the quotation or information.

## **ABSTRACT**

The corrosion of steel reinforcement in concrete is one of the major problems with respect to the durability of reinforced concrete structures. In addition, the residual strength of concrete with corroded reinforcement is much debated. This is because many parameters are implicated when assessing reinforcement corrosion, such as by using the percentage of loss of bar area, percentage of mass loss, reduction of bar radius, percentage of corroded area in the overall beam, and the width of the surface crack. The aim of the current study is to integrate correlations between deterioration and strength degradation into a systematic methodology for estimation of the residual strength of concrete structures based on their serviceability limit state. In the numerical analysis, the objective is to understand the effects of corrosion expansion on the behaviour of surface crack width. Results from the numerical study are used to determine parameters for the experimental investigation. The experimental approach is used to assess the influence of corrosion parameters, which are quantified as a percentage of the section loss, radius loss or corrosion penetration, and crack width on the residual bond strength based on different bar locations, casting positions, and impressed currents. Results from the experimental analyses show that the corrosion level on the main reinforcing bar in this study cannot be used as an indicator in assessing the residual bond strength due to many factors consideration during the assessment. However, corrosion-induced crack width on the bottom cast correlated well with residual bond strength. When crack width increased, most of the bar had a lower residual bond strength value.

## **ACKNOWLEDGEMENT**

First of all the author would like to express his highest praise to Allah the Almighty for His merciful and kindnesses, therefore the author can complete this thesis in a given time.

The author would like to express his sincere thanks to his supervisor, Prof. Dimitri Val for his helpful guidance on numerical study, thesis writing and corrections. Special thanks are also goes to Dr. John Cairns for his help, guidance and advice throughout this research and thesis writing.

The author also wants to express his gratitude to his sponsor, Ministry of Higher Education, Malaysia and for research funds and allowances. A sincere gratitude is also due to his employer, Universiti Tun Hussein Onn, Malaysia for approved of his study leaves to do this research. Thank you very much for the support.

Special thanks to all technicians involved in his experimental work, especially Bill Hodder, Alaistair MacFarlane, Greame Sorley, Tom Stenhouse, Gordon Strong and David Murray. The support of I.T. department staff and administration staff in the School of the Energy, Geoscience, Infrastructure and Society's office is also knowledge.

Finally to his wife, Azmahani Sadikin, children; Iman Naufal, Marissa and Hannan; to my parents Hj Ayop Bin Mohd Yusop, Hjh Mariah Binti Hj Nordin and to all family members for their patience, generous support and encouragements during his study.

ACADEMIC REGISTRY  
**Research Thesis Submission**




Name:	Sallehuddin Shah Bin Ayop		
School:	School of Energy, Geoscience, Infrastructure and Society		
Version: <i>(i.e. First, Resubmission, Final)</i>	Final	Degree Sought:	PhD

**Declaration**

In accordance with the appropriate regulations I hereby submit my thesis and I declare that:

- 1) the thesis embodies the results of my own work and has been composed by myself
- 2) where appropriate, I have made acknowledgement of the work of others and have made reference to work carried out in collaboration with other persons
- 3) the thesis is the correct version of the thesis for submission and is the same version as any electronic versions submitted\*.
- 4) my thesis for the award referred to, deposited in the Heriot-Watt University Library, should be made available for loan or photocopying and be available via the Institutional Repository, subject to such conditions as the Librarian may require
- 5) I understand that as a student of the University I am required to abide by the Regulations of the University and to conform to its discipline.
- 6) I confirm that the thesis has been verified against plagiarism via an approved plagiarism detection application e.g. Turnitin.

\* *Please note that it is the responsibility of the candidate to ensure that the correct version of the thesis is submitted.*

Signature of Candidate:		Date:	20 APRIL 2017
-------------------------	---	-------	---------------

**Submission**

Submitted By <i>(name in capitals)</i> :	
Signature of Individual Submitting:	
Date Submitted:	

**For Completion in the Student Service Centre (SSC)**

Received in the SSC by <i>(name in capitals)</i> :			
Method of Submission <i>(Handed in to SSC; posted through internal/external mail):</i>			
E-thesis Submitted ( <b>mandatory for final theses</b> )			
Signature:		Date:	

# TABLE OF CONTENTS

Abstract	i
Acknowledgement	ii
Declaration	iii
Contents	iv
List of tables	viii
List of figures	ix
Notation	xii
<b>CHAPTER 1 – INTRODUCTION</b>	<b>1</b>
<b>1.1 Background of Problem</b>	<b>1</b>
<b>1.2 Aim and Objectives of Research</b>	<b>2</b>
<b>1.3 References</b>	<b>3</b>
<b>CHAPTER 2 – LITERATURE REVIEW</b>	<b>4</b>
<b>2.1 Basic Mechanism of Corrosion of Reinforcement</b>	<b>4</b>
<i>2.1.1 Initiation stage</i>	<i>5</i>
<i>2.1.2 Activation stage</i>	<i>5</i>
<i>2.1.3 Deterioration stage</i>	<i>7</i>
<b>2.2 Bond Behaviour of Ribbed Bar – General Description</b>	<b>7</b>
<i>2.2.1 Bond test methods</i>	<i>9</i>
<b>2.3 Accelerated Corrosion</b>	<b>13</b>
<i>2.3.1 Technique</i>	<i>13</i>
<i>2.3.2 Corrosion Quantification</i>	<i>19</i>
<b>2.4 Structural Effects of Corrosion</b>	<b>19</b>
<i>2.4.1 Loss of bar section</i>	<i>20</i>
<i>2.4.2 Loss of bond</i>	<i>21</i>
<i>2.4.3 Loss of concrete section</i>	<i>26</i>
<b>2.5 Corrosion-induced Surface Crack</b>	<b>27</b>
<b>2.6 Conclusions</b>	<b>30</b>
<b>2.7 References</b>	<b>32</b>

<b>CHAPTER 3 – NUMERICAL ANALYSIS OF CORROSION-INDUCED CRACKING</b>	38
<b>3.1 Introduction</b>	38
<b>3.2 Review of previous study</b>	38
<i>3.2.1 Corrosion-induced crack model</i>	38
<i>3.2.2 Corrosion modelling</i>	41
<i>3.2.3 Penetration of corrosion products into concrete pores and cracks</i>	43
<i>3.2.4 Crack modelling</i>	44
<i>3.2.5 Material properties</i>	44
<i>3.2.6 Conclusion</i>	46
<b>3.3 Numerical Model Procedure</b>	46
<i>3.3.1 Steel reinforcement and concrete materials properties</i>	47
<i>3.3.2 Crack representation</i>	49
<i>3.3.3 Interface properties</i>	50
<i>3.3.3.1 Crack interface</i>	50
<i>3.3.3.2 Friction interface</i>	52
<i>3.3.4 Loading condition</i>	53
<i>3.3.5 Mesh configuration</i>	54
<i>3.3.6 Nonlinear analysis procedure</i>	57
<b>3.4 Presentation of Numerical Results</b>	58
<i>3.4.1 Expansion of bar radius</i>	58
<i>3.4.2 Crack location</i>	59
<b>3.5 Results and Discussion</b>	62
<i>3.5.1 Crack propagation</i>	62
<b>3.6 Summary of Numerical Results</b>	66
<b>3.7 Corrosion Crack Analysis on Multiple Reinforcement</b>	66
<i>3.7.1 Model selection</i>	66
<i>3.7.2 Corner bar location</i>	67
<i>3.7.3 Combined centre and corner bar location</i>	68
<i>3.7.4 Model validation</i>	71
<b>3.8 References</b>	73
<b>CHAPTER 4 – EXPERIMENTAL WORK</b>	76
<b>4.1 Outline of Test Programme</b>	76
<b>4.2 Design of Test Specimens</b>	78
<i>4.2.1 Materials properties</i>	78

4.2.2 Specimen manufacturer	80
4.2.3 Corrosion conditioning	83
4.2.4 Crack measurement	87
4.2.5 Bond test loading procedure	88
4.2.6 Corrosion rate measurement	89
4.3 References	90
<b>CHAPTER 5 – PRESENTATION AND DISCUSSION OF EXPERIMENTAL RESULTS</b>	91
5.1 Introduction	91
5.2 Presentation of Experimental Results	91
5.2.1 Measurement of surface crack width	91
5.2.2 Bar section loss and corrosion penetration	92
5.2.3 Bond test results	93
5.2.4 Failure mode of bond test	94
5.2.5 Analysis of experimental results	95
5.3 Interpretation and Discussion of Experimental Results	100
5.3.1 Effects of impressed current on corrosion process	100
5.3.2 Corrosion of main reinforcement	104
5.3.3 Corrosion-induced cracking	105
5.3.3.1 Crack pattern and location	105
5.3.3.2 Surface crack width	107
5.3.3.2.1 Selection of crack width parameter	107
5.3.3.2.2 Influence of casting position on crack width	110
5.3.3.2.3 Effects of corrosion measurement on crack width	111
5.3.3.2.4 Influence of impressed current	112
5.3.4 Bond strength results	114
5.3.4.1 Control uncorroded specimens	114
5.3.4.2 Corroded specimens	118
5.3.4.2.1 Bond failure mode	119
5.3.4.2.2 Bond strength	120
5.3.4.2.3 Effects of width of corrosion-induced crack on bond strength	122
5.3.4.2.4 Bond strength for different corrosion levels	123
5.3.4.2.5 Bond-slip behaviour	124
5.3.5 Influence of corrosion parameters on residual bond strength	130
5.4 Summary of Experimental Results	136

<b>5.5 References</b>	137
<b>CHAPTER 6 – CONCLUSIONS AND RECOMMENDATIONS</b>	139
<b>6.1 Conclusions</b>	139
<b>6.2 Recommendations for Future Research</b>	140



## LIST OF TABLES

Table 2.1: Review of impressed current value	15
Table 2.2: Summary of bond test results as derived from fib Bulletin 10 [2.15]	27
Table 2.3: Amount of corrosion to initiate crack of concrete cover [2.15]	28
Table 2.4: Influence of several parameters on the initiation and propagation of crack width [2.37]	29
Table 3.1 Value of $\alpha$ for different corrosion products	40
Table 3.2: Base value of fracture energy $G_{f0}$ (N/mm)	49
Table 3.3: Input data for interface properties	51
Table 3.4: Material properties	67
Table 4.1: First batch concrete strength at 28 days	78
Table 4.2: Second batch concrete strength at 28 days	79
Table 4.3: First batch concrete splitting tensile test	80
Table 4.4: Second batch concrete splitting tensile test	80
Table 4.5: First batch control specimen details	82
Table 4.6: Second batch control specimen details	82
Table 4.7: Details of specimens with “fast” corrosion for the first batch	84
Table 4.8: Details of specimens with “fast” corrosion for the second batch	84
Table 4.9: Details of specimens with “slow” corrosion for the first batch	85
Table 4.10: Details of specimens with “slow” corrosion for the second batch	85
Table 5.1: Bond strength of control specimens - first batch	96
Table 5.2: Bond strength of control specimens - second batch	97
Table 5.3: First batch corroded specimens	98
Table 5.4: Second batch corroded specimens	99
Table 5.5: Average impressed current for different casting batches and bar diameters	100
Table 5.6: Theoretical and actual mass loss for specimens with corroded stirrups	106
Table 5.7: Comparison between single crack and adjacent surface cracks	108
Table 5.8: Summary of the measured and predicted bond strength ratio	118
Table 5.9: First batch to second batch bond strength ratio	122
Table 5.10: $f_{b,r}$ value for corroded specimens with zero surface crack	134

## LIST OF FIGURES

Figure 2.1: The corrosion reaction on steel	6
Figure 2.2: Schematic representation of how the radial components of the bond forces are balanced against tensile stress rings in the concrete in an anchorage zone [2.16]	8
Figure 2.3: Schematic of the RILEM concentric pullout test	10
Figure 2.4: Direct tension pull-out bond test	11
Figure 2.5: Beam end type specimen	12
Figure 2.6: National Bureau of Standard bond test beam [2.20]	12
Figure 2.7: University of Texas beam [2.20]	12
Figure 2.8: Cantilever bond specimen	13
Figure 2.9: Radius loss of reinforcing bar	17
Figure 2.10: Effects of reinforcement corrosion on residual structural capacity [2.35]	20
Figure 2.11: Bond strength versus corrosion	22
Figure 2.12: Bond strength versus corrosion penetration based on Equations 2.8 ( $\rho > 0.25$ ) and 2.9 ( $\rho < 0.25$ )	25
Figure 3.1: Crack at two different stages of cracking [3.11]	41
Figure 3.2: Idealized stress-strain diagram for cover concrete in uniaxial tension	45
Figure 3.3: Idealization of specimen	47
Figure 3.4: Nonlinear behaviour of concrete in compression	48
Figure 3.5: Location of interface elements	50
Figure 3.6: Delamination interface properties	51
Figure 3.7: Tensile stress versus displacement (crack width)	52
Figure 3.8: Mesh element for concrete and steel reinforcement	54
Figure 3.9: 2D Interface elements	54
Figure 3.10: Specimen model to study of mesh density	55
Figure 3.11: Effects of different mesh elements on displacement	56
Figure 3.12: Crack width for different interface divisions	56
Figure 3.13: Increment-iterative method	57
Figure 3.14: Radius expansion versus load factor	59
Figure 3.15: Crack location for 10 mm diameter main reinforcing bar	60
Figure 3.16: Crack location for 16 mm diameter main reinforcing bar	61

Figure 3.17: Crack width propagation for different $c/\phi_b$ ratios for 16 mm and 10 mm bar diameter (model 1)	63
Figure 3.18: The influence of porous zone on crack propagation (model 2)	64
Figure 3.19: Variation of surface crack widths for different $c/\phi_b$ ratios with 0.1 mm and 0.2 mm radius expansion	65
Figure 3.20: Model specimen	67
Figure 3.21: Crack pattern for different concrete cover thicknesses	69
Figure 3.22: Crack pattern for combined corner-centre bar location	70
Figure 3.23: Cabrera's [3.29] specimen with multiple reinforcements	71
Figure 3.24: Crack pattern for different bar diameters	72
Figure 4.1: Detailing of specimens	77
Figure 4.2: 30 Beam end type specimens ready for concreting	79
Figure 4.3: Location of 80 mm and 15 mm plastic sleeve	81
Figure 4.4: Anode arrangement for corrosion conditioning	86
Figure 4.5: Crack configuration [4.6]	88
Figure 4.6: Bond test setup	89
Figure 5.1: Surface crack measurement	92
Figure 5.2: Bond slip diagram for the top cast and the bottom cast specimen	93
Figure 5.3: Splitting failure for corner bar location (specimen 10/2.5/BC/2)	94
Figure 5.4: Splitting failure for centre bar location (specimen 16/1.6/TCe/2)	95
Figure 5.5: Actual versus theoretical mass loss for first casting batch	101
Figure 5.6: Actual versus theoretical mass loss for second casting batch	102
Figure 5.7: Average theoretical and actual mass loss for different bar diameters, locations and impressed currents	103
Figure 5.8: Average corrosion for the first batch	104
Figure 5.9: Average corrosion for the second batch	105
Figure 5.10: Longitudinal surface crack on centre bar location	106
Figure 5.11: Longitudinal surface crack on corner bar location	107
Figure 5.12: Comparison of $w_{cr,max}$ and $w_{cr,tot}$ with the crack width in single crack specimens	109
Figure 5.13: Surface crack width for different batches	111
Figure 5.14: Mean crack width for two different corrosion measurements	112
Figure 5.15: Crack width for different bar locations	113
Figure 5.16: Influence of concrete cover on control bond strength	114
Figure 5.17: Clear concrete cover for different bar locations	115

Figure 5.18: Bond strength from different cover-to-diameter ratios	118
Figure 5.19: Splitting failure on centre bar location	119
Figure 5.20: Splitting failure on corner bar location	120
Figure 5.21: Corroded bond strength	121
Figure 5.22: Influence of corrosion crack width on bond strength	123
Figure 5.23: Corroded bond strength versus corrosion penetrations	124
Figure 5.24: Corroded bond strength versus section loses	124
Figure 5.25: Bond stress-slip diagram for 16 mm diameter control specimens	126
Figure 5.26: Bond stress-slip diagram for 10 mm diameter control specimens	127
Figure 5.27: Bond stress-slip diagram for 16 mm diameter corroded specimens	128
Figure 5.28: Bond stress-slip diagram for 10 mm diameter corroded specimens	129
Figure 5.29: Relative bond slip versus corrosion penetrations	130
Figure 5.30: Average $f_{b,r}$ value	131
Figure 5.31: Average $f_{b,r}$ value for $c/\phi_b$ of 1.6 and 2.5	132
Figure 5.32: Average $f_{b,r}$ value for various $c/\phi_b$ ratios	133
Figure 5.33: Average crack width versus average $f_{b,r}$ value for $c/\phi_b$ of 1.6 and 2.5	135
Figure 5.34: Average crack width versus average $f_{b,r}$ value for various $c/\phi_b$ ratios	135
Figure 5.35: $f_{b,r}$ versus crack width for the bottom and the top cast bar	136

## NOTATION

$A_s$	Sound steel cross section
$A_{st}$	Area of stirrup
$\beta$	The resultant force angle
$C_R$	Percent of weight loss of steel bar
$c$	Concrete cover thickness
$c_{so}$	Effective cover
$d$	Cylinder diameter
$E_c$	Modulus of elasticity
$F$	Faraday's constant
$F_{splitting}$	Splitting resistance
$F_{stirrup}$	Stirrup resistance
$f_b$	Bond strength
$f_{bres}$	Residual bond strength for assessment
$f_{bu}$	Design bond strength
$f_{cm}$	Actual compressive strength of concrete at age 28 days
$f_{ctm}$	Mean axial tensile strength
$f_{ct,sp}$	Mean splitting tensile strength
$f_s$	Steel stress
$f_{sp}$	Splitting strength
$f_t$	Tensile strength of concrete
$f_{t,max}$	Maximum tensile strength
$d_c$	Cylinder diameter
$d_{max}$	Maximum aggregates size
$G_0$	Initial weight of steel bar before corrosion
$G$	Final weight of steel bar after removal of corrosion products
$G_f$	Fracture energy of concrete
$G_{FO}$	Base value of fracture energy
$g_0$	Weight per unit length of steel bar
$h$	Fracture zone width
$I$	Current
$i_{corr}$	Impressed current density
$L$	Bonded length
$l_c$	Corroded length

$l$	Length of cylinder
$l_s$	Effective development length
$M$	Atomic weight of metal
$m$	Reference mass per unit length
$N$	Number of stirrup within development length
$n$	No of bar being develop
$P$	Maximum load
$p_{corr}$	Corrosion penetration
$Q_{corr}$	Amount of corrosion reinforcement
$r$	Radius of steel bar
$r_i$	Initial bar radius
$r_t$	Bar radius (mm) at time $t$
${}^tT$	Current temperature
$T_{ref}$	Reference temperature
$t$	Time
$\nu$	Poisson ratio
$W_0$	Weight of reinforcement prior to corrosion
$W_1$	Weight of reinforcement after corroded and it was cleaned in acid solution
$W_{n0}$	Weight of non-corroded reinforcement before it was cleaned in acid solution
$W_{n1}$	Weight of the same non-corroded reinforcement after it was cleaned in acid solution
$w_{cr}$	Crack width
$w_{cr,max}$	Maximum crack width
$w_{cr,tot}$	Total crack width
$x$	Attack penetration
$z$	Ionic charge
$\Delta A_s$	Steel cross section loss
$\Delta M$	Mass of steel consumed per unit length
$\Delta r$	Thermal expansion of bar radius
$\Delta t$	Elapsed time in second
$T$	Current temperature
$\Delta T$	Temperature rise
$T_{ref}$	Reference temperature

$\Delta V_{rust}$	Volume of generated rust
$\varepsilon_t$	Thermal strain
$\Phi_b$	Bar diameter
$\Delta\Phi_b$	Reduction of bar diameter
$\alpha_T$	Coefficient of thermal expansion
$\alpha$	Volumetric expansion ratio of corrosion products
$\delta$	Free increase in bar radius

# CHAPTER 1 – INTRODUCTION

Over the years, reinforced concrete has been promoted as a long-lasting material that requires little maintenance. However, a worldwide problem has now emerged because of the deterioration of concrete. Defects and deterioration not only appear in old concrete structures but are also observed in newly constructed structures. The mechanism and rate of deterioration are controlled by the environment, the paste microstructure, and the fracture strength of the concrete [1.1]. The corrosion of the embedded reinforcement is a major contributor to the deterioration of structural concrete. The direct effects of reinforced corrosion include loss of bar section, increase in bar diameter resulting from the volumetric expansion of the corrosion products, change in the characteristics of the bar or concrete interface upon formation of the corrosion product, and reduction of the concrete section [1.2]. The loss of bar section may reduce the ductility of the steel reinforcing bar. A structure with insignificant ductility may fail and collapse in a brittle manner without warning.

Rust generated from the corrosion process causes volumetric expansion, which induces radial pressure on the surrounding concrete and leads to longitudinal cover cracking. The presence of cracks reduces the confinement action on which bond resistance depends. Rust also accumulates between the concrete and the reinforcing bars and influences the friction between the reinforcement bars and the concrete, an outcome that may reduce bond strength. Spalling of the concrete cover, as a result of excessive cracking, exposes the main reinforcement and leaves it unprotected against further damage. Corrosion may also contribute to a loss of composite interaction between the concrete and the reinforcing bars. All four issues reduce the residual capacity of the reinforced concrete structure.

## 1.1 Background of the Problem

The most appropriate measure of deterioration to use when assessing the residual capacity of corrosion-damaged concrete structures remains uncertain. For example, is it the percentage loss of bar section, the average thickness lost to corrosion, or the surface crack width that correlates best with the effects of corrosion on the residual strength of a structural member? The various strength loss mechanisms obtained through a literature



review suggest that each mechanism may correlate with a different measure of degradation. Therefore, an in-depth study must be performed to justify the best parameter(s) to use in assessing the residual capacity of reinforced concrete structures. This investigation focuses primarily on identifying the measure of greatest significance for the bond between corroding reinforcement and concrete.

## **1.2 Aim and Objectives of the Research**

This research aims to integrate correlations between corrosion-induced deterioration and strength degradation into a systematic methodology for estimating the residual strength of reinforced concrete structures with a particular emphasis on the bond between reinforcing steel and concrete.

The research objectives are as follows:

- 1) to relate bond strength loss as a result of corrosion to the following measures of corrosion damage: section loss (expressed as a percentage of the original cross-section), corrosion penetration (expressed as a loss of bar radius), and surface crack width;
- 2) to determine the sensitivity of the relationship between bond strength loss and corrosion damage to the corrosion rate and to various geometric parameters, including cover, bar diameter, and casting position;
- 3) to identify the most appropriate measure of corrosion damage for each aspect of anchorage bond strength loss while considering statistical reliability and sensitivity; and
- 4) to validate proposals against available test data, including those that are self-generated and reported by others.

### 1.3 References

- [1.1] P.A.M. Basheer, S.E. Chidiact and A.E. Long, *Predictive model for deterioration of concrete structures*, Construction and Building Materials, **10**, 1, 27-37 (1995)
- [1.2] J. Cairns, Y. Du and D. Law, *Residual bond strength of corroded plain round bars*, Magazine of Concrete Research, **58**, 4, 221-231 (2006)

## CHAPTER 2 – LITERATURE REVIEW

### 2.1 Basic Mechanism of Corrosion of Reinforcement

Research on the corrosion of steel reinforcement in reinforced concrete started over 200 years ago when damage was observed after a concrete structure was exposed to seawater. According to Biczok [2.1], the problems of reinforcement corrosion caused by seawater action was addressed as early as 1840 by J. Smeaton and L. J. Vicat, while a report on concrete damage caused by chemical attack and observed on a harbor structure in Algiers was published by L. J. Vicat in 1841. In the last decade, concern has grown about the problem of corrosion damage in reinforced concrete structures. Owing to the importance of understanding the process and influence of various parameters on corrosion damage, an evaluation of the corrosion of reinforcing steel on concrete structures is necessary.

The mechanism of metal corrosion depends on the involvement of water in the process. The corrosion of steel bars in reinforced concrete is classified as an electrochemical process. Corrosion in the normal sense involves the loss of electrons from the metal to the environment (usually water and oxygen) and the formation of corrosion products such as oxides [2.2] [2.3]. When steel is exposed to normal climatic conditions, it corrodes even when it is not connected electrically to another metal. This process confirms the basic theory that steel is not homogeneous but contains areas of slightly differing composition.

The corrosion of steel in concrete can be modeled as a three-stage process [2.4]. The first stage, usually called the initiation stage, is the diffusion of carbon dioxide ( $\text{CO}_2$ ) or chloride ions through the concrete cover to the steel reinforcement to cause its depassivation. The second stage is the activation stage, when more reinforcing bars start to corrode and rust products are formed. The third stage is deterioration, when cracking and spalling of the concrete cover occur. Eventually, the deterioration reaches a level defined as the end of the functional life of the structure; rehabilitation must take place at this point.

### ***2.1.1 Initiation stage***

Generally, concrete provides an alkaline environment for the reinforcing steel where the pH level is between 12.5 and 13.5, resulting in the passive state of steel. The dense and relatively impermeable structure of concrete provides physical protection, whereas the high alkalinity of the concrete pore solution provides chemical protection [2.5]. In practice, depassivation of the film may occur under two specific sets of conditions: (i) reduction of the pH value because of a reaction with atmospheric CO<sub>2</sub> (carbonation) and (ii) penetration of chloride ions into the concrete pore solution around the steel [2.6]. Less commonly, stray electrical currents may also lead to reinforcement corrosion.

CO<sub>2</sub> from the external environment penetrates concrete through diffusion. In the presence of water, this gas dissolves and reacts with cement to form carbonates. This reaction decreases the pH value to 9.5, resulting in the destruction of the passivating layer on the steel surface. Corrosion begins only if the reinforcing steel has a significant potential difference along with the presence of sufficient moisture and oxygen [2.7].

Chlorides penetrate the cover of a reinforced concrete member through a combination of diffusion and capillary action, and they gradually permeate until they reach the steel surface. Steel reinforcement becomes depassivated after a threshold chloride concentration is reached, which depends principally on the cement composition, the concrete quality, and the conditions of environmental exposure [2.8].

### ***2.1.2 Activation stage***

Areas of rust start appearing on the steel surface once the passive layer breaks down [2.4]. The rate of corrosion may vary from one point to another because of variations in alkalinity (pH) and the concentration of salt and oxygen in the solution in the concrete close to the bar surface [2.9].

Iron dissolves away from the anodic region, while the electrons passing through the cathodic regions combine with water and oxygen to form hydroxyl ions [OH]<sup>-</sup>. The hydroxyl ions combine with the ferrous ions (Fe<sup>++</sup>), and are released into the electrolyte at the anode to form ferrous hydroxide [Fe (OH)<sub>2</sub>], which is a slightly soluble jellylike

substance promptly converted into some other forms of iron oxide in the presence of oxygen, such as insoluble or ferric oxide ( $\text{Fe}_2\text{O}_3 \cdot \text{H}_2\text{O}$ ). The result is rust (Figure 2.1). This form of attack may be relatively localized and lead to the formation of corrosion pits.

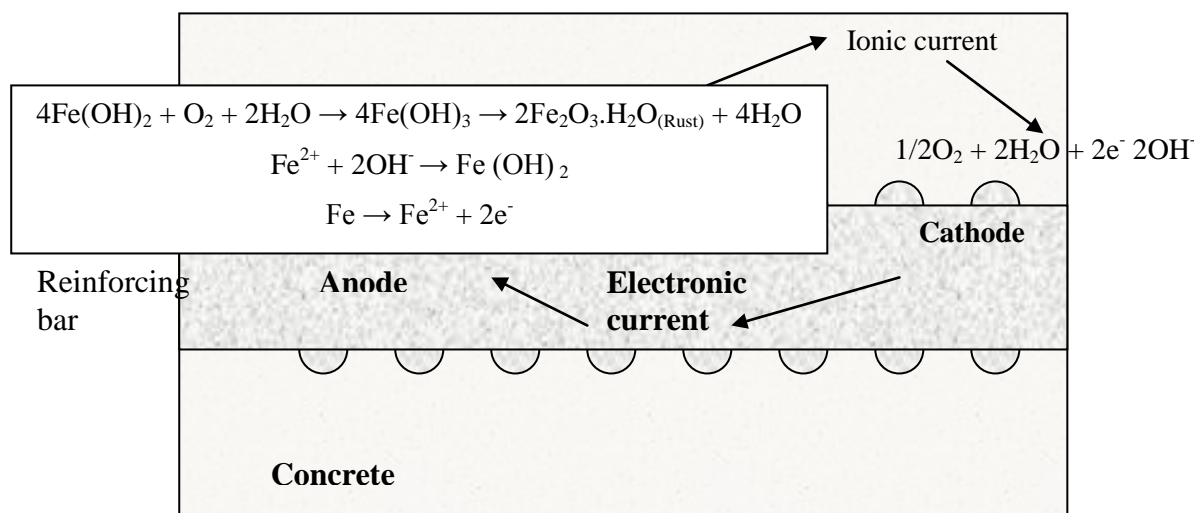
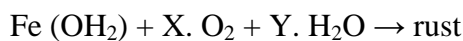
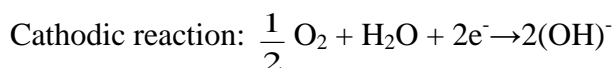


Figure 2.1: The corrosion reaction on steel

The two types of electrochemical corrosion are microcell and macrocell corrosion. Microcell corrosion consists of pairs of immediately adjacent anodic and cathodic areas, which often leads to uniform ion removal [2.10]. This type of corrosion is generally caused by the carbonation of concrete over a wide area in the vicinity of the steel.

Macrocell corrosion leads to localized attack that can penetrate a small area of a bar through a relatively rapid attack. This type normally occurs in the case of chloride-induced corrosion, which consists of anodically acting areas where the critical chloride content has been reached and where large cathodes are next to the anode or sometimes also quite far away, up to a few meters from it [2.11].

When reinforcement rusts, the corrosion products generally occupy a considerably larger volume than the steel destroyed [2.9]. The magnitude of this increase in volume typically varies in the region of two to three times the volume of the metal. This increase leads to the observed cracking and spalling of the concrete cover as a consequence of the corrosion of steel in concrete. It also leads to the formation of red or brown brittle, flaky

rust on the bar surface and the rust stains seen on cracks in the concrete. Some of these corrosion products disperse into the concrete pores surrounding the bar, and the extent to which they disperse influences the build-up of pressure on the concrete around the bar.

### ***2.1.3 Deterioration stage***

Corrosion reduces the cross-section of the steel reinforcement, and possibly of the concrete, because of cover spalling, which in turn decreases the load-carrying capacity of the structure. Pitting corrosion is more dangerous than uniform corrosion. Without necessarily being evident on the surface of the member, this corrosion may progressively reduce the cross-sectional area of the rebar to a point where the rebar can no longer withstand the applied load, leading to the catastrophic failure of the structure [2.12]. The basic problem associated with the deterioration of reinforced concrete as a result of corrosion is not only that the reinforcement loses its mechanical strength, but also that the products of corrosion exert stress within the concrete that cannot be resisted by the limited plastic deformation capacity of the latter, which results in the concrete cracking along the length of the bar. This outcome weakens the bond and anchorage between concrete and reinforcement, which directly affects the serviceability performance and ultimate strength of concrete elements within structures [2.13]. In addition, spalling of the concrete cover reduces the cross-sectional area of concrete in the member, which may also reduce its axial, bending, and shear capacities.

## **2.2 Bond Behaviour of Ribbed Bar – General Description**

To avoid the loss of composite action and anchorage failure, a bond between reinforcing bars and concrete is needed for the satisfactory performance of a reinforced concrete structure. The bond is the interaction between the reinforcement and the surrounding concrete made through the transfer of stresses that combine the compressive strength of the concrete and the tensile strength of the reinforcement in reinforced concrete structures [2.14]. Thus, the bond mechanism has a strong influence on the fundamental behavior of a structure, such as crack development and spacing, crack width, ductility, and strength. The bond action generates inclined forces that radiate outward in the concrete. The inclined force is often divided into a longitudinal component, denoting bond stress, and

the radial component, denoting normal stress or splitting stress. The inclined forces are balanced by tensile ring stresses in the surrounding concrete (Figure 2.2), as explained in [2.15], and by confining reinforcement if present. The rings are thinnest in the concrete cover protecting the reinforcement. If the tensile stress exceeds the tensile strength of the concrete, then longitudinal splitting cracks form in the concrete.

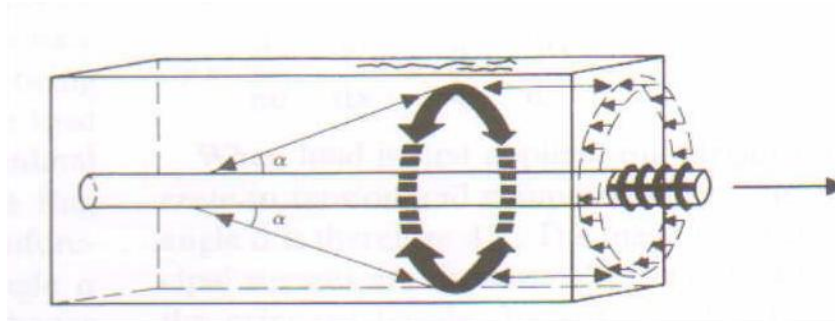


Figure 2.2: Schematic representation of how the radial components of the bond forces are balanced against tensile stress rings in the concrete in an anchorage zone [2.15]

In the case of ribbed bars, the bond strength is developed mainly by mechanical interlocking [2.16]. Failure is generally reached by concrete splitting when internal stresses are induced in the concrete cover by the bond action of the rebar, which causes cracking. Anchorage is the embedment of a bar in concrete so it can carry a load through the bond between the steel and concrete [2.17]. If anchorage length is insufficient, then the full strength of the bar cannot be achieved.

For plain bars, the presence of the normal stresses is a condition for transferring bond stresses after chemical adhesion is lost. When resistance to the normal stresses is lost for some reason, bond stresses cannot be transferred. This situation occurs if the concrete around the reinforcement bar is penetrated by longitudinal splitting cracks and if no transverse reinforcement or transverse pressure exists to continue to resist the radial force. A similar effect occurs if a reinforcing bar starts yielding. With the Poisson effect, the rate of contraction of the steel bar increases at yielding. Thus, the normal stress between the concrete and the steel is reduced so that only low bond stress can be transferred. When the concrete surrounding a ribbed reinforcing bar is well confined, which means it can withstand the ring splitting stresses, and if the bar does not start yielding, then a pullout failure occurs. Under these conditions, failure is characterized by shear cracking between the adjacent ribs of the bar. This failure is the upper limit of the bond strength.

Bond behavior depends on a variety of factors and parameters, including the reinforcing unit (bar, multi-wire strand, and tendon), concrete, and stress state in the reinforcing unit and the surrounding concrete [2.18]. Nevertheless, many technological aspects, such as the concrete cover, the clear space between the bars, the number of bar layers and bundle bars, the casting direction with respect to bar orientation, and the bar position with respect to the free surface of the fluid concrete, also contribute directly to bond behaviour.

### ***2.2.1 Bond test methods***

The selection of a proper type of specimen for bond strength evaluation is of importance because it significantly influences the measured value of bond strength [2.19]. Some of the tests widely used by researchers include the RILEM pullout test, axial tension pullout test, bond beam test, National Bureau of Standards beam test, cantilever bond test, and the University of Texas (UoT) beam test [2.20].

In the RILEM concentric type pullout bond test, a bar is embedded in a cylinder or rectangular block of concrete, and the force required to pull it out or make it slip excessively is measured (Figure 2.3). This test is used to compare the bond strengths of different bars. In a reinforced concrete beam or slab, the concrete surrounding the tensile reinforcement is in tension, whereas the concrete in this pullout test is in compression, which not only eliminates transverse tension cracks in the specimen but also increases bond strength. Failure usually occurs through (1) the longitudinal splitting of the concrete in the case of deformed bars, (2) the pulling of the bar through the concrete in the case of a plain or very small bar or very lightweight aggregate, and (3) the yielding of the bar if the embedment is more than five times the bar diameter. Clearly, this test does not measure a quantity that can be directly related to practice, and it is only used to classify bars, not to give design values for bond strength [2.21].



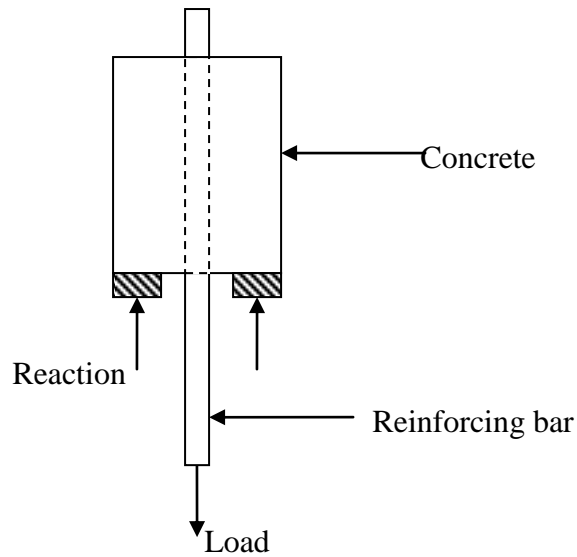


Figure 2.3: Schematic of the RILEM concentric pullout test

A modification of the pullout test is the tension pullout diagram (Figure 2.4), which eliminates the compression on the concrete. However, this test introduces the special problem of spaced splice, and any crack pattern is influenced by this interaction. This test appears to be useful in comparing the slip resistance of various rib sizes and patterns [2.20].

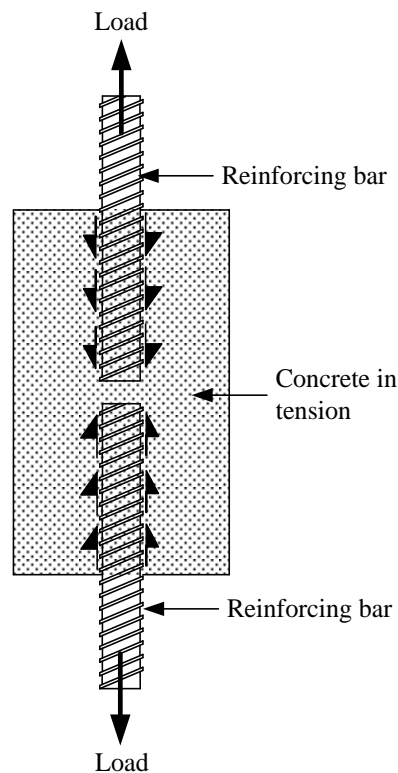


Figure 2.4: Direct tension pullout bond test

Chana et al. [2.21] used another method to determine the bond strength of reinforced concrete. Beam end-type specimens give a more realistic test that simulates support conditions in practice and allows a direct comparison of bond strength for a top cast and a bottom cast condition. This type of specimen is appropriate for considering splitting failure, where the bond strength of the bar can be compared for design purposes. A plastic sleeve covering the bar end underneath the transverse restraint prevents the possible enhancement of the bond strength as a result of an external restraining force (Figure 2.5).

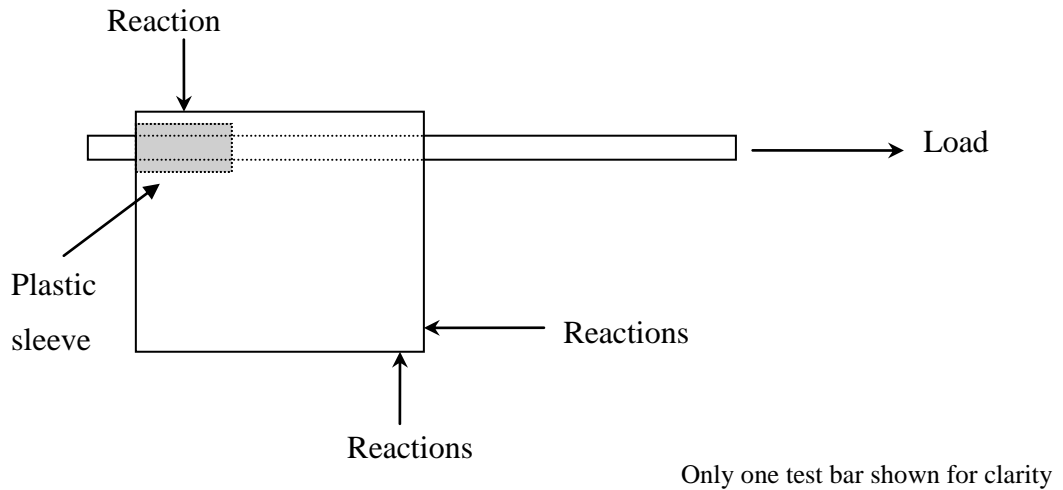


Figure 2.5: Beam end type specimen

For the beam specimen, bond strength can be evaluated through two types of beams: the National Bureau of Standards (NBS) bond test (Figure 2.6) and the UoT beam test (Figure 2.7) [2.20]. A major consideration in each beam is the removal of reaction restraints that may confine the concrete over the bar and thereby increase the splitting resistance. The beam test truly represents the bond stress conditions encountered in the actual flexural member. However, in the NBS specimen, the quantity of stirrups provided tends to be significantly higher than that in practice, while the UoT test leads to difficulties in interpretation because of the absence of a constant moment zone and shear cracking. Furthermore, both specimens are expensive to make and heavy to handle because they use full-size members with the large sizes of bars that create the most serious problems.

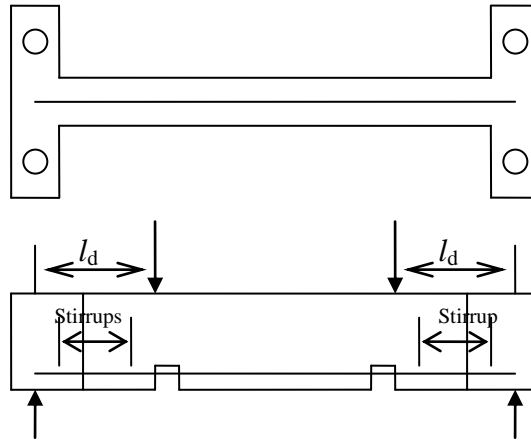


Figure 2.6: National Bureau of Standards bond test beam [2.20]

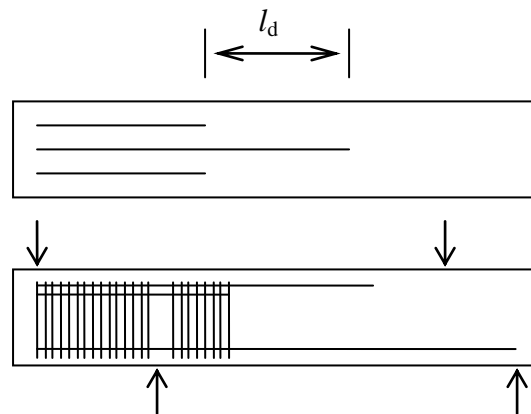


Figure 2.7: University of Texas beam [2.20]

Kemp et al. [2.22] developed the cantilever bond specimen (Figure 2.8), similar in principle to and different only in detail from Chana's beam end specimen, which is based on the ultimate strength criteria for shear and flexure. Some advantages of this type of bond test are listed as follows:

- i) This test produces a bond stress situation similar to that in an actual flexural member.
- ii) Concrete and steel experience similar tensile strains, and strain gradients produced in this specimen are similar to those occurring in actual structures.
- iii) This test specimen is smaller and cheaper than the beam test specimens mentioned previously.
- iv) The bar may be prevented from any confining action with the support of a shield or soft covering.

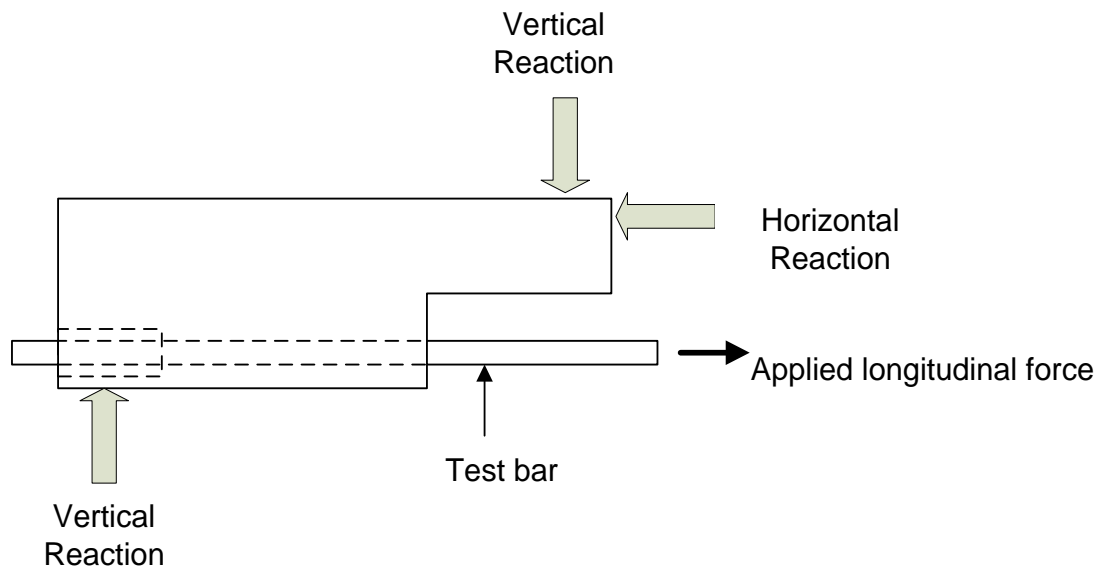


Figure 2.8: Cantilever bond specimen

## 2.3 Accelerated corrosion

### 2.3.1 Technique

Accelerating degradation and controlling the rate of corrosion during the propagation period are sometimes necessary [2.23] to study the effects of corrosion within a realistic time scale. The methods vary depending on the nature of the corrosion under investigation. For chloride-induced corrosion, accelerated corrosion techniques are widely used to a) reduce the time for corrosion to initiate compared with the diffusion process and b) accelerate the rate of active corrosion. Three methods are commonly used: admixed chloride (typically 3% by weight of cement) in the concrete mix, impressed voltage or current to the specimen, and wet and dry techniques, which usually require several months because they depend on the duration of the wetting and drying periods.

When an impressed current is used to drive corrosion, the amount of mass loss is related to the electrical charge consumed when passivity has been compromised and can be modeled with Faraday's law:

$$Mass\ loss = \frac{MI_{corr}t}{zF} \quad (2.1)$$

where

$M$	-	Atomic weight of metal (56 for Fe)
$I_{corr}$	-	Current (amperes)
$t$	-	Time (seconds)
$z$	-	Ionic charge (2 for Fe)
$F$	-	Faraday's constant (96,500 coulombs)

The mass of iron  $M$  consumed over time is related to the amount of current  $I_{corr}$ . Faraday's law is the basis for all published models that assume a constant rate of steel mass consumption and rust production. In other words, for constant current, Faraday's law implies a linear increase of the loss of steel with time and a linear increase in mass loss. The value of  $z$  (valency of the reaction) is equal to 2 [2.3].

Some researchers have used the corrosion rate value observed on site as a reference current value for corrosion conditioning [2.23] [2.24] [2.25]. The maximum corrosion rate measured in laboratory conditions without the application of an impressed current is around  $100 \mu\text{A}/\text{cm}^2$  (in cracked concrete submerged in seawater) based on the experimental work by Andrade and Alonso [2.26]. Meanwhile, for on-site conditions, the maximum recorded  $i_{corr}$  value is around  $1\text{--}10 \mu\text{A}/\text{cm}^2$ . Other researchers have used a different current density to accelerate the corrosion. Table 2.1 shows a comparison of the impressed current density values used previously by researchers to accelerate the corrosion on reinforced concrete. These values range from  $3 \mu\text{A}/\text{cm}^2$  [2.27] to  $5 \times 10^9 \mu\text{A}/\text{cm}^2$  [2.28].

Researcher	Impressed current ( $\mu\text{A}/\text{cm}^2$ )	Counter electrode
Al- Sulaimani [2.29]	2000	Stainless steel plate
Rasheeduzzafar et al. [2.30]	3000	Aluminium plate Galvanised steel
Andrade et al. [2.24]	10 and 100	-
Saifullah and Clark [2.31]	40, 90, 150, 250, 500, 1000,2000, 4000	Stainless steel
Almusallam et al. [2.19]	0.4 A	Stainless steel plate
Andrade et al. [2.27]	3, 10, 100	-
Rodriguez et al. [2.25]	100	Stainless steel
Huang and Yang [2.28]	$5 \times 10^9$	-
Liu and Weyers [2.32]	3.75, 2.41 and 1.79	-
El Maaddawy and Soudki [2.33]	100, 200, 350, 500	Stainless steel
Fang et al. [2.34]	0 – 2 Ampere	Stainless steel plate
Badawi and Soudki [2.35]	150	Stainless steel
Cairns et al. [2.36]	10 and 50	Stainless steel angle

Table 2.1: Review of impressed current value

However, the density of impressed current has significant effects on the level of deterioration in concrete. Andrade et al. [2.22] showed that, for the same crack width, high corrosion rates require higher attack penetration than low corrosion rates ( $< 5 \mu\text{A}/\text{cm}^2$ ). Therefore, for the same attack penetration, a low current produces a greater crack width than a high current. At the same time, in El Maaddawy and Soudki [2.33], the crack width increased with an increasing level of impressed current density with a higher impressed current. The researchers also noted that inducing corrosion through a low current density gives corrosion products the opportunity to diffuse through the concrete pores, thus decreasing crack width. Furthermore, with a high current density, corrosion products concentrate around the steel reinforcing bars, inducing higher deformation. However, for the same attack penetration, a greater crack width was observed for a higher impressed current. These inconsistent results came from different values of impressed current used, as discussed in Saifullah and Clark [2.31] regarding the influence of different current densities on crack initiation. They mentioned that with an impressed current of up to  $0.15 \text{ mA}/\text{cm}^2$ , which was used by Andrade ( $0.01\text{--}0.1 \text{ mA}/\text{cm}^2$ ), a higher percentage of mass loss is required to induce a surface crack than a low corrosion rate.

However, for an impressed current of greater than 0.15 mA/cm<sup>2</sup>, which was used by El Maaddawy (0.1, 0.2, 0.35, and 0.5 mA/cm<sup>2</sup>), the opposite trend was observed, where only a small penetration is required by a high current to induce the same crack as a low current. As these results covered crack initiation only, on the basis of the linear relationship between crack width and attack penetration or the percentage of section loss, the same trend may happen for crack propagation.

Regarding bond strength, the results of Saifullah and Clark [2.31] show that the specimens that corroded at faster rates have considerable decreases in bond strength at the cracking stage with about a 18% and 40% reduction in bond strength at current densities of 2.0 and 4.0 mA/cm<sup>2</sup> respectively. At a low current density (slow rate of corrosion, less than 0.25 mA/cm<sup>2</sup>), the amount of corrosion that caused cracking, concrete bond strength, and stiffness as proportions of their non-corroded values increased with the increase in current density. However, when the current density exceeded 0.15–0.25 mA/cm<sup>2</sup>, the value of these parameters decreased with a further increase in current density.

### **2.3.2 Corrosion quantification**

Numerous researchers have successfully calculated the theoretical steel reinforcement mass loss under impressed current by using Faraday's law in their test work [2.23] [2.24] [2.33]. The results were compared with the actual mass loss from the gravimetric weight loss.

The corrosion intensity of applied current ( $i_{corr}$ ) is converted to the diameter decrease through the following formula [2.24]:

$$\phi_{b(t)} = \phi_b - 0.023 i_{corr} t \quad (2.2)$$

Rodriguez et al. [2.37] substituted the diameter decrease in Equation 2.2 by the radius loss or corrosion penetration (Figure 2.12):

$$\begin{aligned} r_i - r_t &= x, \text{ thus} \\ x &= 0.0115 i_{corr} t \end{aligned} \quad (2.3)$$

where

- $x$  - Attack penetration in mm
- $t$  - Time in years since the chloride reached the reinforcement
- $i_{corr}$  - Average value of corrosion intensity in  $\mu\text{A}/\text{cm}^2$  during time  $t$  (year)

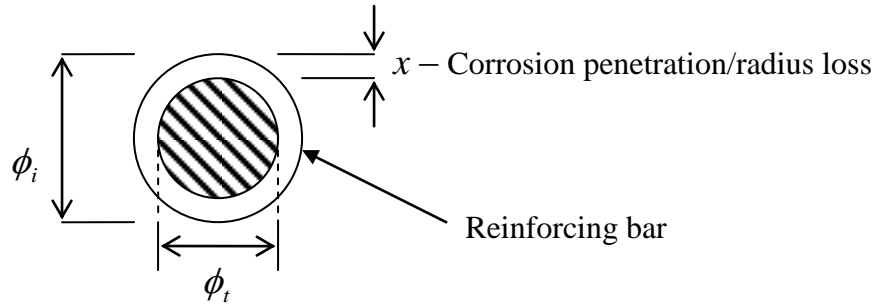


Figure 2.9: Radius loss of reinforcing bar

Pantazopoulou and Papoulis [2.3] suggested a formula based on Equation 2.2 to calculate the mass of steel consumed by corrosion:

$$\Delta M_s = 2.862 \times 10^{-7} \pi \phi_b i_{corr} \Delta t \text{ (kg/m)} \quad (2.4)$$

where:

- $\Delta M_s$  - Mass of steel consumed per unit length
- $\phi_b$  - Initial diameter of the bar in meters
- $\Delta t$  - Elapsed time in seconds
- $i_{corr}$  - Mean annual corrosion current per unit anodic surface area of steel (amperes per meter squares)

Equations 2.2 to 2.4 were used to determine the corrosion penetration and mass loss based on the total amount of electric current impressed through the steel bar during the corrosion process. The predicted value was considered to be true if the current impressed was 100% effective in producing corrosion, which sometimes did not happen, as discussed by Alonso et al. [2.38]. Therefore, the gravimetric method was used as an alternative approach to measure the actual degree of corrosion or corrosion level after the corrosion conditioning. This method is based on measuring the weight loss of the steel bar after the corrosion process relative to its corresponding weight before the corrosion process. For a specific length of the corroded area, Fang et al. [2.39] used the following equation to determine the percentage of weight loss of the steel bar:



$$C_R = \frac{G_o - G}{g_o l} \times 100\% \quad (2.5)$$

where:

- $G_o$  - Initial weight of the steel bar before corrosion (*kg*)
- $G$  - Final weight of the steel bar after removal of the corrosion products (*kg*)
- $g_o$  - Weight per unit length of steel bar (*kg/mm*)
- $l$  - Corroded length (*mm*)

Du et al. [2.40] used another equation to determine the percentage of weight loss for the whole test bar:

$$Q_{corr} = \frac{W_o - W_1 + (W_{n0} - W_{n1})}{W_o} \times 100\% \quad (2.6)$$

where:

- $Q_{corr}$  - Amount of corrosion reinforcement (%)
- $W_o$  - Weight of reinforcement prior to corrosion (gram)
- $W_1$  - Weight of reinforcement after it was corroded and cleaned in acid solution (gram)
- $W_{n0}$  - Weight of non-corroded reinforcement before it was cleaned in acid solution (gram)
- $W_{n1}$  - Weight of the same non-corroded reinforcement after it was cleaned in acid solution (gram)

An acid solution was used to clean the bar after the corrosion process. Therefore, Equation 2.6 provides greater accuracy than Equation 2.5 by considering the weight loss from the acid erosion.

The mass loss can be converted to the steel cross-section loss through the following equation [2.41]:

$$\Delta A_s = \frac{\Delta m}{m} A_s \quad (2.7)$$

where

- $\Delta A_s$  - Steel cross-section loss ( $\text{mm}^2$ )
- $\Delta m$  - Mass loss per unit length ( $\text{kg/mm}$ )

$m$	-	Reference mass per unit length (kg/mm)
$A_s$	-	Sound steel cross section (mm <sup>2</sup> )

## 2.4 Structural Effects of Corrosion

Many experiments have been conducted to investigate the effects of corrosion on the overall performance of an RC member. Castel et al. [2.42] showed that the stiffness deterioration in the response of a corroded beam depends on the interaction of bar-section reduction and bond deterioration. According to Coronelli and Gambarova [2.43], the flexural behavior of a corroded beam is affected not only by the loss of concrete and steel section but also by bond decay. Corrosion affects the strength and the ductility of the structure at ultimate load because it reduces the steel elongation at maximum load.

The effects of corrosion on a reinforced concrete member can be divided into three categories: those on the loss of the bar cross-section, those on the surrounding concrete, and those on the interaction (or bond) between the bar and concrete [2.36]. The consequence of each of these aspects and their inter-related effect on the load-carrying capacity of reinforced concrete structures are shown in Figure 2.10. Therefore, in addressing the problem related to corroded reinforcing bars in concrete, these three main parameters, such as the loss of bar section, cover cracking, and bond degradation, should be considered.

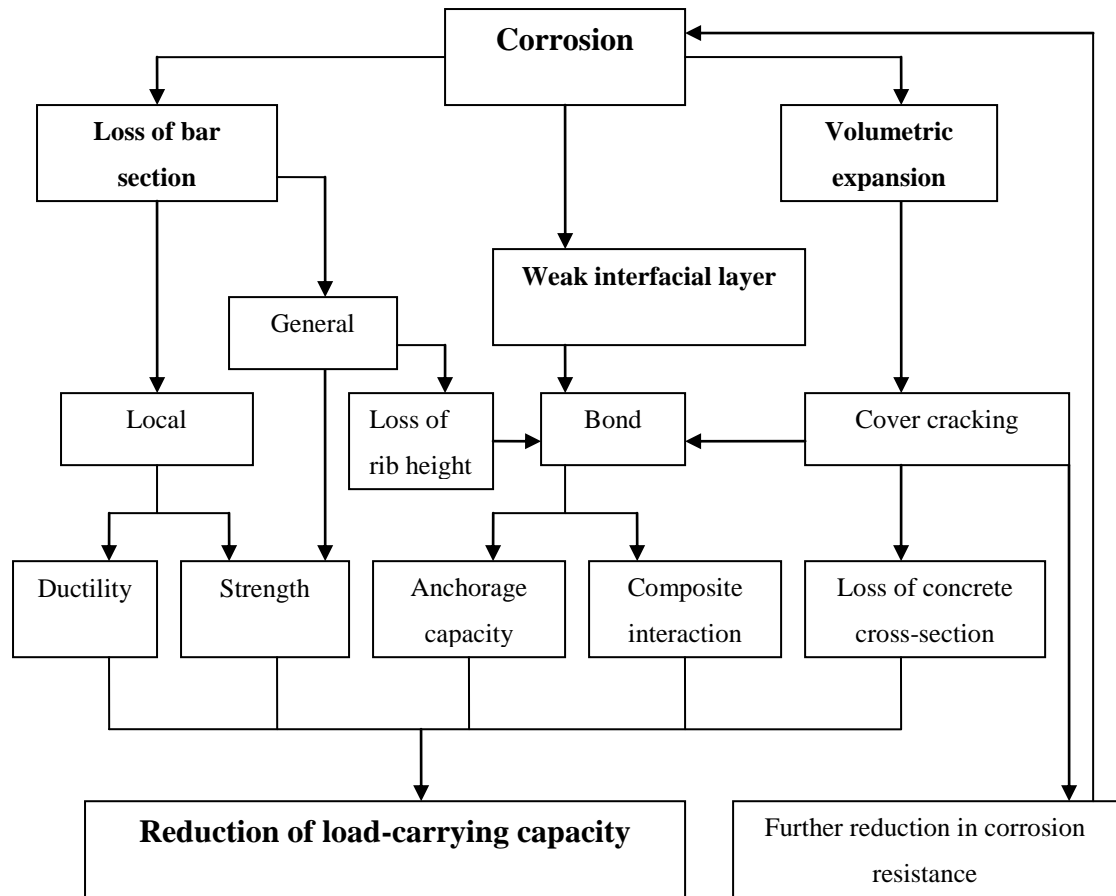


Figure 2.10: Effects of reinforcement corrosion on residual structural capacity [2.36]

#### 2.4.1 Loss of bar section

Several experimental studies have investigated the effects of corrosion on the mechanical behavior of steel bars [2.42] [2.44]. According to Andrade et al. [2.45], a reduction in the bar section of between 10% and 25% in the critical zones of the structure means the depletion of its residual service life, whereas a reduction of up to 5% (with cracking and spalling) indicates an early stage of deterioration.

The experimental work by Almusallam [2.5] on the effects of corrosion on the mechanical properties of steel reinforcement indicates that the corresponding elongation of the bar before failure decreases as the degree of corrosion increases. It also shows that the corrosion of 12.6% or more increases steel reinforcement brittleness. Conversely, the corrosion generated from an atmospheric exposure of up to 16 months showed no effects on yield and ultimate tensile strength, as tested by Maslehuddin et al. [2.46]. However, in the present work, the amount of section loss was small, and the maximum diameter

reduction was only 0.53%. Du et al. [2.47] concluded that corrosion alters the external surface of the reinforcement, and that the residual section is no longer round and varies considerably along its circumference and length. A linear regression from the experimental data of the researchers shows that a 10% section loss reduced yield and ultimate forces by about 14% and 15% respectively for bare bars and bars in the concrete. A study on the mechanical properties of corrosion-damaged reinforcement shows that the reduction in yield strength was less than the reduction in cross-sectional area for a plain mild bar subjected to a light corrosion (up to 7% section loss) [2.48]. The reduction in ductility was greater than the reduction in yield strength for plain and high-yield bars, with 8% section loss reducing ductility by 20%.

#### ***2.4.2 Loss of bond***

Two mechanisms are involved where corrosion may affect the bond between reinforcing bars and concrete [2.8]. First, the corrosion products that accumulate on the bar surface occupy a larger volume than the original uncorroded metal, thereby causing the cracking or spalling of the concrete cover. The loss of the concrete cover inevitably implies the loss of confinement and a reduction in bond strength at the interface zone between the two materials. The surface of the bar also becomes covered with corrosion products, an outcome that interferes with the development of bond mechanisms that rely on adhesion on the bar surface.

The degradation of the anchorage bond of reinforcing bars caused by corrosion has been investigated by various researchers. Several experiments have been conducted to understand the degradation behavior and identify the distress parameters that contribute directly to the degradation. Therefore, in plain bars, two mechanisms may be responsible for the loss of bond as a result of corrosion [2.36]:

- i) A mechanically weak layer of corrosion product at the steel or concrete interface;
- ii) A reduction in the confinement as cover cracks develop along the bar owing to the volumetric expansion of the products of corrosion.

A test conducted by Morinaga [2.49] shows that the influence of corrosion on bond strength was different between plain round and deformed bars. For plain round bars, bond strength was determined mainly by the adhesive force between the concrete and the bar

surface, whereas for deformed bars, the key action of the ribs on the surface of the bar was not affected by the corrosion. The author assumed no distinctly negative influence of corrosion on bond strength until the amount of corrosion reached the cracking level. Furthermore, Cairns et al. [2.50] conducted friction tests to measure the change in the coefficient of friction between steel plates and concrete as a result of corrosion. They found no evidence to support the notion that these corrosion products produce a mechanically weak layer at the bar–concrete interface (corrosion range between 0.07 and 0.23 mm of section loss).

The general trend of changes in the bond strength after corrosion has been initiated is presented in Figure 2.11 [2.18], although exceptions in certain circumstances exist, which will be described later. Initially, the bond strength is increased by a small amount of corrosion but starts to decrease with a further increase in the corrosion level.

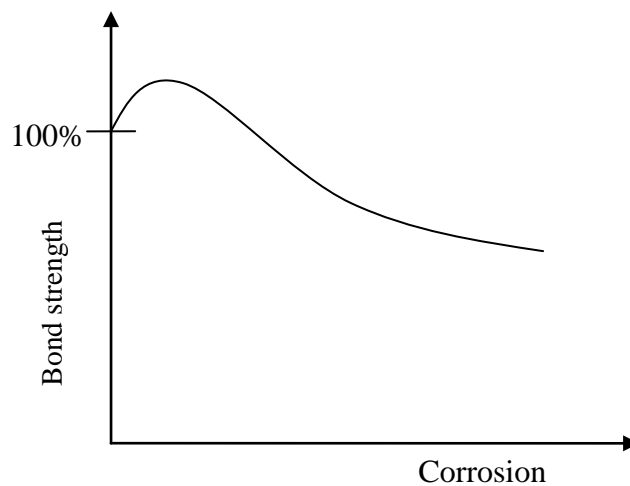


Figure 2.11: Bond strength versus corrosion

This trend was observed by Cabrera and Ghoddoussi [2.51], Al-Sulaimani et al. [2.29], and Choi et al. [2.52]. They used the same size of pullout specimens (150 mm x 150 mm) reinforced with different bar diameters. The results for both specimens showed that the bond strength increased when the corrosion level increased up to 1% section loss and decreased with further corrosion. The bond strength enhancement in the early stage of corrosion was inversely related to the bar diameter, as shown in the work of Al-Sulaimani. Three bar diameters, which imply different ratios of cover to diameter, were

used, where the 10 mm bar showed the highest increase (56% with 0.87% section loss), followed by the 14 and 20 mm diameter bars (32% and 27% respectively, corresponding to 0.9% and 0.65% section loss). The decrease in bond strength was conversely related to the bar diameter when the corrosion level reached around 4% section loss. The 20 mm bar produced a 48% decrease, followed by the 14 and 10 mm bars (8% and 5% bond loss respectively).

In Cabrera and Ghoddoussi [2.51], only a 12 mm bar diameter was used in the test and yielded approximately 17% increase in the bond strength (0.71% section loss), which then decreased by 36% when the corrosion level exceeded 10% section loss.

A similar trend was observed by Auyeung et al. [2.53]. They used axial tension pullout test specimens to study the bond behavior of corroded reinforcement bars. After 1% of corrosion, the bond strength decreased rapidly. More realistic test specimens (Figure 2.8) were used by Almusallam et al. [2.19], where open stirrups were provided to avoid shear failure during the bond test. They found that up to 4% of weight loss resulted in a 16% increase in the bond strength, which then decreased as the amount of corrosion increased. At 8% corrosion (post-cracking stage), the bond strength was almost 30% lower than that of uncorroded specimens.

Pullout tests conducted by Fang et al. [2.34] on specimens confined by two 6 mm diameter closed stirrups at 40 mm spacing showed no obvious degradation in the bond strength. When the degree of corrosion was 6%, the bond strength decreased by only 12%, which was significantly lower than the value for the unconfined specimens reported previously. Other tests were conducted on 24 specimens reinforced with 20 mm hot-rolled deformed steel bars with an 80 mm embedment length (Fang et al.) [2.39]. These confined and unconfined specimens were corroded to varying degrees, from 0% (no corrosion) to 6% mass loss. The experimental results were compared with analytical results from nonlinear finite element analysis. They found that confinement supplied an effective method of counteracting bond loss for corroded steel bars at a medium corrosion level (around 4% – 6% mass loss). The experiment and analysis showed that the bond strength of unconfined steel bars was 30% – 65% lower than that of confined steel bars for a similar corrosion level. For a high corrosion level, Kivell et al. [2.54] showed that a 16% loss of bar section resulted in over 50% reduction in bond strength and that the slip at peak load dropped almost 95% between the corroded and uncorroded specimens.

Another pullout test conducted by Tondolo [2.55] on 120 mm × 120 mm × 120 mm specimens reinforced with 12 mm diameter bars showed that the bond strength of corroded confined specimens was 144% higher than that of non-corroded specimens at 20% mass loss. For unconfined specimens, the residual corroded bond strength at 23% mass loss was 24% compared with the control specimen.

Rodriguez et al. [2.37] studied the effects of corrosion on bond strength for different bar positions, stirrup amounts, and cover thicknesses. They showed almost no influence of the amount of stirrup on the bond strength in uncorroded specimens. The bond strength values of highly corroded bars in specimens without stirrups were close to zero, while the presence of the stirrup resulted in a residual strength value of 3.0 – 4.0 MPa. According to a statistical study of the experimental data of the researchers, bond strength can be predicted through the following equation, which is based on the ratio of the transverse reinforcement area at anchorage length,  $\rho$ .

For  $\rho$  higher than 0.25,

$$f_b = 4.75 - 4.64x \quad (2.8)$$

If  $\rho$  lower than 0.25

$$f_b = 10.04 + [-6.62 + 1.98\left(\frac{\rho}{0.25}\right)][1.14 + x] \quad (2.9)$$

where  $f_b$  - Bond strength  
 $x$  - Attack penetration (bar radius decrease) in mm

This relationship shows that the presence of stirrups significantly influences the bond strength in corroded beams by maintaining the confining pressure around the main reinforcement as the contribution from the concrete cover drops after cracking has initiated. However, this expression underestimates the bond strength at  $x = 0$ . In other words, uncorroded bond strength is not accurately predicted, as shown in Figure 2.12. The average bond strength in uncorroded conditions from the tests of the researchers was almost 27% higher than the calculated value from the equation. Therefore, some precautions should be taken when this equation is used in the analysis, as it would tend to underestimate the reduction in bond strength as a consequence of corrosion.

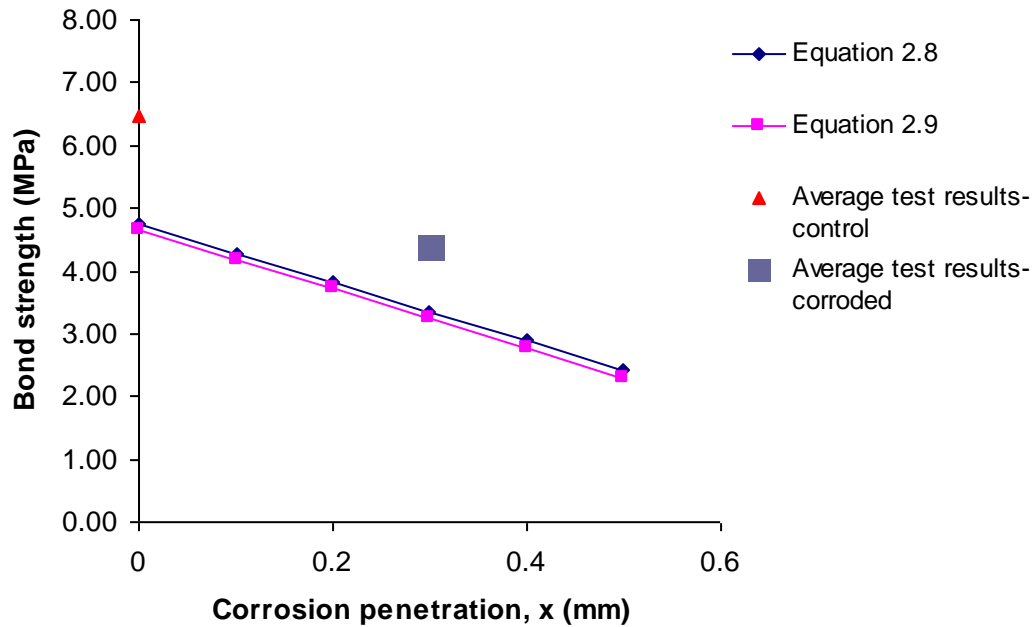


Figure 2.12: Bond strength versus corrosion penetration based on Equations 2.8 ( $\rho > 0.25$ ) and 2.9 ( $\rho < 0.25$ )

Williamson and Clark [2.56] considered five variables, namely, level of corrosion, pre-load, cover depth, bar type (plain and deformed), and specimen age, in studying the effects of corrosion on bond strength. They found that pre-loading the bar in tension during the corrosion process affected only deformed bar specimens with the greatest cover thickness. At 20% corrosion with a cover-to-diameter ratio of 2, the appearance of extensive cracks had slight effects on the bond strength compared with uncorroded specimens.

A summary of bond test results from various researchers is given in Table 2.2. The impressed current value ranges from  $0.01\text{mA}/\text{cm}^2$  to  $10\text{mA}/\text{cm}^2$ , but no significant trend is observed on the influence of impressed current on bond strength. However, if the degradation of bond strength is assumed to be linear with the severity of corrosion, a lower current tends to produce higher bond strength degradation than a higher current, as observed by Saifullah and Clark. In terms of crack width, no clear relationship exists with bond strength reduction except for specimens without links and crack width greater than 1 mm because link reinforcement is very important in maintaining bond strength after longitudinal cracking.



Researchers	$\phi_b$ (mm)	$\frac{c}{\phi_b}$ ratio	Corrosion rate (mA/cm <sup>2</sup> )	Link ?	Crack width (mm)	Section loss (%)	Residual $f_b$ (%)
Al-Sulaimani et al. [2.29]	10	3.75	2	N	-	7.8	17
	14	5.36	2	N	-	6.5	25
	20	7.5	2	N	-	4.35	53
Cabrera and Ghodussi [2.51]	12	5.75	3 volts	N	0.6	12.6	24
Saifullah and Clark [2.31]	8	1.0	0.04	N	-	12.5	60
	8	1.0	0.25	N	-	12.5	105
	8	1.0	4	N	-	12.5	50
Rodriguez et al. [2.16]	16	1.5	0.1	N	1.6-2.2	5.4-9.1	20
	16	1.5-2.5	0.1	Y	1.0-2.0	5.4-9.1	65
	16	1.5	0.1	Y	1.1-1.4	14	75
Almusallam et al. [2.19]	12	5.0	10	N	0.4	8.0	15

Table 2.2: Summary of bond test results as derived from fib Bulletin 10 [2.18]

### 2.4.3 Loss of concrete section

Loss of concrete section is another effect of reinforcement corrosion. The spalling of the concrete cover reduces the confinement around the reinforcing bars, thus reducing the bond strength between the steel bar and concrete. In beams, spalling exposes the main reinforcement and therefore reduces the composite action between concrete and steel reinforcing bars [2.57]. The neutral axis depth is reduced at the section of maximum moment, and consequently, the maximum compressive strain in the concrete increases. In a concrete column, the loss of cover can have a significantly greater effect on axial strength than the loss of bar section.

## 2.5 Corrosion-induced Surface Cracks

The appearance of surface cracks in corroded structures results from the volumetric expansion of corrosion products around the reinforcing bars. This volumetric expansion depends on the type of oxide, the degree of hydration, and the dispersion of corrosion products into the surrounding pore structure [2.38]. When corrosion begins, it progresses by causing an expansion of the rust produced in the vicinity of the rebar. Longitudinal corrosion cracks form along the corroded reinforcing bars when the tensile stress in the concrete surrounding the rebar exceeds the tensile strength of the concrete [2.6]. These cracks cause the loss of concrete integrity, which reduces the concrete contribution to the load-bearing capacity and affects the external appearance of the structure [2.37].

Experiments were conducted by Andrade et al. [2.24] to identify the influence of bar location, impressed current intensity, and cover thickness on surface cracks as a function of rebar corrosion. They found that 20  $\mu\text{m}$  of bar radius lost to corrosion was needed to induce a surface crack, but the cover-to-diameter ratio had no influence on the cracking initiation time. The influence of corrosion on crack initiation was discussed previously in the fib Bulletin 10 [2.18] and is tabulated in Table 2.3. In general, high amounts of corrosion induced by high impressed currents are required to initiate cracks on a thick concrete cover.

Regarding crack propagation, Rodriguez et al. [2.37] mentioned that crack evolution depends mainly on the position of the bar in a concrete element (top or bottom cast position) and on the corrosion intensity  $i_{corr}$ . However, this influence was negligible for usual corrosion intensity values ranging from 0.1 to 2  $\mu\text{m}/\text{cm}^2$ . They developed an empirical expression from their experimental results on different casting positions, where crack width as a function of attack penetration was derived as follows:

$$w_{cr} = 0.05\beta[x - x_0] \quad (w_{cr} \leq 1.0 \text{ mm}) \quad (2.10)$$

where  $w_{cr}$  is the crack width in mm,  $x$  is the attack penetration in micron,  $x_0$  is the attack penetration corresponding to crack initiation, and  $\beta$  is a coefficient that depends on the bar position ( $\beta = 0.01$  for a top cast bar and 0.0125 for a bottom cast bar).

Researchers	$\phi_b$ (mm)	$\frac{c}{\phi_b}$ ratio	Impressed current (mA/cm <sup>2</sup> )	Crack width (mm)	Section loss (%)	Corrosion penetration (mm)
Al-Sulaimani et al. [2.28]	10	7.5	2	-	5	0.13
	14	5.36	2		3	0.11
	20	3.75	2		2	0.10
Cabrera and Ghoddoussi [2.50]	12	5.75	3 Volts	0.2	1-2	0.03-0.06
Clark and Saifullah [2.55]	8	0.5	0.5		0.4	0.008
	8	1.0	0.5		0.6	0.012
	8	2.0	0.5		1.3	0.026
Andrade et al. [2.23]	16	1.25-1.88	0.1	0.05	0.4-0.48	0.015-0.018
		1.25	0.01	< 0.05	0.43	0.017
Saifullah and Clark [2.40]	8	1.0	0.04	-	1.1	0.022
	8	1.0	0.25		0.78	0.016
	8	1.0	2		0.3	0.006
Rodriguez et al. [2.16]	16	2.0-4.0	0.003-0.10	-	0.4- 1.0	0.015- 0.04
Almusallam et al. [2.18]	12	5.0	10	-	4.0	0.12

Table 2.3: Amount of corrosion to initiate crack of concrete cover [2.18]

Alonso et al. [2.38] found a linear relationship between crack width growth and radius loss during the propagation period of the crack. In conclusion, they summarized the evolution of crack width as shown in Table 2.4.

Variable	Time of evolution of the crack for the same attack penetration	
	Initiation	Propagation
Increases $i_{corr}$	Indifferent	Increases $i_{corr}$
Increase $c/\phi_b$	Longer	Increase $c/\phi_b$
Increase porosity	Longer	Increase porosity
Stirrup (isolated)	Indifferent	Stirrup (isolated)

Table 2.4: Influence of several parameters on the initiation and propagation of crack width [2.38]

Vidal et al. [2.41], basing on their observation of two beams that naturally corroded over periods of 14 years and 17 years, found that the attack penetration calculated from the pit penetration and the diameter decrease caused by corrosion gave a good prediction of crack initiation but not of crack propagation. This finding was due to the fact that the attack penetration used in their study was derived from the pitting condition from several experimental data. To some extent, those data were limited to a certain bar diameter and the corrosion products only. Therefore, they proposed using section loss, which was calculated from the actual mass loss after the corrosion process. This corrosion measurement yielded more accurate results than corrosion penetration. The authors concluded that longitudinal crack initiation mainly depended on the cover-to-diameter ratio and the bar diameter, although the quality of the steel concrete interface might have some effects as well. However, on crack propagation, the cover-to-diameter ratio and the bar diameter seemed to have no effect.

In some cases of confined specimens, stirrups were corroded during the corrosion conditioning process. Khan et al. [2.59] showed that the presence of corrosion on the stirrup had no effects on the relationship between the crack width and cross-section loss of the longitudinal bars. Therefore, using a longitudinal corrosion crack as a reference for the corrosion of the stirrup is not possible.

Several studies have been conducted to investigate the influence of surface cracks on bond strength reduction. For plain bars, longitudinal cracking reduced the confining pressure on the bar interface, which reduced the bond strength, as shown by Cairns et al. [2.36] for specimens without links. This condition was not observed in specimens with links because the confining pressure was maintained by the links. The relationship

between the bond strength of the corroded specimens and the crack width from different casting positions is shown as follows:

$$f_{b,corroded} = \frac{f_b}{(1+0.8w_{cr})} \quad \text{for a bottom cast bar} \quad (2.11)$$

$$f_{b,corroded} \leq \frac{f_b}{(0.5+1.6w_{cr})} \quad \text{for a top cast bar} \quad (2.12)$$

where:

- $f_{b,corroded}$  – Corroded bond strength
- $f_b$  – Design bond strength
- $w_{cr}$  – Maximum width of longitudinal cover crack

For deformed bars, Almusallam et al. [2.19] reported that in the initial stage of crack formation (approximately 0.2 mm wide), the ultimate bond load was decreased by around 60% of the uncorroded value. After a certain degree of corrosion, the effects of crack width on bond strength was insignificant because of sufficiently wide cracks. The reinforcing bars had already lost much of their confinement, and a further increase in crack width did not cause any further reduction in the confining pressure.

## 2.6 Conclusions

Several conclusions have been made based on the results and discussions from previous investigations that can be used as guidelines in this study:

- i) Three mechanisms, namely, cover cracking, bar section loss, and bond strength deterioration, were identified to influence the reduction of the residual capacity of a corroded RC structure. However, no research has been conducted to determine the parameter that correlates best with the reduction in each mechanism.
- ii) Different bond test methods have been used by different researchers to study the bond strength of reinforcement in concrete. From the wide range of choices, the beam end type specimen was shown to be a suitable test for bond testing because it evaluated behavior in a splitting failure mechanism, thus allowing the researcher to obtain realistic bond strength values that could be used to design and assess concrete structures. In addition to ease of handling, it provides a direct comparison of bond strength for top cast and bottom cast

positions and from different corner and center locations of the bar. Another advantage is that it can handle more than one test bar for each specimen and is thus economical.

- iii) Mass loss or section loss (%) and attack penetration (mm) are the two main parameters used by previous researchers to quantify the degradation of a bar section caused by corrosion. However, using these different parameters leads to confusing and inconsistent interpretation of experimental results in the report.
- iv) The results show that an attack penetration with a value of 0.1 mm, for example, results in markedly different section losses in 8 and 40 mm diameter bars. Hence, making comparisons across several studies, where different corrosion parameters have been used to quantify degradation, is difficult.
- v) To obtain reasonable and comparable results, a range of cover-to-main bar diameters should be based on previous studies. A thick cover will spall even with small cracks, whereas a thin cover will make the bond strength unacceptable as a result of too little confinement. Therefore, a suitable cover thickness should be used in this study as a function of the main bar diameter.
- vi) This study is focused on the bond strength in specimens with stirrups because it produces realistic data similar to actual conditions. It also provides added value to the existing knowledge.
- vii) Previous studies have demonstrated that the impressed current method is the best choice for accelerating corrosion tests of reinforcing bars within a reasonable time. However, the impressed current density should be selected carefully because a value that is too high will result in the misinterpretation of the crack and bond results, whereas a value that is too low will extend the time required for the tests.
- viii) Theoretical section loss was calculated from the total impressed current, whereas actual section loss was calculated from the weight loss of steel reinforcement after the corrosion. Both approaches are used in the current study, where the actual section loss is used to check or validate the theoretical value.
- ix) As discussed previously, 0.4% and 4% section losses were enough to induce a surface crack and reduce the bond strength in corroded specimens. Therefore, these corrosion levels can be used as a guideline for limiting the corrosion level in the current study.

## 2.7 References

- [2.1] I. Biczok, *Concrete corrosion concrete protection*, 8<sup>th</sup> Edition. Akademiai Kiado, Budapest (1964)
- [2.2] V.R. Pludek, *Design and corrosion control*, The Gresham Press, Surrey, UK (1977)
- [2.3] S.J. Pantazopoulou, and K.D. Papoulia, *Modeling cover-cracking due to reinforcement corrosion in RC structures*, Journal of Engineering Mechanics, **127**, 4, 342-351 (2001)
- [2.4] J.P. Broomfield, *Corrosion of steel in concrete, understanding, investigation and repair*, E & FN Spon, London (1997)
- [2.5] A.A. Almusallam, *Effects of degree of corrosion on the properties of reinforcing steel bars*, Construction and Building Materials, **15**, 361-368 (2001)
- [2.6] S. Bentur, S. Diamond and N.S. Berke, *Steel corrosion in concrete: Fundamental and civil engineering practice*, E & FN Spon, London (1997)
- [2.7] P.F. Marquest and A. Costa (2010), *Service life of RC structures: Carbonation induced corrosion. Prescriptive vs. performance-based methodologies*, Construction and Building Materials, **24**, 258-265 (2010)
- [2.8] K. Stanish, R.D. Hooton and S.J. Pantazopoulou, *Corrosion effects on bond strength in reinforced concrete*, ACI Structural Journal, **96**, 6, 915-921 (1999)
- [2.9] A.W. Beeby, *Cracking, cover and corrosion of reinforcement*, Concrete International Design and Construction, **5**, 2, 35-40 (1983)
- [2.10] C. Cao, M.M.S. Cheung and B.Y.B. Chan, *Modelling of interaction between corrosion-induced concrete cover crack and steel corrosion rate*, Corrosion Science, **69**, 97-109 (2013)
- [2.11] M. Raupach, *Chloride-induced macrocell corrosion of steel in concrete – theoretical background and practical consequences*, Construction and Building Materials, **10**, 5, 329-338 (1996)
- [2.12] S. Ahmad, *Reinforcement corrosion in concrete structures, its monitoring and service life prediction – a review*, Cement and Concrete Composite, **25**, 459-471 (2003)

- [2.13] A.K. Azad, S. Ahmad, and S.A. Azher, *Residual strength of corrosion-damaged reinforced concrete beams*, ACI Materials Journals, **104**, 1, 40-47 (2007)
- [2.14] K. Lundgren, *Bond between ribbed bars and concrete. Part 1: Modified model*, Magazine of concrete research, **57**, 7, 371-382 (2005)
- [2.15] R. Tepfers, *Cracking of concrete cover along anchored deformed reinforcing bars*, Magazine of Concrete Research, **31**, 106, 3-12 (1979)
- [2.16] J. Rodriguez, L.M. Ortega and J. Casal, *Corrosion of reinforcing bars and service life of reinforced concrete structures: Corrosion and bond deterioration*, International Conference on Concrete across Borders, Odense Denmark, **2**, 315-326 (1994)
- [2.17] T.J. MacGinley, and B.S. Choo, *Reinforced concrete: design, theory and examples*, E & FN Spon, London (1990)
- [2.18] *fib Bulletin 10, 'Bond of corroded reinforcement', Chapter 4, "Bond of reinforcement in concrete"*, pp 187-212. Lausanne (2000). ISSN 1562-3610, ISBN 2-88394-050-9
- [2.19] A.A. Almusallam, A.S.Al-Gathani, A.R. Aziz, and Rasheeduzzafar, *Effects of reinforcement corrosion on bond strength*, Construction and Building Materials, **10**, 2, 123-129 (1996)
- [2.20] P.M. Ferguson, *Reinforced concrete fundamentals*, 4<sup>th</sup> Edition, John Wiley, New York (1979)
- [2.21] P.S. Chana, *A test method to establish realistic bond stresses*, Magazine of Concrete Research, **42**, 151, 83-90 (1990)
- [2.22] E.L. Kemp, *Bond in reinforced concrete: Behavior and design criteria*, Journal of the American Concrete Institute, **83**, 1, 50-57 (1986)
- [2.23] S.A. Austin, R. Lyons and M.J. Ing, *Electrochemical behaviour of steel-reinforced concrete during accelerated corrosion testing*, Corrosion, **60**, 2, 203-212 (2004)
- [2.24] C. Andrade, C. Alonso, and F.J. Molina, *Cover cracking as a function of bar corrosion: Part 1 – Experimental test*, Materials and Structure, **26**, 453-464 (1993)
- [2.25] J. Rodriguez, L.M. Ortega and J. Casal, *Load carrying capacity of concrete structures with corroded reinforcement*, Construction and Building Materials, **11**, 4, 239-248 (1997)



- [2.26] C. Andrade, and C. Alonso, *Corrosion rate monitoring in the laboratory and on-site*, Construction and Building Materials, **10**, 5, 315-328 (1996)
- [2.27] C. Andrade, C. Alonso, J. Rodriguez, and M. Garcia, *Cover cracking and amount of rebar corrosion: Importance of the current applied accelerated test*, Concrete Repair, Rehabilitation and Protection, Edited by R.K. Dhir and M.R. Jones, E & FN Spon, London (1996)
- [2.28] R. Huang, and C.C. Yang, *Condition assessment of reinforced concrete beams relative to reinforcement corrosion*, Cement and Concrete Composite, **19**, 131-137 (1997)
- [2.29] G.J. Al-Sulaimani, M. Kaleemullah, I.A. Basunbul and Rasheeduzzafar, *Influence of corrosion and cracking on bond behaviour and strength of reinforced concrete members*, ACI Structural Journal, **87**, 2, 220-231 (1990)
- [2.30] Rasheeduzzafar, S.S. Al-Saadoun and A.S. Gahtani, *Corrosion cracking in relation to bar diameter, cover and concrete quality*, Journal of Materials in Civil Engineering, **4**, 4, 327-342 (1992)
- [2.31] M. Saifullah, and L.A. Clark, *Effect of corrosion rate on the bond strength of corroded reinforcement*, Corrosion and Corrosion Protection of Steel in Concrete, Sheffield Academic Press, UK (1994)
- [2.32] Y. Liu, and R.E. Weyers, *Modelling the time-to-corrosion cracking in chloride contaminated reinforced concrete structures*, ACI Materials Journal, **96**, 6, 675-681 (1998)
- [2.33] T.A. El Maaddawy and K.A. Soudki, *Effectiveness of impressed current technique to stimulate corrosion of steel reinforcement in concrete*, Journal of Materials in Civil Engineering, **15**, 1, 41-47 (2003)
- [2.34] C. Fang, K. Lundgren, L. Chen, and C. Zhu, *Corrosion influence on bond in reinforced concrete*, Cement and Concrete Research, **34**, 2159-2167 (2004)
- [2.35] M. Badawi, and K.A. Soudki, *Control of corrosion-induced damage in reinforced concrete beams using carbon fiber-reinforced polymer laminates*, Journal of Composite for Construction, **9**, 2, 195-201 (2005)
- [2.36] J. Cairns, Y. Du and D. Law, *Residual bond strength of corroded plain round bars*, Magazine of Concrete Research, **58**, 4, 221-231 (2006)

- [2.37] J. Rodriguez, L.M. Ortega, J. Casal, and J.M. Diez, *Corrosion of reinforcement and service life of concrete structures*, Durability of Building Materials and Components **7**, 1, 117-126 (1996)
- [2.38] C. Alonso, C. Andrade, J. Rodriguez, and J.M. Diez, *Factors controlling cracking of concrete affected by reinforcement corrosion*, Materials and Structures, **31**, 435-441 (1998)
- [2.39] C. Fang, K. Lundgren, M. Plos, and K. Gylltoft, *Bond behaviour of corroded reinforcing steel bars in concrete*, Cement and Concrete Research, **36**, 1931-1938 (2006)
- [2.40] Y.G. Du, L.A. Clark and A.H.C. Chan, *Residual capacity of corroded reinforcing bars*, Magazine of Concrete Research, **57**, 3, 135-147 (2005)
- [2.41] T. Vidal, A. Castel, and R. Francois, *Analyzing crack width to predict corrosion in reinforced concrete*, Cement and Concrete Research, **34**, 165-174 (2004)
- [2.42] A. Castel, R. Francois and G. Arliguie, *Mechanical behavior of corroded reinforced concrete beams. II: Bond and notch effects.* Material Structure., **33**, 545-551 (2000)
- [2.43] D. Coronelli, and P. Gambarova, *Structural assessment of corroded reinforced concrete beams: modeling guideline*, Journal of Structural Engineering, **130**, 8, 1214-1224 (2004)
- [2.44] R. Palsson and M.S. Mirza, *Mechanical response of corroded steel reinforcement of abandoned concrete bridge*, ACI Structural. Journal, **99**, 2, 157-162 (2002)
- [2.45] C. Andrade, C. Alonso, D. Garcia and J. Rodriguez, *Remaining service lifetime of reinforced concrete structures: effect of corrosion in the mechanical properties of the steel*, Symposium on Life Prediction of Corrodible Structures, NACE, Cambridge, 12/1-12/11 (1991)
- [2.46] M. Maslehuddin, I.A. Allam, J. Al-Sulaimani, A.I. Al-Mana and S.N. Abduljawwad, *Effect of rusting of reinforcing steel on its mechanical properties and bond with concrete*, ACI Materials Journal, **87**, 5, 496-502 (1990)
- [2.47] Y.G. Du, L.A. Clark, and A.H.C. Chan, *Effect of corrosion on ductility of reinforcing bars*, Magazine of Concrete Research, **57**, 7, 407-419 (2005)

- [2.48] J. Cairns, G.A. Plizzari, Y. Du, D.W. Law and C. Franzoni, *Mechanical properties of corrosion-damaged reinforcement*, ACI Materials Journal, **102**, 4, 256-264 (2005)
- [2.49] S. Morinaga, *Prediction of service lives of reinforced concrete buildings based on rate of corrosion of reinforcing steel*, Institute of Technology Shimizu Corporation, Special Report No 23 (1998)
- [2.50] J. Cairns, Y. Du and D. Law, *Influence of corrosion on the friction characteristic of the steel/concrete interface*, Construction and Building Materials, **21**, 190-197 (2007)
- [2.51] J.G. Cabrera and P. Ghoddoussi, *The effects of reinforcement corrosion on the strength of the steel/concrete "bond"*, Proceeding International Conference on Bond in Concrete: From Research to Practice, Riga Latvia, 10.11-10.24 (1992)
- [2.52] Y.S. Choi, S. Yi, M.Y. Kim, W.Y. Jung and E.I. Yang, *Effect of corrosion method of the reinforcing bar on bond characteristics in reinforced concrete specimens*, Construction and Building Materials **54** 180-189 (2014)
- [2.53] Y. Auyeung, P. Balaguru, and L. Chung, *Bond behaviour of corroded reinforcement bars*, ACI Materials Journal, **97**, 2, 214-220 (2000)
- [2.54] A. Kivell, A. Palermo and A. Scott, *Effects of bond deterioration due to corrosion in reinforced concrete*, Proceeding of the Ninth Pacific Conference on Earthquake Engineering, Building an Earthquake-Resilient Society, Auckland, New Zealand (2011)
- [2.55] F. Tondolo, *Bond behaviour with reinforcement corrosion*, Construction and Building Materials, **93**, 926-932 (2015)
- [2.56] S.J. Williamson and L.A. Clark, *Effects of corrosion and load on reinforcement bond strength*, Structural Engineering International: Journal of the International Association for Bridge and Structural Engineering (IABSE), **12**, 2, 117-122 (2002)
- [2.57] J. Cairns and Z. Zhao, *Behaviour of concrete beams with exposed reinforcement*, Proceedings of the Institute of Civil Engineers: Structures and Buildings, **99**, 2, 141-154 (1993)
- [2.58] L.A. Clark and M. Saifullah, *Effect of corrosion on reinforcement bond strength*, Proceeding Conference on Structural Faults & Repair, Ed Forde M. Engineering Technics Press, Edinburgh, **3**, 113-119 (1993)

- [2.59] I. Khan, R. Francois and A. Castel, *Prediction of reinforcement corrosion using corrosion induced cracks width in corroded reinforced concrete beams*, Cement and Concrete Research, **56**, 84-96 (2014)

# CHAPTER 3 – NUMERICAL ANALYSIS OF CORROSION-INDUCED CRACKING

## 3.1 Introduction

Computer simulation is one of the approaches that can be used to study the effects of corroded reinforcement on concrete structures. Several researchers have used finite element (FE) software to investigate the relationship between corrosion parameters, such as attack penetration and loss of steel section, and deterioration parameters such as cracking and spalling, which affect the residual capacity of concrete structures [3.1] [3.2].

The objective of using numerical analysis in the current study is to understand the effects of corrosion expansion on the surface crack width. Furthermore, the study should help to determine parameters for the experimental investigation.

This chapter starts with a literature review of previous works on corrosion-induced crack modelling, such as the parameters considered, idealisation of the expansion of corrosion products and crack modelling. The output from the previous works will be used to model specimens with different bar diameters and bar locations using a finite element approach. The results from the finite element analyses will be discussed subsequently.

## 3.2 Review of Previous Studies

### *3.2.1 Corrosion-induced crack model*

Various approaches have been used in modelling the initiation of surface cracks induced by reinforcement corrosion. The first model was proposed by Bazant [3.3], who modelled the concrete cover as a thick-wall cylinder subjected to internal pressure from the volume expansion of corrosion products. This internal pressure was derived from plane-strain isotropic linear elastic assumptions, according to which cracking occurred when the peak stress reached the tensile strength of concrete. The model proposed by Bazant predicted mainly the time to cover cracking; however, this model was not validated experimentally. In this model, the time for corrosion crack initiation was based on the corrosion rate and

the properties of concrete, such as the modulus of elasticity and tensile strength, cover thickness, spacing between steel reinforcing bars, and diameter of the main reinforcement.

Bazant's model was subsequently upgraded by Liu and Weyers [3.4], Pantazopoulou and Papoulia [3.5], Bhargava et al. [3.6], and Allampallewar and Srividya [3.7] by assuming that a porous zone existed around the steel/concrete interface caused by air voids entrapped/entrained near the transition from cement paste to steel. As the corrosion takes place on the surface of the steel, the porous zone will gradually be filled with the corrosion products before corrosion begins to exert internal pressure.

In modelling the time of corrosion cracking, the amount of corrosion products needed to fill the porous zone was calculated based on the density of the corrosion products and the total volume of interconnected pores around the steel/concrete interface [3.4]. The pressure from corrosion products needed to generate the critical tensile stress that induces cracking of the concrete cover depends on the concrete properties, cover thickness, and volume of the corrosion product itself. In this model, the rate of rust growth was assumed to decrease in proportion to the amount of rust products. This happened because, when the rust layer thickens, the iron ionic diffusion distances increased and the rate of rust production decreased, as diffusion was inversely proportional to the oxide layer thickness. However, according to Chernin and Val [3.8], the solution in [3.4] was incorrect and violated Faraday's law of electrolysis.

Cracking time is found to be a function of the cover, material properties of the surrounding concrete, and rust product and is controlled by the rate of rust accumulation [3.5]. Ahmed et al. [3.9] used the boundary value problem and solved it using the finite differences method in modelling the crack initiation time. The build-up of rust around the bar was estimated from the anodic current density using two alternatives from the model proposed by Liu and Weyers and the Faraday's law model. Concrete was treated as an anisotropic nonlinear elastic material with post-cracking softening. The concrete cover was idealised as a thick-walled cylinder. They found that using Faraday's law in combination with a constant corrosion rate tends to produce an unrealistically short cracking time and that the composition of rust products resulting from accelerated corrosion may depend on the intensity of the imposed current.

Du et al. [3.2] [3.10] used two-dimensional finite element analysis to study the effects of the radial expansion of corroded reinforcement on the formation of surface cracks. They found that the radial expansion and corresponding internal pressure for penetration cracking depended on the thickness of the concrete cover. This is because an increase in the concrete cover reduces the tensile hoop stress at the bar surface in the concrete cover caused by the radial expansion of corroded reinforcement and therefore delays the occurrence of penetration cracking. The results from the numerical work were compared with experimental results on simulated corrosion specimens. This verification approach was used by Val et al. [3.11] in their numerical work on crack initiation.

Thoft-Christensen [3.12] used the finite element method to study the relationship between the volumes of corrosion product and crack width opening. He assumed that, after corrosion initiation in reinforcement, the cross-section of the reinforcement would decrease with time and the width of the crack would increase. The relationship between the volume of generated rust and the decrease in steel bar diameter was (for a small change in bar diameter) as follows:

$$\Delta V_{rust} = \alpha \frac{\pi}{2} \Delta \phi_b \phi_b l_c \quad (3.1)$$

where  $\Delta V_{rust}$  - Volume of generated rust

$\alpha$  - Volume fraction between the steel and rust products (Table 3.1)

$\Delta \phi_b$  - Reduction of bar diameter

$\phi_b$  - Initial bar diameter

$l_c$  - Length of corroded area

Corrosion products	Colour	$\alpha$
Fe <sub>3</sub> O <sub>4</sub>	Black	2.1
Fe(OH) <sub>2</sub>	White	3.8
Fe(OH) <sub>3</sub>	Brown	4.2
Fe(OH) <sub>3</sub> , 3H <sub>2</sub>	Yellow	6.4

Table 3.1: Value of  $\alpha$  for different corrosion products

This relation was based on the change in geometry ( $\Delta D < D$ ) from crack initiation, when the rust product fills up the porous zone to the crack opening when most rust products are present, as shown in Figure 3.1.

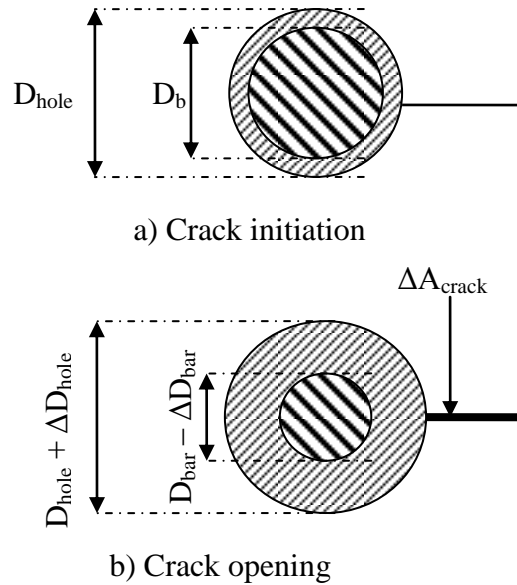


Figure 3.1: Crack at two different stages of cracking [3.11]

Besides 2D analysis, Thoft-Christensen et al. [3.13] used 3D modelling to evaluate the crack corrosion index for a reinforced concrete beam by assuming a concentrated corrosion area of the reinforcement. The crack corrosion index is the constant of proportionality between crack width and the reduction in bar diameter.

### 3.2.2 Corrosion modelling

Various approaches have been used in modelling corrosion in finite element analysis. One of the reasons is that corrosion is not a standard type of loading in FE codes. Therefore, a corrosion product is modelled based on its expansive behaviour characteristic.

Molina et al. [3.1] modelled steel corrosion based on two effects: a decrease in its stiffness and an increase in its specific volume. The first effect was achieved by linear variation of the properties of the material from those of the steel to those of the rust. Because of limited information relating to rust properties, they assumed Poisson's ratio and the bulk modulus of rust products as nearly equal to that of liquid water. The effects of the increase in specific volume were achieved by imposing an initial strain on the element being corroded.



Du et al. [3.2] modelled the expansive behaviour of reinforcement corrosion by an internal pressure for specimens used in simulated corrosion tests and by a radial expansion for those in accelerated tests. For internal pressure modelling, uniform pressure was applied to the internal surface of the rubber tube, and it was taken as a linear elastic material. Rubber tubing was used in the tests because its elastic range in tension is much greater than that of concrete and it is able to move freely outward, transferring the pressure to the concrete surface under the action of radial internal pressure. For radial expansion modelling of all nodes of the concrete elements around the corroding bar, a radial expansive displacement was prescribed. The cracking process of the concrete cover caused by the increasing radial expansion of corroded reinforcement was analysed for both uniform corrosion and non-uniform corrosion around the bar circumference.

Val and Chernin [3.8][3.14] used the thermal load approach to determine the free increase of the reinforcing bar, which acted as corrosion expansion. The expansion of the steel reinforcing bar was considered a free increase in the radius ( $\delta$ ) caused by corrosion. It was estimated as follows:

$$\delta = \alpha_T \Delta T r \quad (3.2)$$

where  $\alpha_T$  is the coefficient of thermal expansion,  $\Delta T$  the increase in temperature, and  $r = \frac{\phi_b}{2}$  is the radius of the reinforcing bar.

Berra et al. [3.15] modelled the expansion of corrosion products via thermal strains imposed on the steel bar. Orthotropic thermal expansion properties were specified to obtain only radial expansion and no elongation of the bar.

The volume increase of the corrosion products around the bar that causes stresses and cracking of the concrete cover was modelled in a corrosion layer. If there is no restraint on the corrosion product from the surrounding concrete, all effective corrosion substances can expand freely without any confining stress. The free increase in bar radius ( $\delta$ ) can be expressed by:

$$\delta = \sqrt{r^2 + (\alpha - 1) \cdot (2rx - x^2)} - r \quad (3.3)$$

where  $r$  is the radius of the steel bar;  $x$  is the corrosion penetration, and  $\alpha$  is the volume of rust relative to uncorroded steel.  $\alpha$  is used as an input parameter by assuming that the

volume of the rust is  $\alpha$  times the volume of the steel that has corroded [3.16]. The value of  $\alpha$  is based on the type of corrosion products, as presented in Table 4.1. However, a value of 2 has been used by many researchers in their analyses [3.1] [3.17] [3.18].

### ***3.2.3 Penetration of corrosion products into concrete pores and cracks***

Several factors, such as the diffusion of corrosion products into the concrete and changes in the corrosion rate with time, control the agreement between numerical works and experimental data. Although the diffusion of corrosion products into concrete is a very important parameter affecting crack initiation and propagation, what fraction of corrosion products diffuses into concrete and what accumulates around a corroding bar creating pressure on the surrounding concrete have never been determined experimentally [3.10]. Out of the total amount of rust product, not all will contribute to the pressure build-up. Some of it may be carried away from the rust layer and deposited within the open crack [3.5]. To resolve this problem, researchers have introduced an empirical parameter (porous zone,  $\delta_o$ ) into an analytical model that would give better agreement between the model and the test results. Liu and Weyers [3.4] assumed this porous zone to be 12.5  $\mu\text{m}$  in their study. El Maaddawy and Soudki [3.19] used  $\delta_o$  ranging from 10 to 20  $\mu\text{m}$ . However, in many cases, the reported values of  $\delta_o$  have been obtained from the pure fitting of model predictions to experimental results [3.20]. Thus, it may not be considered a measurable input parameter but rather as a fitting parameter to adjust model predictions to experiments.

### ***3.2.4 Crack modelling***

Cracking in concrete can be modelled in two ways, by discrete crack and smeared crack models. The discrete cracking model was first developed by Ngo and Scordelis [3.21], who carried out a linear elastic analysis of beams with predefined crack patterns. The cracks were modelled by the separation of nodal points. Discrete cracking representation has received only limited acceptance because of the difficulty involved in providing for an economical redefinition of the structural topology following the formation of cracks. With the changing of the topology in these models as cracking progresses, the redefinition of the nodal points destroys the narrow band width in the structural stiffness matrix and

greatly increases the computational effort required for the solution. The computational effort can be reduced if a predefined crack is incorporated into the finite element model, but the accuracy of the result then depends on the accuracy with which the crack can be defined.

The smeared cracking model was introduced by Rashid [3.22]; it offers automatic generation of cracks without the redefinition of the finite element topology and complete generality in possible crack direction [3.23]. The smeared crack approach offers a number of advantages over the discrete approach. Re-meshing techniques and continuous topological redefinition are not necessary in the smeared process. Also, the rotation of principal stress axes can be treated during the strain softening. In the discrete approach this is not possible, since the crack should be inserted a priori and kept fixed during all the subsequent steps of the analysis [3.24].

### 3.2.5 Material properties

Pantazopoulou and Papoulia [3.5] and Bhargava et al. [3.6] used the idealised stress-strain relationship (Figure 3.2) for smeared cracked concrete in their studies. Before cracking, the relationship between the average principle hoop stress  $\sigma_\theta$  and average principle strain  $\varepsilon_\theta$  for concrete in tension is assumed to be linear elastic with the slope equal to  $E_c$ , i.e., the initial tangent modulus.

$$\sigma_\theta(r) = E_c \cdot \varepsilon_\theta(r) \quad (3.4)$$

Once  $\varepsilon_\theta$  exceeds the cracking tensile strain  $\varepsilon_{cr} = f_t / E_c$ , the cracking in concrete is modelled as a process of tension softening that starts at  $\varepsilon_{cr}$  and ends at  $\varepsilon_\theta = \varepsilon_u$ , where  $\varepsilon_u$  is the strain corresponding to the zero residual tensile strength of fracture energy ' $G_f$ ' of the concrete, which is defined as the energy required to propagate a tensile crack of unit area.  $f_t$  is taken as  $0.33f_c^{(1/2)}$ .  $G_f$  has been calculated as follows [3.25]:

$$G_f = G_{fo} (f_{cm}/f_{cmo})^{0.7} (N/mm) \quad (3.5)$$

where  $f_{cmo} = 10$  MPa and  $G_{fo}$  is interpolated depending on the maximum aggregate size.

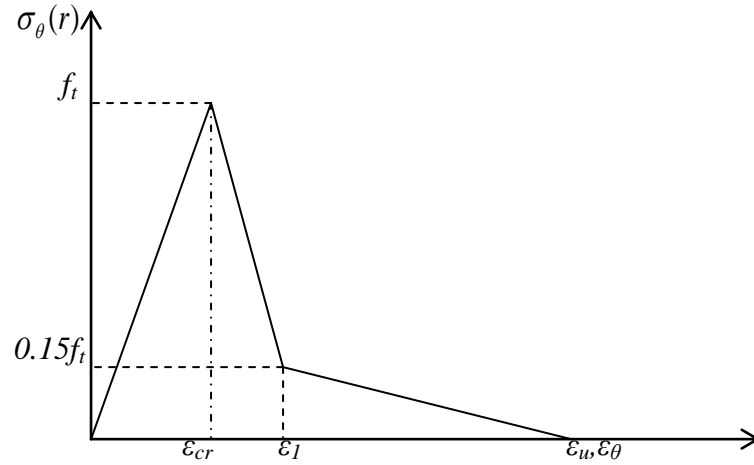


Figure 3.2: Idealised stress-strain diagram for cover concrete in uniaxial tension

Val et al. [3.10] modelled crack initiation based on the Rankine criterion, where the crack forms in the direction normal to the maximum principle stress when this stress exceeds the tensile strength of the concrete.

Ahmed et al. [3.9] modelled concrete based on the tension cut off, tension softening behaviour, shear retention behaviour, and yield condition. The nonlinear behaviour of concrete under tension was modelled by a quasi-brittle cracking model, in which the tensile stress in the concrete after cracking is given by a linear-softening relationship. The ultimate strain of the concrete is determined according to the following equation:

$$\varepsilon_u = \frac{2G_f}{f_t h} \quad (3.6)$$

where  $f_t$  is the tensile strength of concrete,  $G_f$  is the fracture energy of concrete, and  $h$  is the fracture zone width and equal to the square root of the element area.

### 3.2.6 Conclusions

Numerical studies of corrosion induced cracking have been discussed, ranging from analytical works to properties of materials. The conclusions of the discussion are as follows:

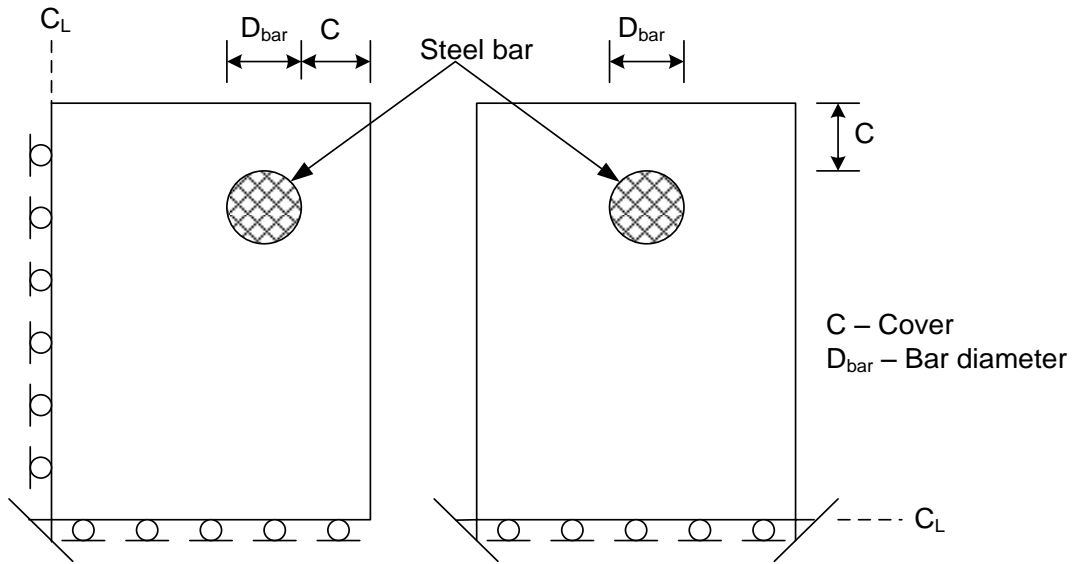
- a) Based on previous studies, it is clear that most models on corrosion-induced crack were treated as two-dimensional because of the adequacy of this model in representing uniform corrosion along the corroded length.

- b) A value of 2 for the rust volume fraction will be used in the current study, as it is frequently used by many researchers and because of the absence of data on actual rust properties from experimental studies.
- c) Free expansion of corrosion products will be modelled using a thermal expansion analogy. It provides uniform characteristics to represent rust behaviour.
- d) Since data on the amount of rust products penetrating into concrete pores and cracks are unavailable from experimental work, it is assumed that no corrosion products penetrate the concrete pores and cracks. Therefore, an analysis will be conducted to determine the amount of corrosion products required to fill up those areas by comparing it with the experimental data.

### **3.3 Numerical Model Procedure**

A numerical model is used to determine the influence of corrosion penetration on the formation and propagation of cracks visible on the surface of a RC member. This study concentrates on the estimation of the amount of corrosion products that produce pressure around the steel-concrete interface and initiate the crack and the subsequent growth of surface crack width.

In this analysis, corrosion is assumed to be uniform along the main bar; therefore, a two-dimensional finite element model of the section perpendicular to the bar axis is adopted to describe the initiation and propagation of concrete cracking. For a corner bar [Figure 3.3(a)], two continuous sides to the left and bottom were fixed in the X and Y directions, while for a centre bar [Figure 3.3(b)], half of the specimen was modelled.



a) Corner location bar      b) Centre location bar

Figure 3.3: Idealisation of specimens

### 3.3.1 Steel reinforcement and concrete material properties

A steel reinforcing bar is treated as linear elastic material. The modulus of elasticity and Poisson's ratio are taken as 210,000 MPa and 0.3, respectively, while the coefficient of thermal expansion is  $12 \times 10^{-6}/^{\circ}\text{C}$ .

In LUSAS's finite element model, concrete properties are divided into elastic and plastic properties. The elastic section requires the Poisson ratio to be taken as 0.2, and the modulus of elasticity is calculated using the CEB-FIB code [3.25]:

$$E_c = E_{co} \left[ \frac{f_{cm}}{f_{cmo}} \right]^{1/3} \quad (3.7)$$

where  $E_{co} - 2.15 \times 10^4$  MPa  
 $f_{cm}$  - Actual compressive strength of concrete at age 28 days  
 $f_{cmo} - 10$  MPa

The plastic section is based on a multi-crack model (model 94) that requires input of various parameters. The multi-crack model is a plastic-damage-contact model in which

damage planes form according to a principle stress criterion and develop as embedded rough contact planes [3.26]. The basic input for concrete properties is the uniaxial compressive strength ( $f_c$ ) (Figure 3.4). The value for the experimental uniaxial compressive strength of concrete is taken from a cube test of the concrete mix. It is worth mentioning that the compressive strength of concrete used to calculate the modulus of elasticity by Equation 3.7 is the cylinder compressive strength; the conversion is that the cylinder strength is 80% of the cube strength. The uniaxial tensile strength of concrete is calculated using Equation 3.8 from the CEB-FIB [3.25] code, where the mean axial tensile strength ( $f_{ctm}$ ) is estimated from the mean splitting tensile strength ( $f_{ct,sp}$ ):

$$f_{ctm} = 0.9 f_{ct,sp} \quad (3.8)$$

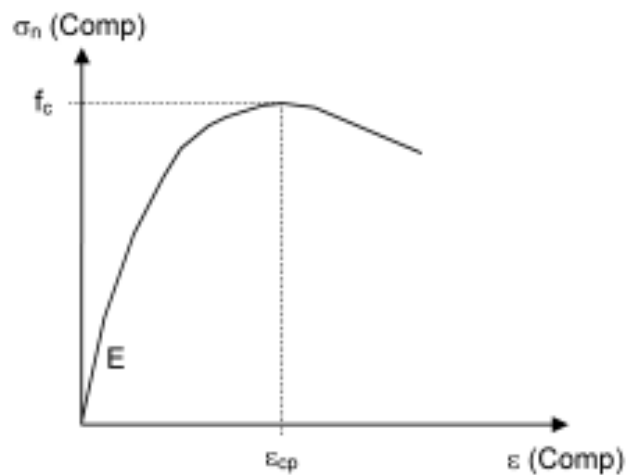


Figure 3.4: Nonlinear behaviour of concrete in compression

For the crack model, LUSAS provides two options; cracking can be modelled based on the strain at peak uniaxial compression or from the fracture energy per unit area. The first option can be used for reinforced concrete elements, while the second option produces a localised crack zone that leads to localised fracture. In the current study, the second option was adopted because of the localised crack in the fracture zone, and it gives an advantage to concrete meshing where coarse mesh can be used [3.27]. Other parameters are based on the default values set for this model. According to the CEB-FIB code, the fracture energy per unit area,  $G_f$ , is calculated using the following equation:

$$G_f = G_{fo} (f_{cm} / f_{cmo})^{0.7} \quad (3.5)$$

where  $f_{cmo} = 10$  MPa and  $f_{cm}$  is the mean value of compressive strength.

$G_{fo}$  is the base value of fracture energy. It depends on the maximum aggregates size  $d_{max}$ , as given in Table 3.2.

$d_{max}$	$G_{fo}$ (N/mm)
8	0.025
16	0.030
32	0.058

Table 3.2: Base values of fracture energy  $G_{fo}$  (N/mm)

### 3.3.2 Crack representation

In modelling the crack, a two-stage process has been adopted. First, a smeared crack approach is used to determine the crack location and direction because it offers an automatic generation of cracks without the redefinition of the finite element topology and complete generality in the possible crack direction. Second, after the crack location has been determined from the smeared crack analysis, discrete cracks are represented by delamination interface elements to analyse the crack width from its initiation to propagation. In this model, concrete elements are separated within a predefined crack path and the displacement of the interface elements is considered to represent the crack opening (Figure 3.5). If the stress exceeds the strength threshold value in the opening or shearing directions, the tensile strength of the interface element is reduced linearly as defined by the material parameters, and complete failure is assumed to occur when the fracture energy is exceeded. No initial crack is inserted, so the interface elements can be placed in the model at potential delamination areas, where they lie dormant until failure occurs [3.25].



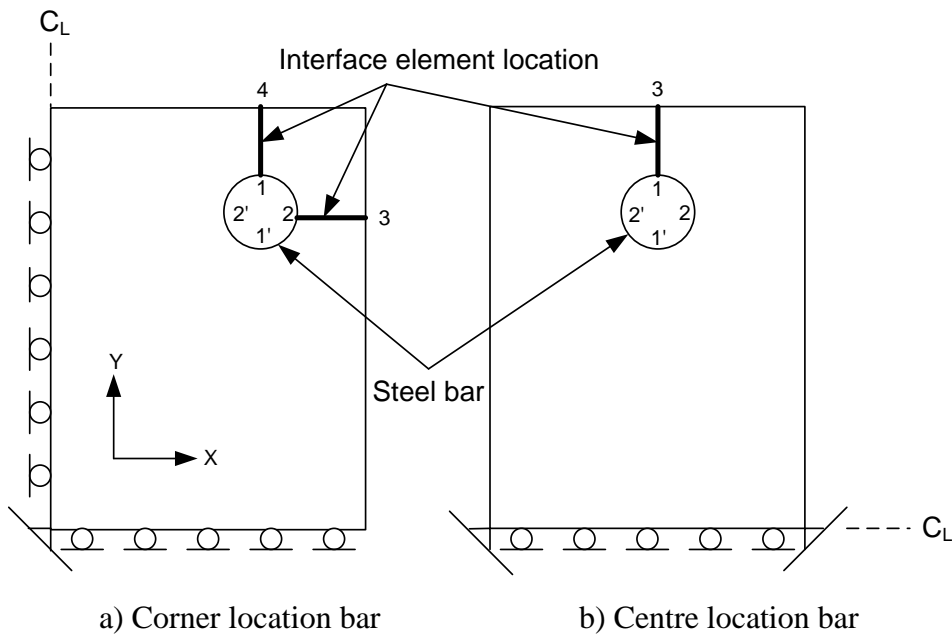


Figure 3.5: Location of interface elements

### 3.3.3 Interface properties

Two interface attributes will be used in the modelling. The first will represent the opening of the surface crack during the initiation and propagation process, while the second will be used to represent the bonding condition between the steel bar and the surrounding concrete.

#### 3.3.3.1 Crack interface

The properties are based on the fracture energy and initiation stress, as presented in Figure 3.6. A linear strain softening is assumed once the threshold strength has been reached, and the material does not resist any further straining once the total fracture energy has been exceeded [3.26]. The fracture energy has a specific value for each fracture mode depending on the material being used. Initiation stress is the stress at which delamination is initiated. Relative displacement is defined as the maximum relative displacement between element faces and is used to define the stiffness of the interface before failure [3.26].

Provided it is sufficiently small to simulate an initially very stiff interface it will have little effect. Open and shear fracture modes for delamination interface elements are used. These elements have no geometric properties and are assumed to have no thickness.

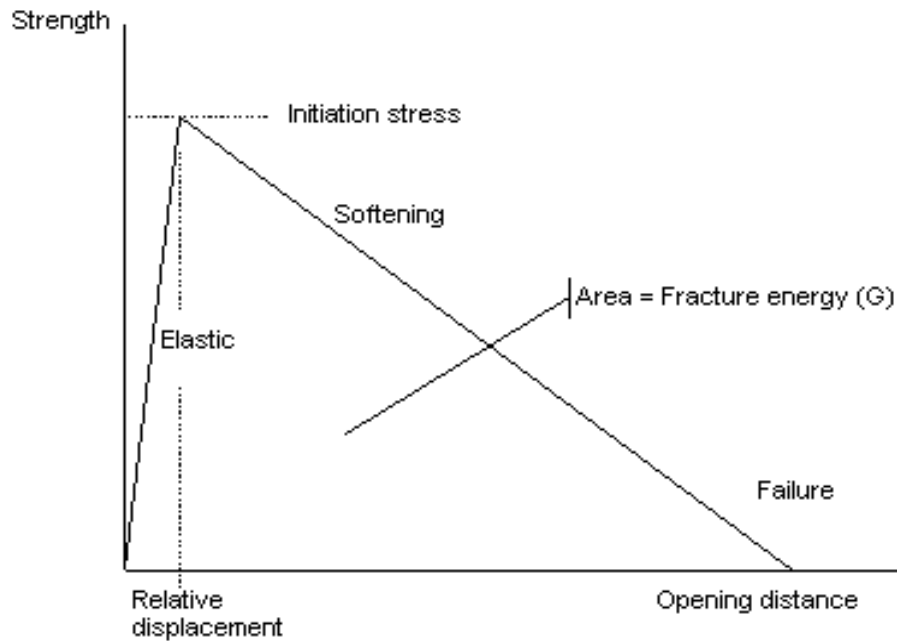


Figure 3.6: Delamination interface properties

Based on Figure 3.6, the input data for the interface properties are shown in Table 3.3.

Input data	Source
Initiation stress	Tensile strength, $f_{ctm}$ (MPa)
Fracture energy	Calculated from Equation 3.5
Maximum relative displacement	$1 \times 10^{-6}$ (default value)

Table 3.3: Input data for interface properties

Figure 3.7 shows an example of the non-linear behaviour of the interface element in tension. The crack is assumed to propagate when the stress at the crack tip reaches the maximum tensile strength ( $f_{t,max}$ ). Once the crack opens, the stress is not assumed to fall at once but to decrease linearly with increasing crack width.

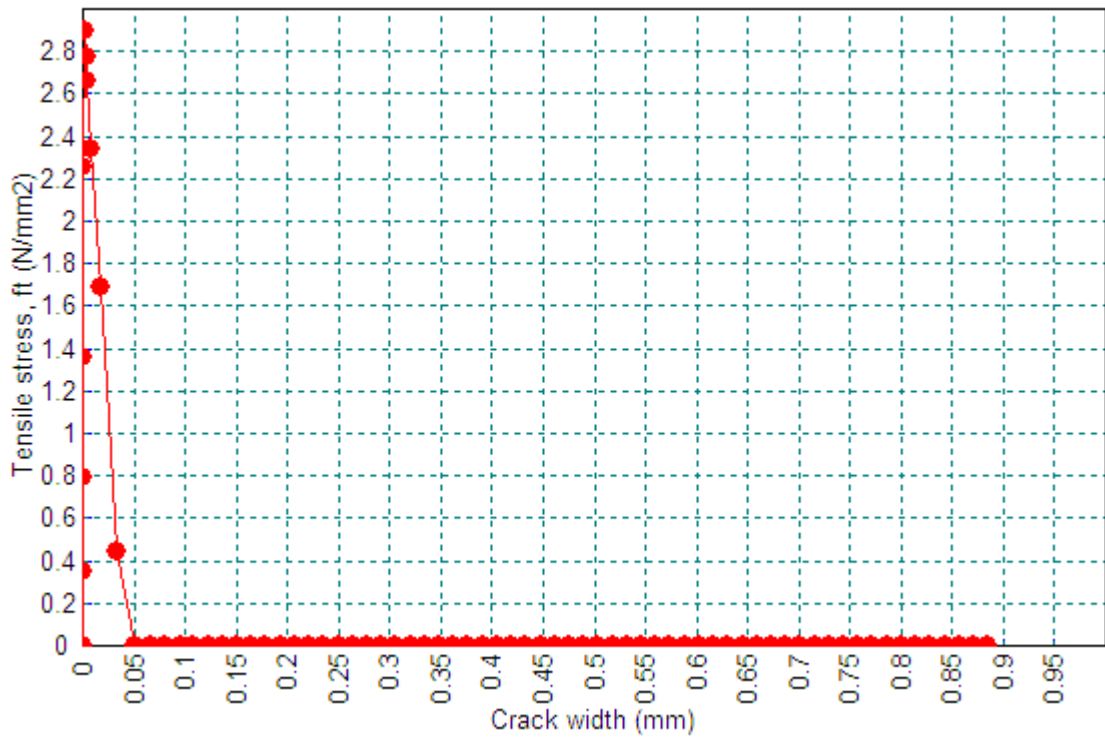


Figure 3.7: Tensile stress versus displacement (crack width)

### 3.3.3.2 Friction interface

The contact problem between the reinforcing bar and concrete surfaces is modelled using the ‘slideline’ attribute provided by LUSAS. This interface element controls the interaction between disconnected meshes of steel bars and concrete. ‘Slidelines’ allow the definition of properties such as the stiffness scale factor, friction coefficient, and pre-contact and are assigned to corresponding pairs or groups of features, known as ‘master’ and ‘slave’. By using this model, the friction coefficient between the surrounding concrete and steel reinforcing bars can be assigned and is taken to be 0.4 as proposed by Lundgren [3.16].

### 3.3.4 Loading condition

Modelling of the expansion of corrosion products by applying the thermal analogy was used previously by Val et al. [3.11] and Chernin and Val [3.14], as discussed in section 3.2.2. Therefore, as no corrosion loading facility is provided in the LUSAS modelling procedure, the same approach was applied in this work to study the propagation of

surface cracks resulting from the expansion of corrosion products. To this end, the temperature load was used in the analysis and the thermal strain of the reinforcement bar was obtained using the temperature rise and the coefficient of thermal expansion. For the plane strain element, the thermal strain is defined:

$$\varepsilon_t = (1 + \nu)\Delta T\alpha_T \quad (3.9)$$

where:

- $\varepsilon_t$  - Radial thermal strains
- $\nu$  - Poisson ratio
- $\Delta T$  - Temperature rise
- $\alpha_T$  - Coefficient of thermal expansion

The temperature rise  $\Delta T$  is then given by

$$\Delta T = T - T_{ref} \quad (3.10)$$

where  $T$  and  $T_{ref}$  are the current temperature and reference temperature, respectively.

The conversion from the radial thermal strain ( $\varepsilon_t$ ) to the radial thermal expansion of the bar radius ( $\Delta r$ ) is done as follows:

$$\Delta r = \varepsilon_t \cdot r \quad (3.11)$$

The conversion of the expansion of the bar radius to corrosion penetration is made as follows. According to Lundgren [3.16], at a free increase in the bar radius caused by corrosion,  $\Delta r$  can be estimated by using Equation 3.3.

If  $p_{corr} \ll r$ ,  $\Delta r$  can be estimated as follows:

$$\Delta r = (\alpha - 1)p_{corr} \quad (3.12)$$

Equation 3.12 is used to calculate the corrosion expansion analytically to be compared with experimental results.

### 3.3.5 Mesh configuration

Since modelling the crack initiation and propagation was based on the fracture energy, Hillerborg et al. [3.27] suggested that the analysis could be performed with a coarse mesh because there were no stress singularities and the amount of absorbed energy was not very sensitive to the mesh size. Therefore, eight-node quadrilateral mesh is used to describe the concrete, while six-node triangle mesh is used to describe the steel reinforcing bars (Figure 3.8).

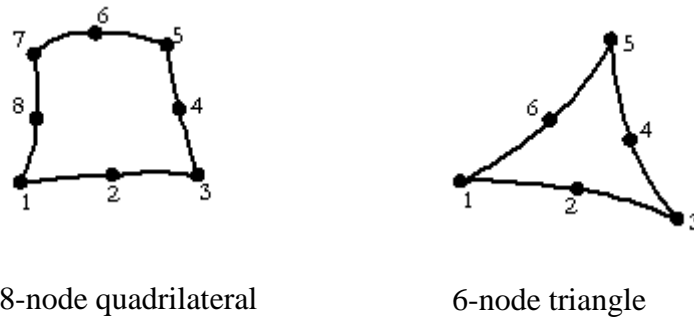


Figure 3.8: Mesh elements for concrete and steel reinforcement

For the interface element, a six-node quadratic element is used for modelling delamination and crack propagation, as presented in Figure 3.9.

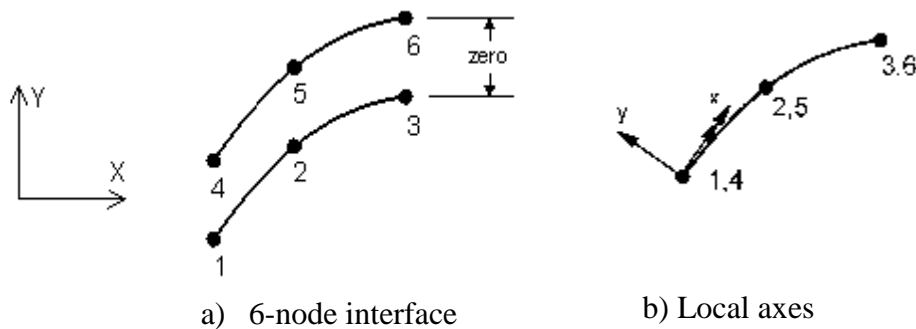


Figure 3.9: 2D interface elements

In the finite element analysis, the accuracy of the results is controlled by the selection of the mesh density, as a finer mesh produces more accurate results but requires more computer time for solving the problem. Regarding this point, a simple investigation has been conducted to determine the acceptable mesh division without compromising the accuracy of the results. In this investigation, a thermal load is applied to the steel bar. The

displacement of node 1 (stress concentration area) in Figure 3.10 was monitored against the horizontal mesh division of the crack zone. The vertical mesh was fixed to four elements per 10 mm. As shown in Figure 3.11, the mesh density was quantified by the number of elements per 23 mm. Constant displacement was obtained for the mesh density of four elements per 23 mm and the displacement dropped more than 20% for fewer elements. Therefore, the mesh density of four elements per 23 mm is selected in this numerical study.

For the interface elements, a similar approach has been used to study the variation of surface crack width with mesh density. The interface line is placed in a similar location as in Figure 3.10 that starts from the steel bar to the concrete surface. This interface line is divided into five, six, and eight divisions. The opening of the surface crack from these three divisions is plotted against the load factor. As shown in Figure 3.12, the opening of a surface crack is consistent when the line is divided into six and eight divisions. Therefore, six divisions are taken as the minimum division used in this study for the interface elements.

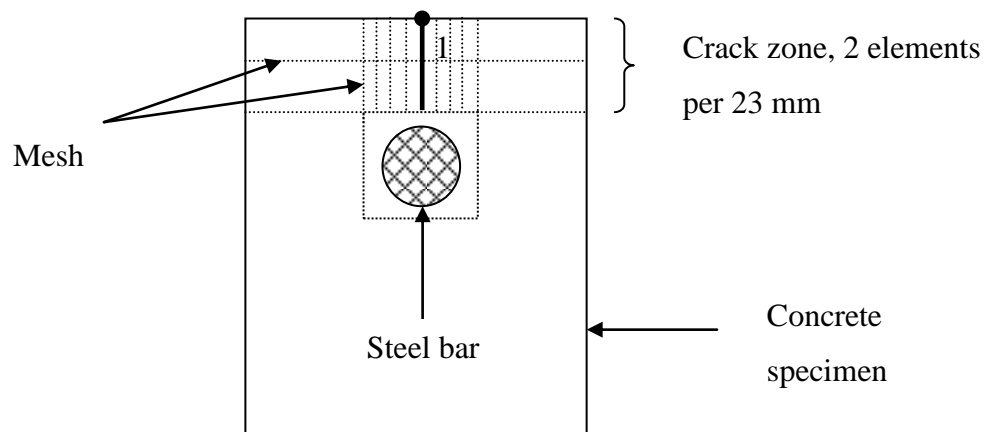


Figure 3.10: Specimen model to study mesh density

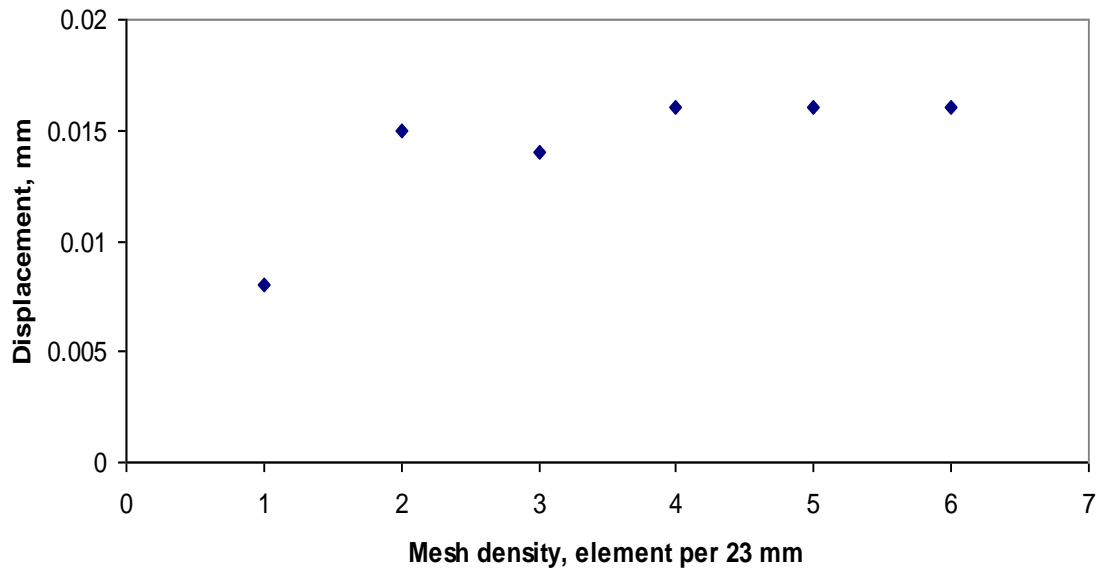


Figure 3.11: Effects of different mesh elements on displacement

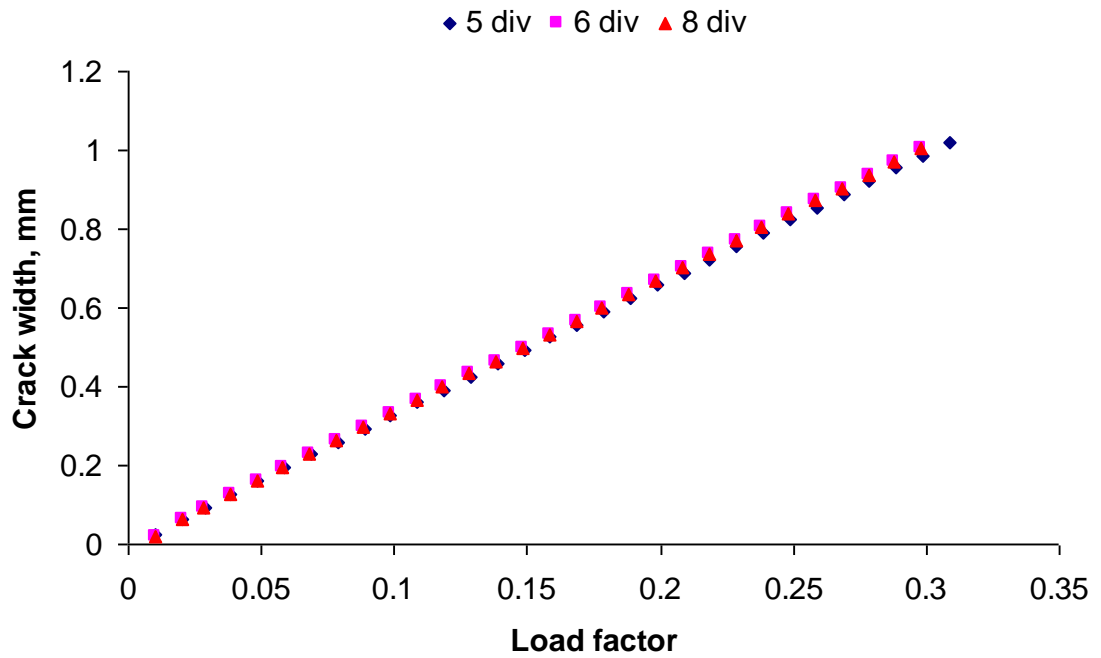


Figure 3.12: Crack width for different interface divisions

### 3.3.6 Nonlinear analysis procedure

Because of the nonlinearity of concrete due to the presence of cracks, the problem is analysed using a nonlinear approach provided by LUSAS. A temperature increase is set to produce a thermal load that is imposed on the steel bar. This load induces an expansion force in the surrounding concrete. The load factor that controls the expansion is increased by pre-defined steps. The convergence of the analysis is set up by the user input to produce the desired accuracy for the analysis. In LUSAS, the nonlinear solution is based on the Newton-Raphson procedure [3.26]. An initial prediction of the incremental solution is based on the tangent stiffness from which incremental displacements and their iterative corrections may be derived (Figure 3.13). The details of the solution procedure are controlled using the nonlinear control properties assigned to the load case. A solution procedure is usually adopted, in which the total required load is applied in a number of increments. Within each increment, a linear prediction of the nonlinear response is made, and subsequent iterative corrections are performed to restore equilibrium by the elimination of the residual or out-of-balance forces.

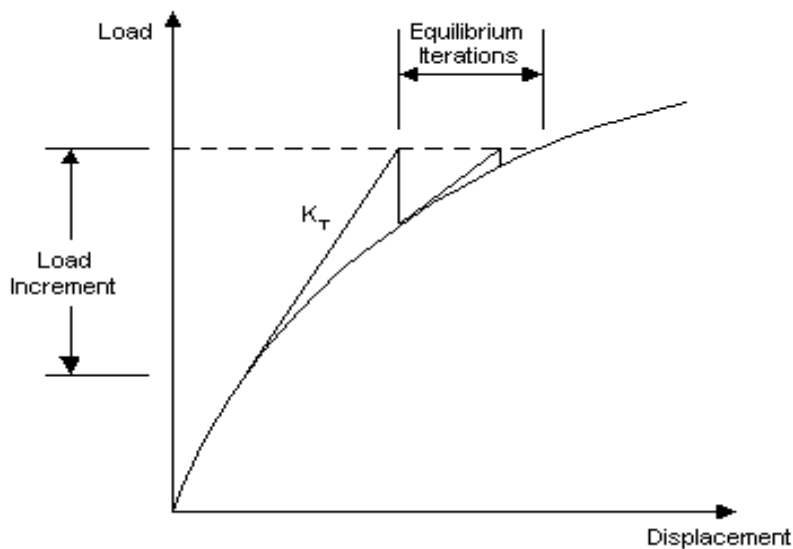


Figure 3.13: Increment-iterative method

Convergence criteria are required to define when equilibrium has been achieved. The selection of appropriate convergence criteria is an important issue to obtain good results. A slack tolerance may provide incorrect answers, and if the tolerance is too restricted, it leads to unnecessary iterations and a waste of computer time. In this analysis, the load is specified by an automatic increment, and the starting and maximum load factors are



adjusted based on convergence. Furthermore, the maximum number of iterations may be specified. LUSAS provides a step reduction that reduces the load increment if convergence is difficult to achieve, and the default value is set to 0.5. It has been determined what the maximum number of reductions could be before the analysis fails to converge.

### 3.4 Presentation of Numerical Results

#### 3.4.1 Expansion of bar radius

The expansion of the bar radius because of the thermal load is used in this analysis to represent the expansion of corrosive products responsible for inducing surface cracks. The relationship between thermal strain from thermal expansion and corrosion penetration is given as follows:

$$\Delta r = \varepsilon_t \cdot r = (\alpha_v - 1)x \quad (3.13)$$

where  $\Delta r$  is the radius thermal expansion,  $\varepsilon_t$  is the thermal strain,  $r$  is the steel bar radius,  $\alpha_v$  is the volumetric expansion ratio of corrosion products ( $\alpha_v = 2$ ) and  $x$  is the corrosion penetration.

In modelling the thermal expansion of the bar radius in the LUSAS analysis, a temperature load is imposed on the steel bar and the increment of bar expansion is controlled by the load factor defined in the loading sequence. Based on the LUSAS manual version 14, the relationship between thermal expansion and the imposed temperature is given as in Equation 3.14 and shown in Figure 3.14.

$$\Delta r = (1 + \nu)(\Delta_T)r\alpha_T p \quad (3.14)$$

Where  $\Delta r$  is the free increase in bar radius,  $\nu$  is the Poisson ratio,  $\Delta_T$  is the temperature rise,  $r$  is the bar radius,  $\alpha_T$  is the coefficient of thermal expansion, and  $p$  is the load factor (increment of the load during the analysis).

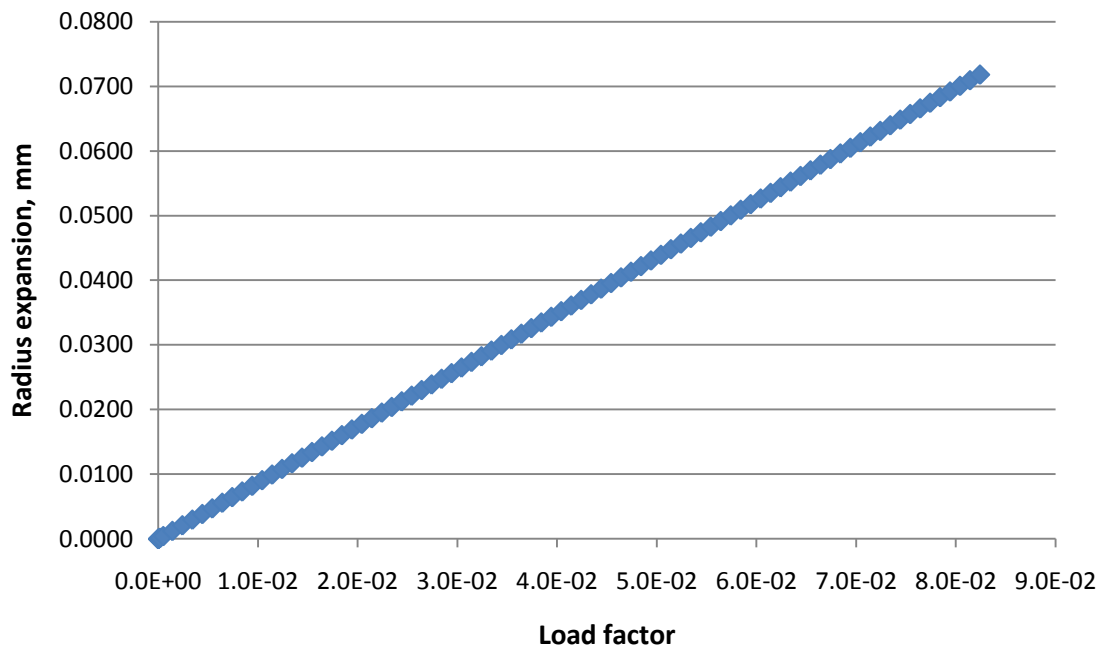


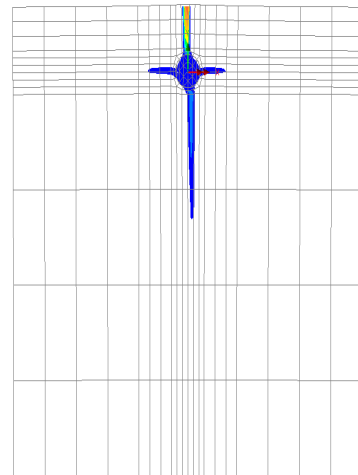
Figure 3.14: Radius expansion versus load factor

### 3.4.2 Crack location

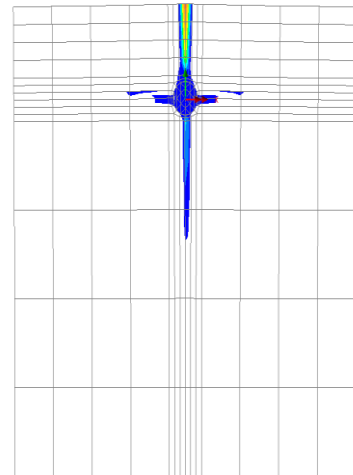
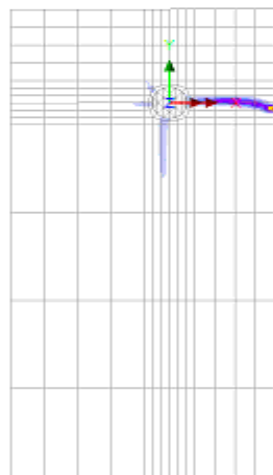
Non-linear analyses were conducted on the concrete specimens to determine the location of crack initiation and propagation. As the software does not provide an explicit model for corrosion, corrosion was represented by the thermal expansion of bars in the radial direction. No longitudinal deformations of reinforcement were imposed. During the analysis, thermal expansion of the reinforcing bar induces radial pressure on the surrounding concrete. When the strain of the concrete reaches the ultimate value, a surface crack forms. With further pressure imposed, the surface crack propagates to a certain extent. As these analyses were intended to determine crack location, only a qualitative interpretation is made in this phase. The location of cracks is represented by the blue contour plot as shown in Figures 3.15 and 3.16 for various bar diameters and locations. The blue colour plots indicate where the tensile strain in the concrete exceeds the strain capacity, while other colours in the plot express the extent of cracks, which corresponds to the increment of tensile strain.

The thermal expansion of steel reinforcement induced a single surface crack for both covers on 10 mm diameter bars. For 16 mm diameter bars, this trend is observed on the 16 mm concrete cover only. However, for the 16 mm bar with higher cover thickness, the

numerical analysis gave two crack locations. At the centre bar location, the formation of a crack occurs vertically from the bar to the top face. Analyses in the next section use a discrete representation of cracking at locations determined from these analyses.

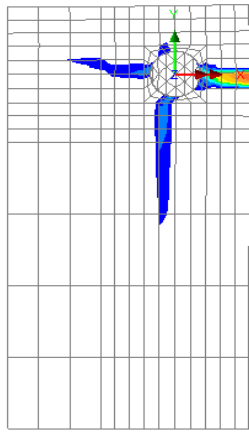


a) Corner location, 16 mm cover      b) Centre location, 16 mm cover

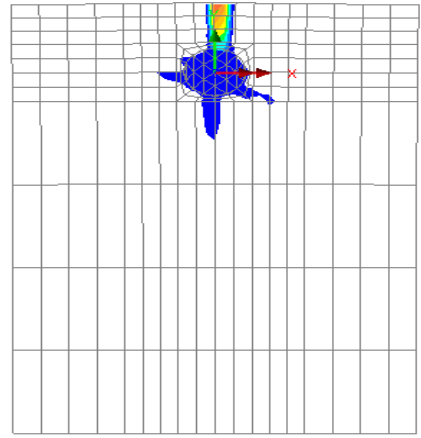


c) Corner location, 25 mm cover      d) Centre location, 25 mm cover

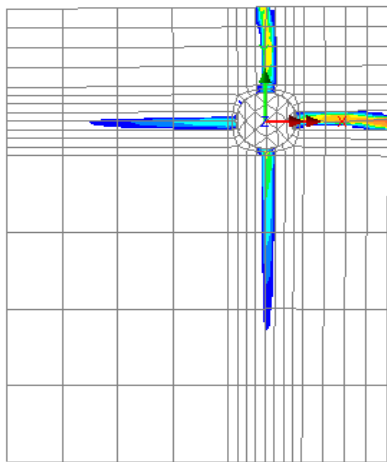
Figure 3.15: Crack location for 10 mm diameter main reinforcing bars



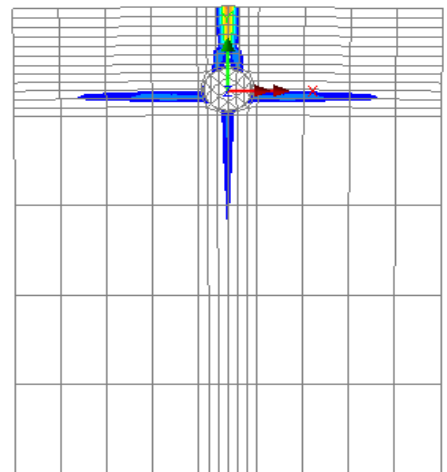
a) Corner location, 16 mm cover



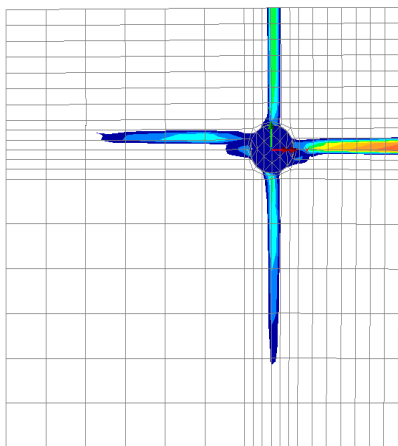
b) Centre location, 16 mm cover



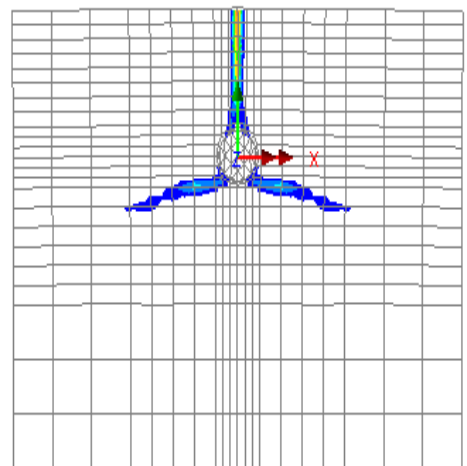
c) Corner location, 25 mm cover



d) Centre location, 25 mm cover



e) Corner location, 40 mm cover



f) Centre location, 40 mm cover

Figure 3.16: Crack location for 16 mm diameter main reinforcing bars

## 3.5 Results and Discussion

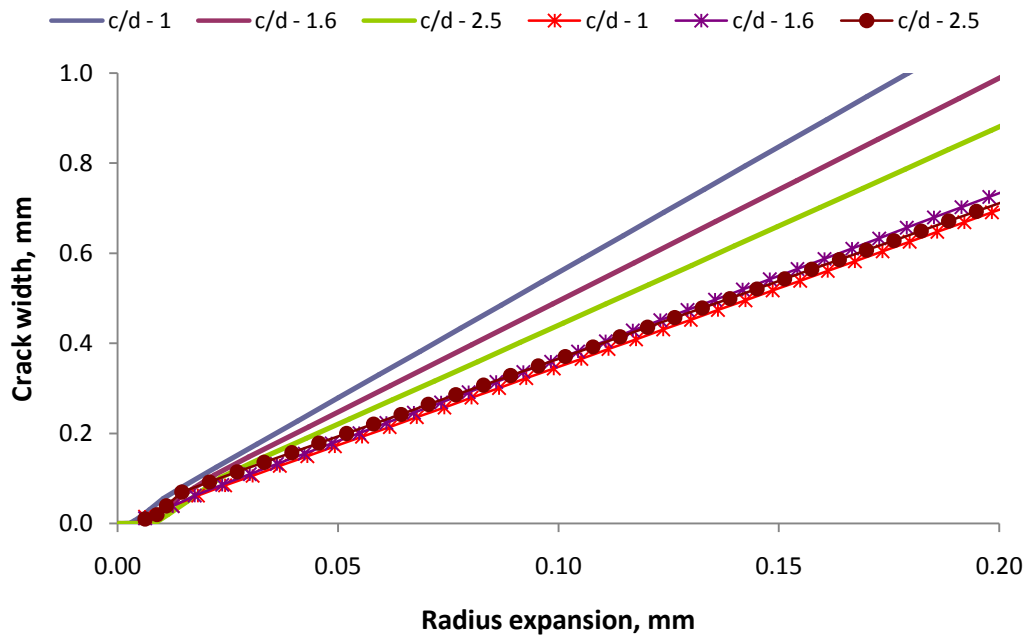
### 3.5.1 Crack Propagation

In the smeared crack model analysis, the location of the cracks is based on the tension softening of the concrete materials where the crack initiated when the tensile stress exceeds the ultimate tensile stress of the concrete. Thus, the smeared crack model is adopted to study the actual crack location caused by the expansion of the steel reinforcement. However, this model provides the location of the crack but not the width of the crack during the initiation and propagation phases. Therefore, another approach, discrete crack analysis, is used to obtain the actual crack width for the aforementioned phases. In modelling the propagation of surface cracks, the interface elements were placed at the crack location determined from the smeared crack analysis, and the analysis was conducted to determine the actual propagation of the surface cracks. The opening of these interface elements caused by the expansion of bar radius is considered as propagation of surface cracks. The nonlinear properties of concrete are used as an input in the properties of the interface elements. Therefore, the tension behaviour of the interface elements is similar to that of concrete.

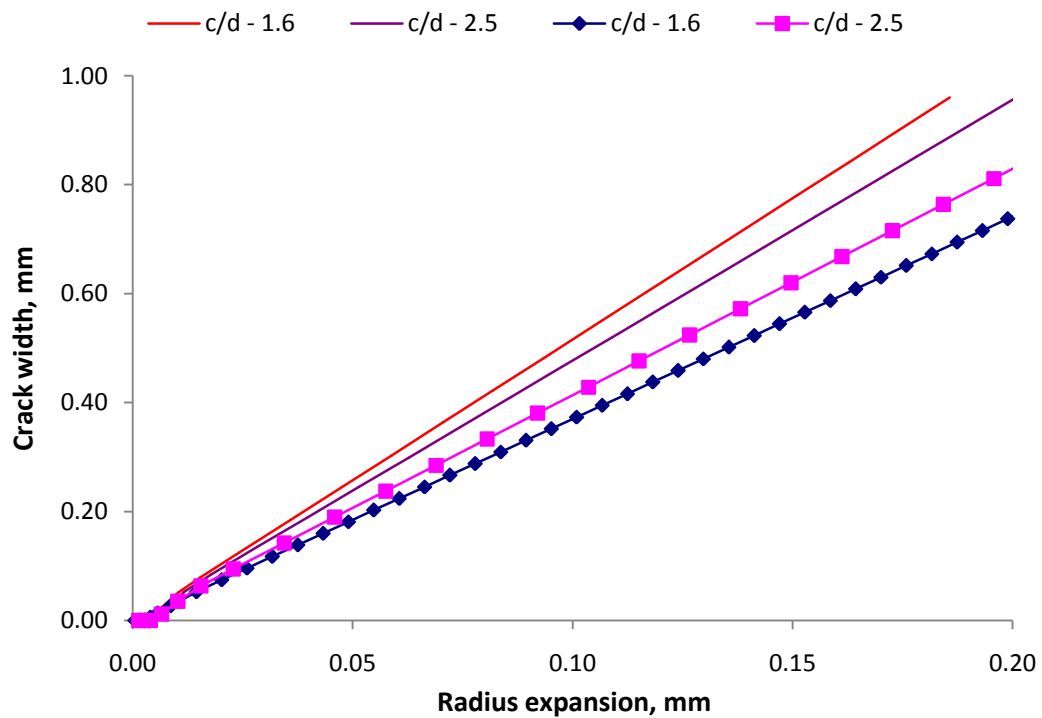
Based on previous studies, few models have been used to model the propagation of surface cracks caused by corrosion. In Bazant's model [3.3] (model 1), all the accumulated rust products were responsible for producing expansive pressure during the cracking process. In Liu and Weyers model [3.4] (model 2), the rust products were assumed to be initially deposited into the porous zone layer, and once this zone was 'filled', the accumulated rust built up the pressure to start the cracks. Both models are used in the current study to identify the influence of the porous zone on crack propagation. Since numerous porous layer thicknesses have been used previously, as discussed in section 3.2.3, a thickness of 0.01mm is used for the model 2 analysis.

The propagation of surface crack width versus the increasing bar radius caused by thermal expansion is presented in Figure 3.17 and 3.18 for model 1 and model 2, respectively. The results were plotted for different cover to diameter ratios, where the solid lines represent the corner bar location while lines with a marker indicate the centre bar location. Both the corner and centre bar locations show a similar linear relationship

between crack width and bar thermal expansion. Based on crack width, it can be seen that, for a similar radius expansion, higher crack width is observed at the corner bar location than the centre face bar and that the 16 mm bar diameter is higher than the 10 mm bar diameter. This trend is consistent for both models.

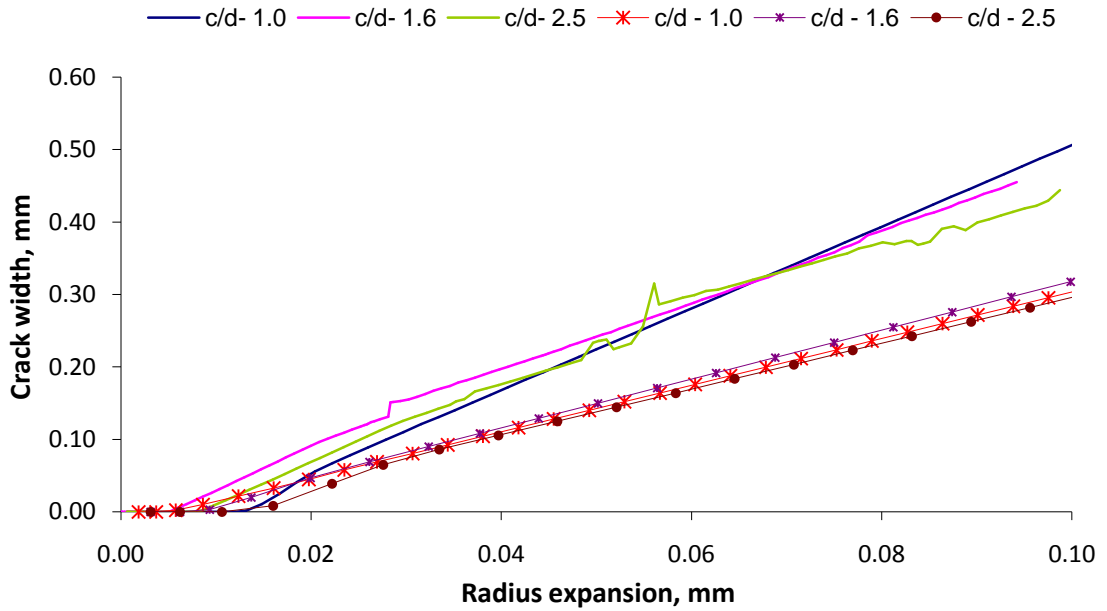


a) 16 mm bar diameter

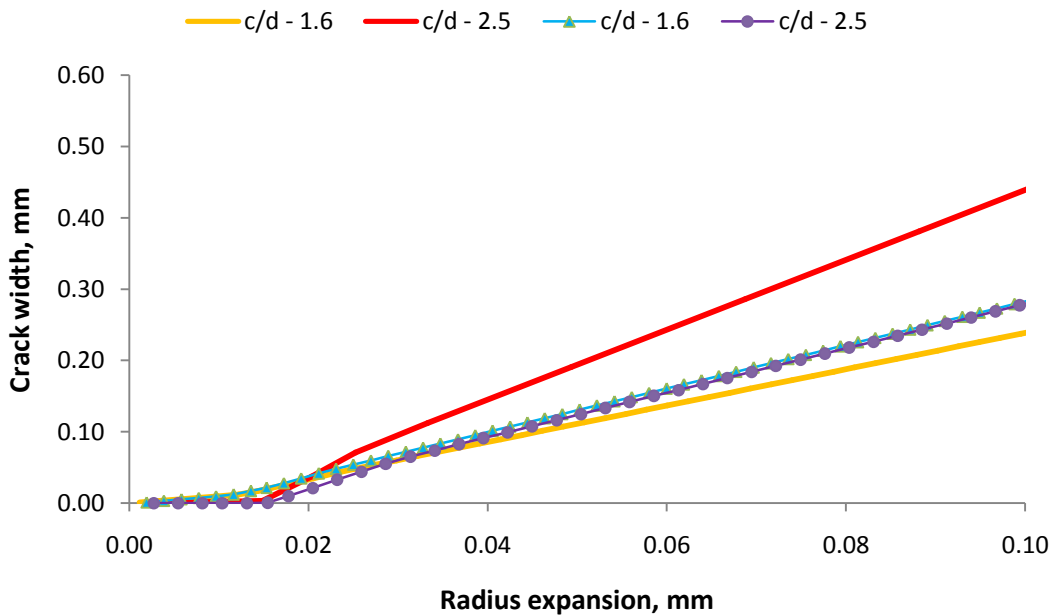


b) 10 mm bar diameter

Figure 3.17: Crack width propagation for different  $c/\phi_b$  ratios for 16 mm and 10 mm diameter bars (model 1)



a) 16 mm diameter bar

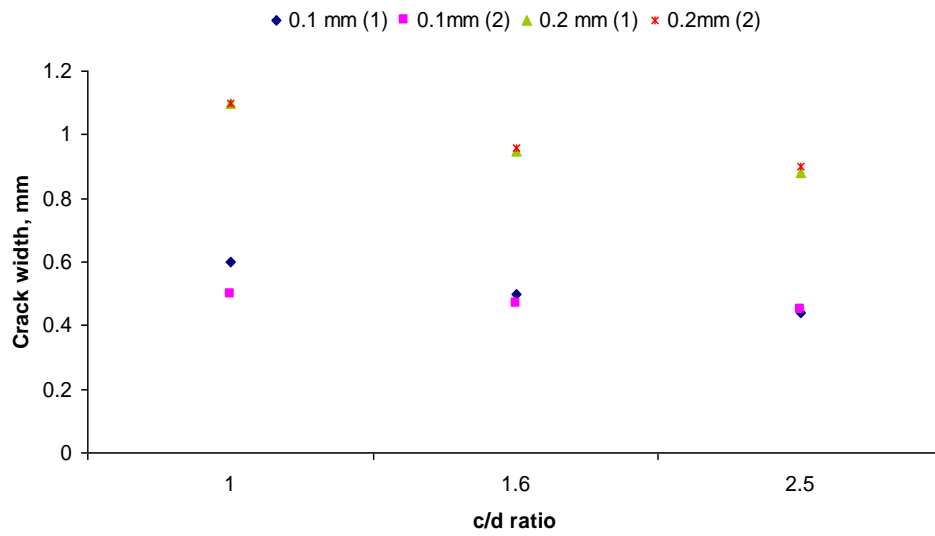


b) 10 mm diameter bar

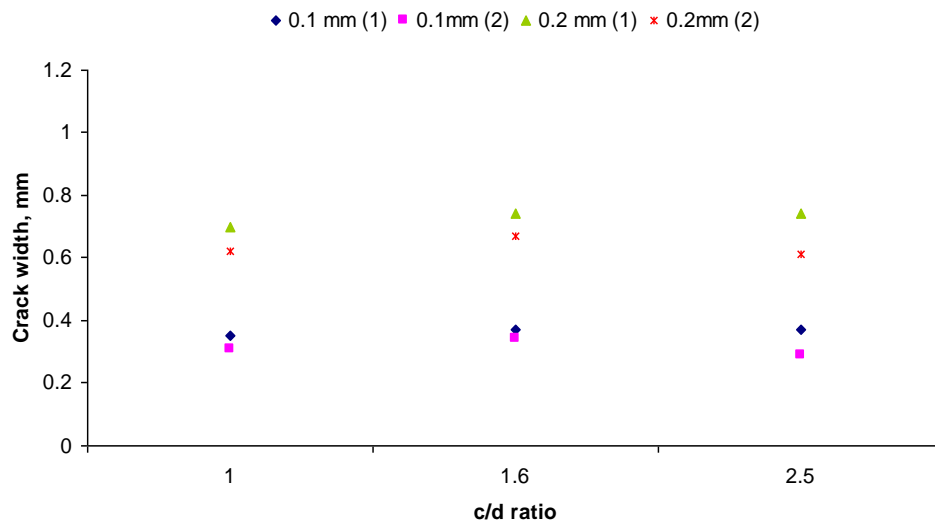
Figure 3.18: The influence of the porous zone on crack propagation (model 2)

To determine the difference between these two models on surface crack propagation, the results plotted in Figure 3.17 and 3.18 were extracted for bar radius increments (which is equivalent to corrosion penetration) of 0.1 mm and 0.2 mm and plotted against the cover to diameter ratio as shown in Figures 3.19 (a) and (b). As indicated, both models show a

similar trend, and a comparison of Figure 3.17 and 3.18 shows that the presence of a porous zone on model 2 did not significantly change the trend and width of the crack during propagation.



a) Corner bar location



b) Centre bar location

Figure 3.19: Variation of surface crack widths for different  $c/\phi_b$  ratios with 0.1 mm and 0.2 mm radius expansion



### **3.6 Summary of Numerical Results**

The first section showed the locations of surface cracks using a nonlinear concrete analysis. The location of surface cracks is determined based on the strain softening of concrete element caused by the strains imposed by thermal expansion of the bar radius. Following this, interface elements were placed at the same location and an analysis was conducted to determine the actual width of the surface cracks.

The numerical model demonstrated that, for a given amount of corrosion, as measured by both section loss and corrosion penetration, there would be a significant difference in crack width over 10 mm and 16 mm diameter bars. The presence of a porous layer around the concrete-steel interface produced insignificant effects on crack width propagation.

### **3.7 Corrosion Crack Analysis on Multiple Reinforcements**

The locations of corrosion cracks for a single bar were verified numerically in the previous section for various locations and cover thicknesses. This section discusses the influence of multiple reinforcing bar corrosion on the crack width pattern using a finite element modelling approach. The arrangement of the bar is based on the combination of corner-to-corner and corner-to-centre bar locations that are normally found in an actual beam. The displacement of the reinforcing steel bar diameter caused by the thermal expansion is used as the corrosion penetration for the corresponding crack pattern. Furthermore, the evolution of the crack pattern and the corresponding corrosion penetration is discussed.

#### ***3.7.1 Model selection***

The modelling and analysis in this section involve the selection of a concrete cross-section (Figure 3.20) with two different bar locations, a) double corner and b) combined corner and centre, with the former reinforced with 16 mm diameter bars, while the latter is reinforced with 16 mm and 10 mm diameter bars. The crack model is analysed based on the smeared crack model and the initiation, and propagation is controlled by the fracture energy. A summary of the specimens is presented in Table 3.4.

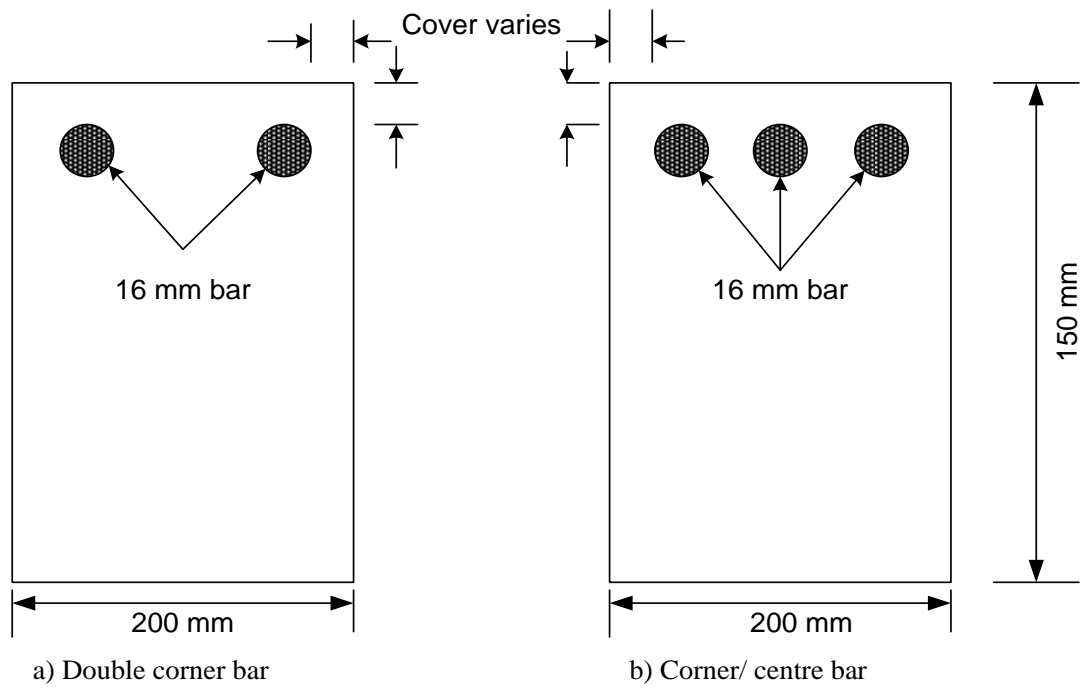


Figure 3.20: Model specimens

Specimen	$\phi_b$ (mm)	Cover, $c$ (mm)	$\frac{c}{\phi_b}$	Materials properties	
(a)	16	16	1.0	Concrete: $f'_c = 32.8$ MPa $f_t = 3.03$ MPa $G_f = 0.069$ N/mm	
		25	1.6		
		40	2.5		
(b)	16	16	1.0		Steel: $E = 200 \times 10^3$ MPa $\alpha_t = 12 \times 10^{-6}$
		25	1.6		
		40	2.5		

Table 3.4: Materials properties

### 3.7.2 Corner bar location

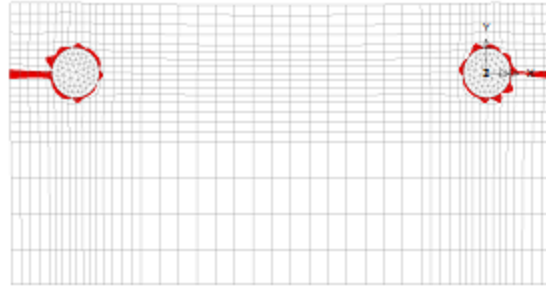
The crack pattern for a 16 mm diameter reinforcing bar for a double corner bar location is depicted in Figure 3.21 for a different concrete cover thickness with a minimum cover of 16 mm. The dimension of the concrete section used in this study is 200 mm wide and 150 mm deep, and the thermal load is applied to both reinforcing bars. Based on Figure 3.21, the thickness of the concrete cover influenced the pattern of crack propagation such that a side crack was observed for the smaller cover, while the thick cover tended to have cracks on both adjacent sides. The numerical radius expansions for these patterns are 3  $\mu$ m, 5

$\mu\text{m}$ , and  $10 \mu\text{m}$  for a 16 mm, 25 mm, and 40 mm cover, respectively. The trend shows that higher expansion is required to propagate cracks on a thicker concrete cover. It is quite common for a corner bar location to start a crack on a side location then the top, as this pattern was observed in the experimental work in Andrade et al. [3.28], when a crack was initiated on a side location even though it was 1.5 times thicker than on the top side.

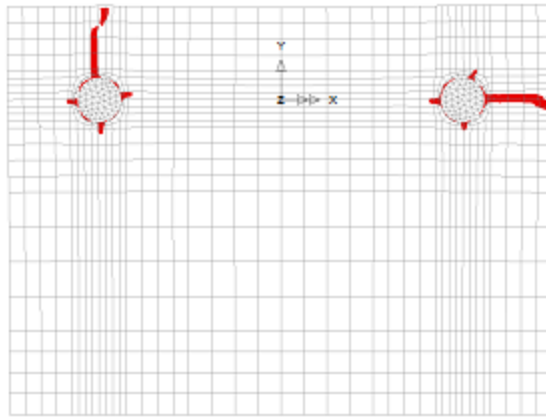
### ***3.7.3 Combined centre and corner bar location***

The other possible arrangement of the bars is shown in Figure 3.22, depicting a combination of corner and centre bar locations. The concrete cover varies between 16 mm and 40 mm. It shows that the crack pattern is not influenced by the thickness of the concrete cover but depends on the distance between bars. As with the 16 mm cover, the distance between bars is 3.75 times the cover, so the cracks propagate toward its cover. When the distance between bars is two times its cover, the pattern of the crack tends to propagate in the horizontal direction as shown in Figure 3.22(b). For the last case, where the spacing between bars is the same as the concrete cover, the crack is propagated towards the adjacent bar and the top side cover.

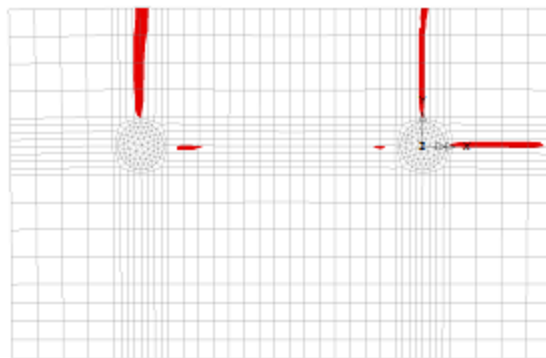
The expansions of the bar radius used to produce these cracks differ between the concrete cover such that the lowest expansion of  $7.5 \mu\text{m}$  is observed on the 40 mm cover, while  $12.7 \mu\text{m}$  and  $8.2 \mu\text{m}$  are observed for the 16 mm and 25 mm cover, respectively.



a) 16 mm cover

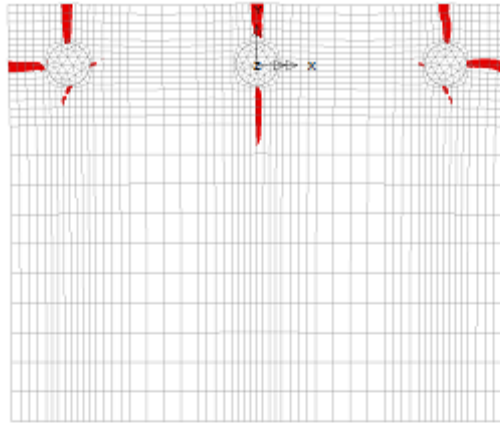


b) 25 mm cover

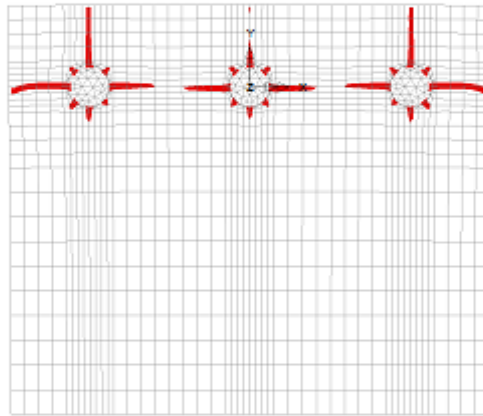


c) 40 mm cover

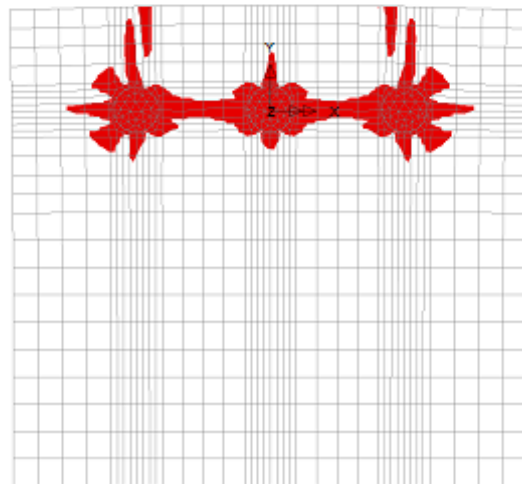
Figure 3.21: Crack pattern for different concrete cover thicknesses



a) 16 mm cover



b) 25 mm cover



c) 40 mm cover

Figure 3.22: Crack pattern for combined corner-centre bar location

### 3.7.4 Model validation

To account for the validity of the crack pattern in these specimens, a similar modelling procedure is adopted for experimental specimens based on Cabrera's [3.29] study on the corrosion of multiple reinforcing bars. Two selected specimens reinforced with 16 mm and 20 mm bars have a similar cross section, as shown in Figure 3.23.

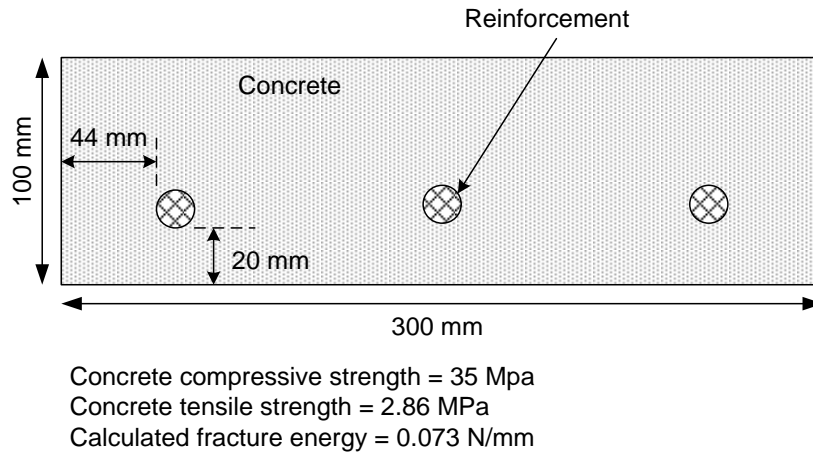
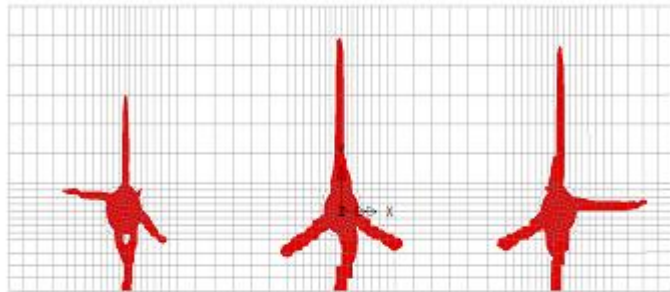
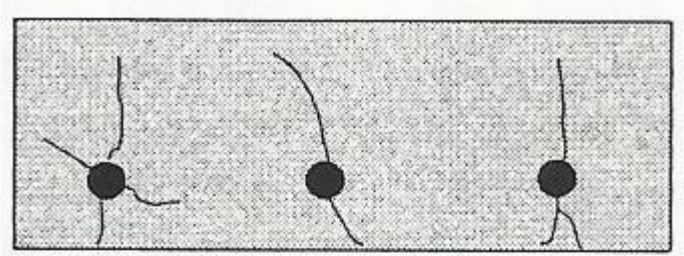


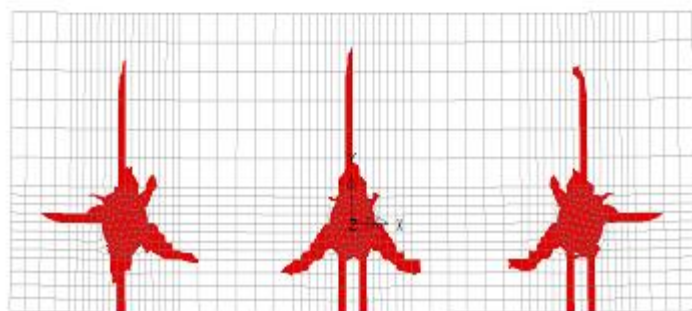
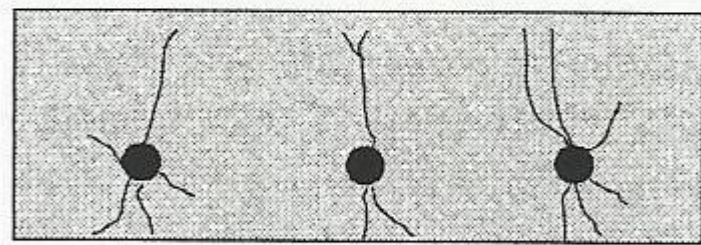
Figure 3.23: Cabrera's [3.29] specimen with multiple reinforcements

The comparison of experimental and numerical crack patterns is shown in Figure 3.24. The friction coefficient of 0.4, as discussed in section 3.3.3.2, is applied between the reinforcing bar and the concrete. Based on these figures, the crack pattern from the model shows similarities with the experimental crack location in that it has moved vertically. The experimental corrosion penetrations that produced these patterns were 0.53 mm and 0.34 mm for 16 mm and 20 mm diameter bars, respectively. Based on the discrete crack model, these penetrations produced 1.0 mm and 1.6 mm crack widths, which are 50% and 71% higher than the experimental crack width.

This result shows that finite element modelling approaches can be used to determine the location of surface cracks for single and multiple bar locations. Therefore, it can be concluded that the experimental crack location in this study is expected to be similar to those observed previously. Furthermore, as this numerical work has shown the propagation of surface crack width is controlled by several parameters such as the bar diameter, the thickness of the concrete cover, and the location of the bar (corner or centre), these parameters should be considered in the experimental work to understand clearly the influence of corrosion cracks on residual bond strength.



a) 16 mm diameter bar



b) 20 mm diameter bar

Figure 3.24: Crack patterns for different bar diameters

### 3.8 References

- [3.1] F.J. Molina, C. Alonso and C. Andrade, *Cover cracking as a function of rebar corrosion: Part 2 – Numerical model*, *Materials and Structures*, **26**, 532-548 (1993)
- [3.2] Y.G. Du, A.H.C. Chan, and L.A. Clark, *Finite element analysis of the effects of radial expansion of corroded reinforcement*, *Computers and Structures*, **84**, 917-929 (2006)
- [3.3] Z. P. Bazant, *Physical model for steel corrosion in concrete sea structures – Application*, *Journal of Structural Division*, **105**, 1155-1166 (1979)
- [3.4] Y. Liu and R.E. Weyers, *Modelling the time to corrosion cracking in chloride contaminated reinforced concrete structures*, *ACI Materials Journal*, **95**, 6, 675-681(1998)
- [3.5] S.J. Pantazopoulou and K.D. Papoulia, *Modelling cover-cracking due to reinforcement corrosion in RC structures*, *Journal of Engineering Mechanics*, **127**, 4, 342-351 (2001)
- [3.6] K. Bhargava, A.K. Ghosh, Y. Mori and S. Ramanujam, *Model for cover cracking due to rebar corrosion in RC structures*, *Engineering Structures*, **28**, 1093-1109 (2006)
- [3.7] S.B. Allampallewar and A. Srividya, *Modelling cover cracking due to rebar corrosion in RC structures*, *Structural Engineering and Mechanics*, **30**, 6, 713-732 (2008)
- [3.8] L. Chernin and D.V. Val, *Prediction of cover cracking in reinforced concrete structures due to corrosion*, *Proceeding 1<sup>st</sup> International Conference on Construction Heritage in Coastal and Marine Environment (ME-DACS08)*, Lisbon, Portugal (2008)
- [3.9] S.F.U. Ahmed, M. Maalej and H. Mihashi, *Cover cracking of reinforced concrete beams due to corrosion of steel*, *ACI Materials Journal*, **104**, 2, 153-161 (2007)
- [3.10] Y.G. Du, A.H.C. Chan, S. Williamson, and L.A. Clark, *FEM analysis of concrete cracking due to steel corrosion*, *Proceeding of the EURO-C 1998 Conference on Computational Modelling of Concrete Structures*, Badgastein, Austria, 481-489 (1998)



- [3.11] D.V. Val, L. Chernin and M.G. Stewart, *Experimental and numerical investigation of corrosion-induced cover cracking in reinforced concrete structures*, Journal of Structural Engineering, **135**, 4, 376-385 (2009)
- [3.12] P. Thoft-Christensen, H. L. Frandsen, and S. Svensson, *Numerical study of corrosion crack opening*, Structure and Infrastructure Engineering, **4**, 5, 381-391 (2008)
- [3.13] P. Thof-Christensen, S. Svensson and H.L. Frandsen, *3D-modelling of corrosion crack opening*, Advances in Reliability and Optimization of Structural Systems – Sorenson &Frangopol, Taylor & Francis Group, London (2006)
- [3.14] L. Chernin and D.V. Val, *Prediction of corrosion-induced cover cracking in reinforced concrete structures*, Construction and Building Materials, **25**, 4, 1854-1869 (2011)
- [3.15] M. Berra, A. Castellani, D. Coronelli, S. Zanni and G. Zhang, *Steel-concrete bond deterioration due to corrosion: Finite-element analysis for different confinement levels*, Magazine of Concrete Research, **55**, 3, 237-247 (2003)
- [3.16] K. Lundgren, *Modelling the effect of corrosion on bond in reinforced concrete*, Magazine of Concrete Research, **54**, 5, 165-173 (2002)
- [3.17] K. Toongoenthong and K. Maekawa, *Simulation of coupled corrosive product formation, migration into crack and propagation in reinforced concrete sections*, Journal of Advanced Concrete Technology, **3**, 2, 253-265 (2005)
- [3.18] D. Coronelli, and P. Gambarova, *Structural assessment of corroded reinforced concrete beams: modeling guideline*, Journal of Structural Engineering, **130**, 8, 1214-1224 (2004)
- [3.19] T. El Maaddawy and K. Soudki, *A model for prediction of time from corrosion initiation to corrosion cracking*, Cement and Concrete Composite, **29**, 168-175 (2007)
- [3.20] A. Jamali, U. Angst, B. Adey and B. Elsener, *Modelling of corrosion-induced concrete cover cracking: A critical analysis*, Construction and Building Materials, **42**, 225-237 (2013)
- [3.21] D. Ngo and A.C. Scordelis, *Finite element analysis of reinforced concrete beams*, ACI Journal, Proceedings, **64**, 3, 152-163 (1967)

- [3.22] Y.R. Rashid, *Ultimate strength analysis of prestressed concrete pressure vessels*, Nuclear Engineering and Design, **7**, 334-344 (1968)
- [3.23] H.J. Dagher and S. Kulandran, *Finite element modelling of corrosion damage in concrete structures*, ACI Structural Journal, **89**, 6, 699-708 (1992)
- [3.24] R.A. Einsfeld; A.E. Elwi; T.N. Bittencourt; L.F. Martha, *Numerical simulation of fracturing in concrete structures using a combination of smeared and discrete approaches*. International Journal of Rock Mechanics and & Mining Science, **34**, 3-4, Paper No. 189 (1997)
- [3.25] CEB-FIB Model Code (1990)
- [3.26] Lusas, Theory Manual 1, Version 14
- [3.27] A. Hillerborg, M. Modeer and P.E. Petersson, *Analysis of crack formation and crack growth in concrete by means of fracture mechanics and finite elements*, Cement and Concrete Research, **6**, 773-782 (1979)
- [3.28] C. Andrade, C. Alonso, and F.J. Molina, *Cover cracking as a function of bar corrosion: Part 1 – Experimental test*, Materials and Structure, **26**, 453-464 (1993)
- [3.29] J.G. Cabrera, *Deterioration of concrete due to reinforcement steel corrosion*, Cement & Concrete Composite, **18**, 47-59 (1996)

## CHAPTER 4 – EXPERIMENTAL WORK

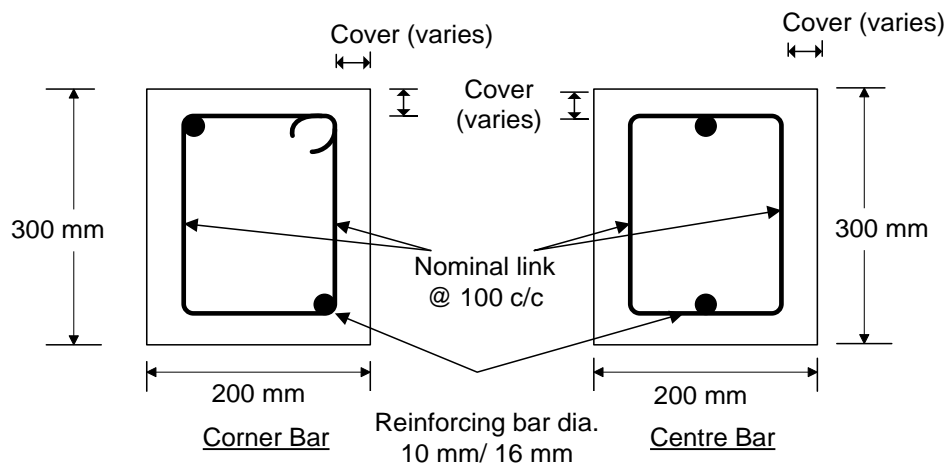
### 4.1 Outline of the Test Programme

In this experimental study, the beam end type bond test specimen was used. This beam end type specimen enables a condition to be created what is similar to that at the anchorage zone of a simply supported beam where the concrete and steel are under tension. The cross-section size was 200 mm x 300 mm, and the length of the specimen was 280 mm for the 10 mm reinforcing bar and 400 mm for the 16 mm reinforcing bar. The embedded lengths of the main bars were 185 mm for a 10 mm bar and 305 mm for a 16 mm bar, giving a bond length/bar diameter ratio of 18.5 and 19, respectively, to ensure bond failure prior to the yielding of the reinforcement. The specimens were divided into two groups depending on the location of the bar, which is located at either the corner or in the centre of a face (Figure 4.1). In previous work by others, four bars were tested for each specimen; however, the cracking caused by one failure tended to damage the adjacent untested bar [4.1][4.2]. Considering this factor, only two bars were provided in each specimen.

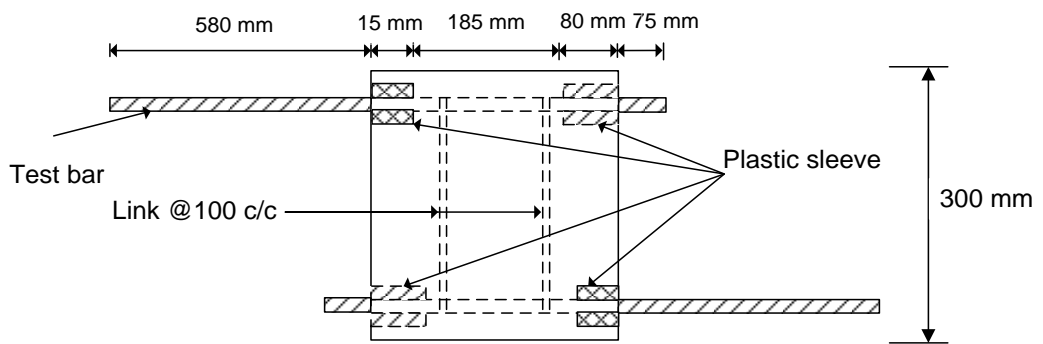
The pattern of cracking induced by reinforcement corrosion depends on the geometry of the concrete section. Two bar locations were therefore selected to represent a) a corner location, where confinement from concrete would (for a given corner) be weakest but the link most effective, and b) a centre location, where confinement from the surrounding concrete would be high but the link relatively ineffective.

Two corrosion rates were used, as it is known that this influences crack width, as discussed in section 2.3.1. By comparing the variation in residual strength for the two corrosion rates, it should be possible to determine which deterioration parameters correlate best with residual bond strength.

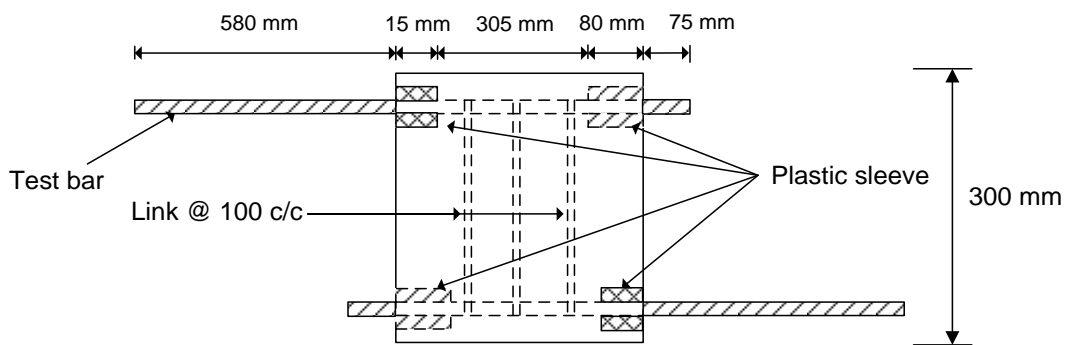
Because of the long anchorage length used in this study ( $> 18\phi_b$ ), the corrosion level was limited to avoid yield failure during the bond test.



**Specimen cross-section**



**a) 10 mm Bar**



**b) 16 mm Bar**

Figure 4.1: Details of specimens

(NTS)

## 4.2 Design of Test Specimens

### 4.2.1 Material properties

Ready-mix concrete with a designed compressive strength of 25 MPa at 28 days was used in the concreting work. The water/cement ratio was 0.5, and the maximum aggregate size was 10 mm. 3% sodium chloride by weight of cement was then added to the concrete mix to provide a corrosive environment in the concrete. Deformed steel bars of 10 mm and 16 mm in diameter were used for the main reinforcement in the specimens, while 6 mm plain bars with 100 mm spacing over the bond length were used as transverse reinforcement.

The concreting work was carried out in two batches. Thirty beams were cast in each batch, comprising 10 control specimens, and another 20 to be corroded (Figure 3.2). For identification, each reinforcing bar was labelled based on its bar diameter, cover thickness, corrosion rate, position, location, and casting batch.

During the concreting work, 15 100 mm x 100 mm x 100 mm cubes and six cylinders 150 mm in diameter and 300 mm long were prepared for each batch. These cubes and cylinders were used to determine the compressive strength and splitting tensile strength of the concrete. The compression test was conducted at 28 days for control purposes and on the day that the bond test was conducted. The results of the compression test are presented in Tables 4.1 and 4.2.

Cube	Maximum load (kN)	Area (mm <sup>2</sup> )	$F_{cu}$ (N/mm <sup>2</sup> )
1	465.7	1.00E+04	46.57
2	442.5	1.00E+04	44.25
3	438.7	1.00E+04	43.87
		Average	44.9

Table 4.1: First batch concrete strength at 28 days

Cube	Maximum load (kN)	Area (mm <sup>2</sup> )	$F_{cu}$ (N/mm <sup>2</sup> )
1	424.3	1.00E+04	42.43
2	391.9	1.00E+04	39.19
3	401.6	1.00E+04	40.16
		Average	40.6

Table 4.2: Second batch concrete strength at 28 days



Figure 4.2: 30 beam end type specimens ready for concreting

For the tensile splitting test, three cylinder specimens were tested under a splitting load according to ASTM C496-90 [4.3]. During the test, the cylinder specimens were placed in the centring machine cross head, and 3 mm thick plywood strips were placed along the top and bottom of the cylinders. The splitting strength was calculated using the following equation:

$$f_{sp} = \frac{2P}{\pi dl} \quad (4.1)$$

where

- $P$  - Maximum load (N)
- $d$  - Cylinder diameter (mm)
- $l$  - Length of cylinder (mm)

The results for both batches are presented in Tables 4.3 and 4.4

Cylinder	Max load (kN)	Tensile Strength (N/mm <sup>2</sup> )
1	179.9	2.53
2	227.3	3.21
3	207.3	2.93
Average		2.89

Table 4.3: First batch concrete splitting tensile test

Cylinder	Max load (kN)	Tensile Strength (N/mm <sup>2</sup> )
1	227.3	3.21
2	246.7	3.49
3	240.9	3.41
Average		3.36

Table 4.4: Second batch concrete splitting tensile test

#### ***4.2.2 Specimen manufacture***

The reinforcing bars were wire-brushed to remove any loose mill scale rust and then weighed. An 80 mm PVC sleeve was installed at the free end of the bonded length to cover the bar end underneath the transverse restraint to prevent a possible enhancement of the bond resulting from an external restraining force (Figure 4.3). A 15 mm PVC sleeve was sealed and placed between the steel and the concrete connection to prevent corrosion at the loaded end area. A thin silicone paste was applied under the PVC sleeve to provide a gap between the sleeve and reinforcing bar. After that, each formwork was oiled on the internal surface, and then the rebar was placed in the formwork. Only the bonded length of the main bars was corroded; the exposed part of the bars was covered with a plastic tube to isolate these parts from corrosion.

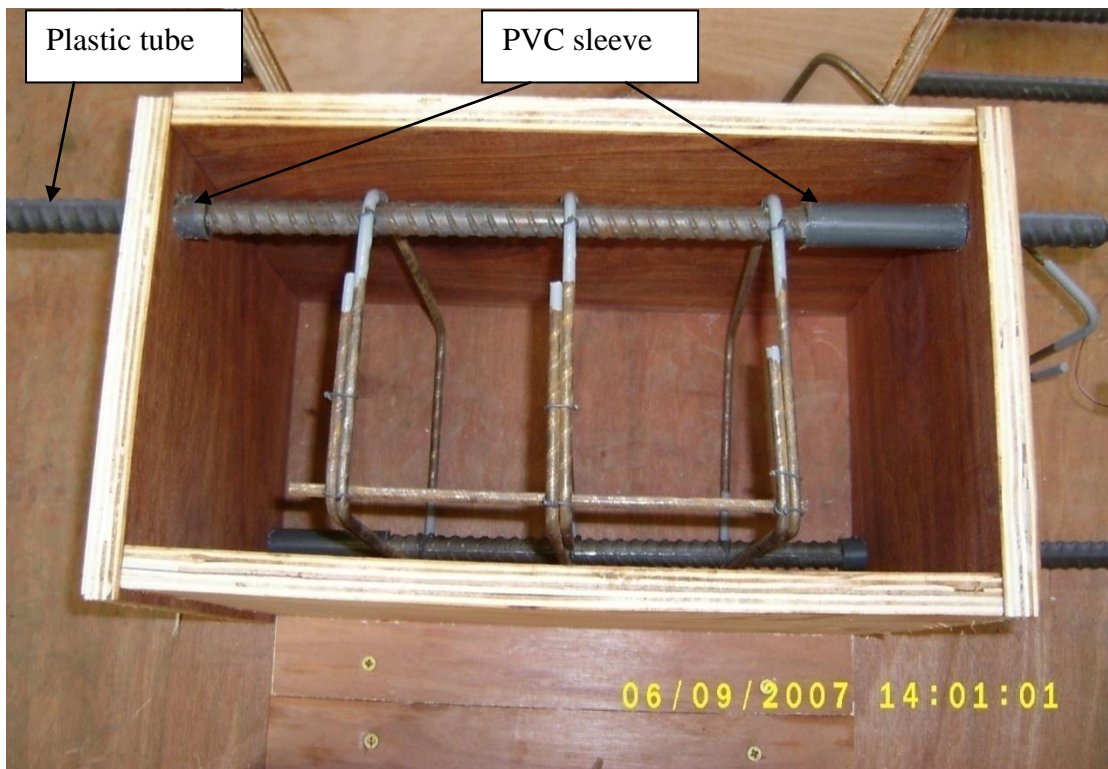


Figure 4.3: Location of 80 mm and 15 mm plastic sleeves

The details of the control specimens (no corrosion) are shown in Tables 4.5 and 4.6 for the first and second batch, respectively. The cover-to-diameter ratios for both batches were 1, 1.6, and 2.5. Two different cover thickness measurements were used for each batch; for the first batch, a minimum cover thickness measured to the stirrup was used, as in concrete design codes of practice, while for the second batch, the cover was taken to the main reinforcement, the measure commonly used by researchers on reinforced concrete corrosion studies.

The specimens were covered with polythene after casting. After 24 hours, the specimens were demoulded from the formwork. The specimens were cured under wet hessian and polythene for up to seven days and then in air in the laboratory until 28 days before commencing the corrosion process. The control specimens were stored in the laboratory and tested at the same age as the 'fast' corrosion specimens (see the next section).



Corrosion condition	Bar test ref.	Bar diameter, $\phi_b$ (mm)	Minimum cover to main bar, $c$ (mm)	$c/\phi_b$ ratio	Main bar	
					Position	Location
Control	10/1.6/TC/1	10	22	2.2	Top	Corner
	10/1.6/BC/1	10	22	2.2	Bottom	Corner
	10/2.5/TC/1	10	31	3.1	Top	Corner
	10/2.5/BC/1	10	31	3.1	Bottom	Corner
	10/1.6/TCe/1	10	22	2.2	Top	Centre
	10/1.6/BCe/1	10	22	2.2	Bottom	Centre
	10/2.5/TCe/1	10	31	3.1	Top	Centre
	10/2.5/BCe/1	10	31	3.1	Bottom	Centre
	16/1.0/TC/1	16	22	1.4	Top	Corner
	16/1.0/BC/1	16	22	1.4	Bottom	Corner
	16/1.6/TC/1	16	31	1.9	Top	Corner
	16/1.6/BC/1	16	31	1.9	Bottom	Corner
	16/2.5/TC/1	16	46	2.9	Top	Corner
	16/2.5/BC/1	16	46	2.9	Bottom	Corner
	16/1.0/TCe/1	16	22	1.4	Top	Centre
	16/1.0/BCe/1	16	22	1.4	Bottom	Centre
	16/1.6/TCe/1	16	31	1.9	Top	Centre
	16/1.6/BCe/1	16	31	1.9	Bottom	Centre
	16/2.5/TCe/1	16	46	2.9	Top	Centre
	16/2.5/BCe/1	16	46	2.9	Bottom	Centre

Table 4.5: First batch control specimen details

Corrosion condition	Bar test ref.	Bar diameter, $\phi_b$ (mm)	Minimum cover to main bar, $c$ (mm)	$c/\phi_b$ ratio	Main bar	
					Position	Location
Control	10/1.6/TC/2	10	16	1.6	Top	Corner
	10/1.6/BC/2	10	16	1.6	Bottom	Corner
	10/2.5/TC/2	10	25	2.5	Top	Corner
	10/2.5/BC/2	10	25	2.5	Bottom	Corner
	10/1.6/TCe/2	10	16	1.6	Top	Centre
	10/1.6/BCe/2	10	16	1.6	Bottom	Centre
	10/2.5/TCe/2	10	25	2.5	Top	Centre
	10/2.5/BCe/2	10	25	2.5	Bottom	Centre
	16/1.0/TC/2	16	16	1.0	Top	Corner
	16/1.0/BC/2	16	16	1.0	Bottom	Corner
	16/1.6/TC/2	16	25	1.6	Top	Corner
	16/1.6/BC/2	16	25	1.6	Bottom	Corner
	16/2.5/TC/2	16	40	2.5	Top	Corner
	16/2.5/BC/2	16	40	2.5	Bottom	Corner
	16/1.0/TCe/2	16	16	1.0	Top	Centre
	16/1.0/BCe/2	16	16	1.0	Bottom	Centre
	16/1.6/TCe/2	16	25	1.6	Top	Centre
	16/1.6/BCe/2	16	25	1.6	Bottom	Centre
	16/2.5/TCe/2	16	40	2.5	Top	Centre
	16/2.5/BCe/2	16	40	2.5	Bottom	Centre

Table 4.6: Second batch control specimen details

### 4.2.3 Corrosion conditioning

The specimens for corrosion were subjected to a cycle of 24 hours of wetting followed by 6 days' application of the impressed current. During the wetting period, the current was terminated, and the specimens were sprayed with a solution with a 3% (by weight) sodium chloride (*NaCl*) concentration. This type of corrosion condition was selected over full or partial immersion in a salt solution, widely used by many researchers previously, to represent better exposure conditions (dry and wet cycle) of concrete structures during their service life.

Two corrosion rates were used, as it is known that this influences crack width. As discussed in Chapter 2, a current density greater than 1 mA/cm<sup>2</sup> has an impact on the expansive behaviour of corrosion products that significantly reduces the bond strength, while the maximum recorded on site was 0.001 to 0.01 mA/cm<sup>2</sup>. The ideal current density as recommended by Saifullah and Clark [4.4] is no greater than 0.25 mA/cm<sup>2</sup>. Therefore, in this study, two different impressed current densities were chosen to better understand the effects of the impressed current on bond strength: one was limited to 0.4 mA/cm<sup>2</sup> and the other to 0.08 mA/cm<sup>2</sup>, referred to here as “fast” current and “slow” currents, respectively. The specimen details for these two impressed currents are presented in Tables 4.7–4.10 for both batches.

Corrosion condition	Bar test ref.	Bar diameter, $\phi_b$ (mm)	Minimum cover to main bar, $c$ (mm)	$c/\phi_b$ ratio	Bar position & location
"Fast" corrosion	10/1.6/F/TC/1	10	22	2.2	Top corner
	10/1.6/F/BC/1	10	22	2.2	Bottom corner
	10/2.5/F/TC/1	10	31	3.1	Top corner
	10/2.5/F/BC/1	10	31	3.1	Bottom corner
	10/1.6/F/TCe/1	10	22	2.2	Top centre
	10/1.6/F/BCe/1	10	22	2.2	Bottom centre
	10/2.5/F/TCe/1	10	31	3.1	Top centre
	10/2.5/F/BCe/1	10	31	3.1	Bottom centre
	16/1.0/F/TC/1	16	22	1.4	Top corner
	16/1.0/F/BC/1	16	22	1.4	Bottom corner
	16/1.6/F/TC/1	16	31	1.9	Top corner
	16/1.6/F/BC/1	16	31	1.9	Bottom corner
	16/2.5/F/TC/1	16	46	2.9	Top corner
	16/2.5/F/BC/1	16	46	2.9	Bottom corner
	16/1.0/F/TCe/1	16	22	1.4	Top centre
	16/1.0/F/BCe/1	16	22	1.4	Bottom centre
	16/1.6/F/TCe/1	16	31	1.9	Top centre
	16/1.6/F/BCe/1	16	31	1.9	Bottom centre
16/2.5/F/TCe/1	16	46	2.9	Top centre	
16/2.5/F/BCe/1	16	46	2.9	Bottom centre	

Table 4.7: Details of specimens with "fast" corrosion for the first batch

Corrosion condition	Bar test ref.	Bar diameter, $\phi_b$ (mm)	Minimum cover to main bar, $c$ (mm)	$c/\phi_b$ ratio	Bar position & location
"Fast" corrosion	10/1.6/F/TC/2	10	16	1.6	Top corner
	10/1.6/F/BC/2	10	16	1.6	Bottom corner
	10/2.5/F/TC/2	10	25	2.5	Top corner
	10/2.5/F/BC/2	10	25	2.5	Bottom corner
	10/1.6/F/TCe/2	10	16	1.6	Top centre
	10/1.6/F/BCe/2	10	16	1.6	Bottom centre
	10/2.5/F/TCe/2	10	25	2.5	Top centre
	10/2.5/F/BCe/2	10	25	2.5	Bottom centre
	16/1.0/F/TC/2	16	16	1.0	Top corner
	16/1.0/F/BC/2	16	16	1.0	Bottom corner
	16/1.6/F/TC/2	16	25	1.6	Top corner
	16/1.6/F/BC/2	16	25	1.6	Bottom corner
	16/2.5/F/TC/2	16	40	2.5	Top corner
	16/2.5/F/BC/2	16	40	2.5	Bottom corner
	16/1.0/F/TCe/2	16	16	1.0	Top centre
	16/1.0/F/BCe/2	16	16	1.0	Bottom centre
	16/1.6/F/TCe/2	16	25	1.6	Top centre
	16/1.6/F/BCe/2	16	25	1.6	Bottom centre
16/2.5/F/TCe/2	16	40	2.5	Top centre	
16/2.5/F/BCe/2	16	40	2.5	Bottom centre	

Table 4.8: Details of specimens with "fast" corrosion for the second batch

Corrosion condition	Bar test ref.	Bar diameter, $\phi_b$ (mm)	Minimum cover to main bar, $c$ (mm)	$c/\phi_b$ ratio	Bar position & location
"Slow" corrosion	10/1.6/S/TC/1	10	22	2.2	Top corner
	10/1.6/S/BC/1	10	22	2.2	Bottom corner
	10/2.5/S/TC/1	10	31	3.1	Top corner
	10/2.5/S/BC/1	10	31	3.1	Bottom corner
	10/1.6/S/TCe/1	10	22	2.2	Top centre
	10/1.6/S/BCe/1	10	22	2.2	Bottom centre
	10/2.5/S/TCe/1	10	31	3.1	Top centre
	10/2.5/S/BCe/1	10	31	3.1	Bottom centre
	16/1.0/S/TC/1	16	22	1.4	Top corner
	16/1.0/S/BC/1	16	22	1.4	Bottom corner
	16/1.6/S/TC/1	16	31	1.9	Top corner
	16/1.6/S/BC/1	16	31	1.9	Bottom corner
	16/2.5/S/TC/1	16	46	2.9	Top corner
	16/2.5/S/BC/1	16	46	2.9	Bottom corner
	16/1.0/S/TCe/1	16	22	1.4	Top centre
	16/1.0/S/BCe/1	16	22	1.4	Bottom centre
	16/1.6/S/TCe/1	16	31	1.9	Top centre
	16/1.6/S/BCe/1	16	31	1.9	Bottom centre
	16/2.5/S/TCe/1	16	46	2.9	Top centre
	16/2.5/S/BCe/1	16	46	2.9	Bottom centre

Table 4.9: Details of specimens with "slow" corrosion for the first batch

Corrosion condition	Bar test ref.	Bar diameter, $\phi_b$ (mm)	Minimum cover to main bar, $c$ (mm)	$c/\phi_b$ ratio	Bar position & location
"Slow" corrosion	10/1.6/S/TC/2	10	16	1.6	Top corner
	10/1.6/S/BC/2	10	16	1.6	Bottom corner
	10/2.5/S/TC/2	10	25	2.5	Top corner
	10/2.5/S/BC/2	10	25	2.5	Bottom corner
	10/1.6/S/TCe/2	10	16	1.6	Top centre
	10/1.6/S/BCe/2	10	16	1.6	Bottom centre
	10/2.5/S/TCe/2	10	25	2.5	Top centre
	10/2.5/S/BCe/2	10	25	2.5	Bottom centre
	16/1.0/S/TC/2	16	16	1.0	Top corner
	16/1.0/S/BC/2	16	16	1.0	Bottom corner
	16/1.6/S/TC/2	16	25	1.6	Top corner
	16/1.6/S/BC/2	16	25	1.6	Bottom corner
	16/2.5/S/TC/2	16	40	2.5	Top corner
	16/2.5/S/BC/2	16	40	2.5	Bottom corner
	16/1.0/S/TCe/2	16	16	1.0	Top centre
	16/1.0/S/BCe/2	16	16	1.0	Bottom centre
	16/1.6/S/TCe/2	16	25	1.6	Top centre
	16/1.6/S/BCe/2	16	25	1.6	Bottom centre
	16/2.5/S/TCe/2	16	40	2.5	Top centre
	16/2.5/S/BCe/2	16	40	2.5	Bottom centre

Table 4.10: Details of specimens with "slow" corrosion for the second batch

The direction of the current was set to cause the reinforcing bar to serve as an anode, while the stainless steel angle located at the near surface with the reinforcing bar acted as a cathode (Figure 4.4). The electrical contact between the concrete and a counter electrode was provided by a wet sponge. The wire connection between the power supply and reinforcing bar was connected in parallel rather in series, where separate wires were attached to each bar. This approach has proved to give a more uniform distribution of the corrosion produced among all the reinforcing bars [4.5]. The corrosion conditioning was divided into two groups for each batch. In the first group, the “fast” current specimens were placed in the conditioning pond and induced with “fast” current. The “slow” current specimens were subjected to the same process and induced with the “slow” current. During the conditioning process, a data logger was placed between the stainless steel and the power supply and then connected to a digital multimeter to record the value of the impressed current flowing through each bar at regular intervals. The potentiometer was placed between the power supply and the reinforcing bars to control the flow of the current running through each bar during the conditioning process. The current data was recorded every 6 seconds and stored in a computer.

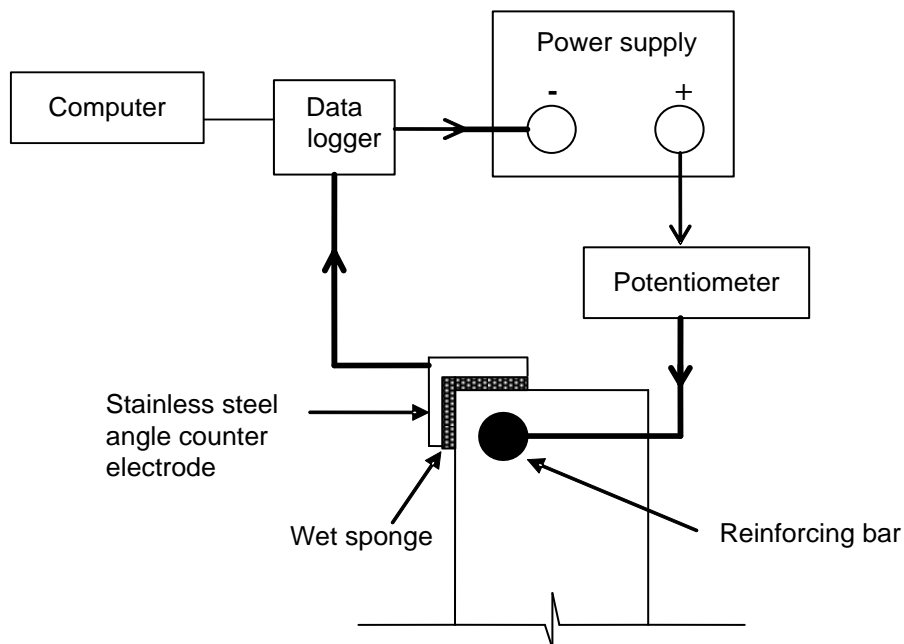


Figure 4.4: Anode arrangement for corrosion conditioning

The impressed current was terminated when the corrosion level on each bar reached 8% theoretical mass loss, corresponding to penetrations of 0.20 mm and 0.32 mm for the 10

mm and 16 mm bars, respectively. This theoretical mass loss value was calculated using Equation 2.4 from Chapter 2:

$$\Delta M_s = 2.862 \times 10^{-7} \pi \phi_b i_{corr} \Delta t \quad (\text{kg/m})$$

where  $\Delta M_s$  is the mass of steel consumed per unit length (kg/m),  $\phi_b$  is the initial diameter of the bar in metres,  $\Delta t$  is the time in seconds, and  $i_{corr}$  is the mean annual corrosion current per unit anodic surface area of steel (ampere per square metre).

Based on this equation, the time taken to achieve the 8% mass loss with a current density of 0.4 mA/cm<sup>2</sup> was estimated at 15.9 days for a 10 mm diameter bar and 25.3 days for a 16 mm diameter bar, while for a current density of 0.08 mA/cm<sup>2</sup> was estimated at 79.3 days for a 10 mm diameter bar and 126.7 days for a 16 mm diameter bar.

#### **4.2.4 Crack measurement**

After the impressed current was terminated, the specimens were left disconnected from the current source for a few days. During this time, surface crack width was measured. Readings were taken at 20 mm intervals along each bar. The average crack was calculated based on these total readings. The width of the cracks was measured using a graduated magnifier. In agreement with the numerical study of crack location, surface cracks were recorded at both faces adjacent to the corner bar. Therefore, the sum of the crack width that appeared on the beam surface was calculated using the model proposed by Vidal et al. [4.6] (Figure 4.5). Another method of crack measurement considered in this study was taking  $w_{cr,max}$  as the greater width ( $w_1, w_2$ ) of cracks in two adjacent faces.

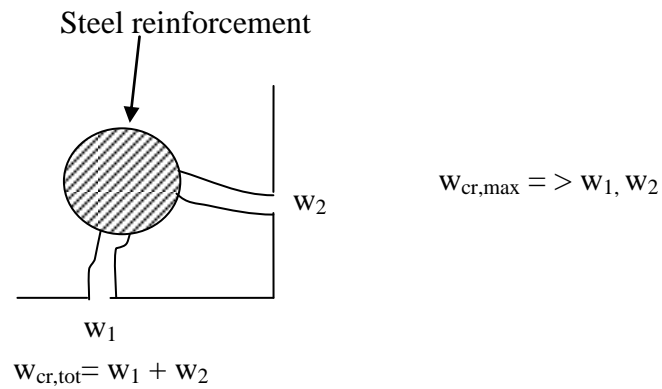


Figure 4.5: Crack configuration [4.6]

#### 4.2.5 Bond test loading procedure

The testing setup for the specimens is similar to that used by Chana [4.1], where each bar was subjected to axial tension force until failure and the maximum was considered the failure load. During the test, the free end slip was measured by a single linear variable differential transducer (LVDT) at the end of the specimen, while two LVDTs were placed at the front of the specimen to measure the loaded end slip (Figure 4.6).

All these slip measuring devices were connected to the computer and all the slip and load measurements were recorded automatically using the inbuilt data logger software on the computer. The increment of the load was done by a screw jack that moved the load shaft by turning the load lever plate, and it was moved based on the drive sleeve thread. This type of jack was used to provide a constant rate of displacement to the bar.

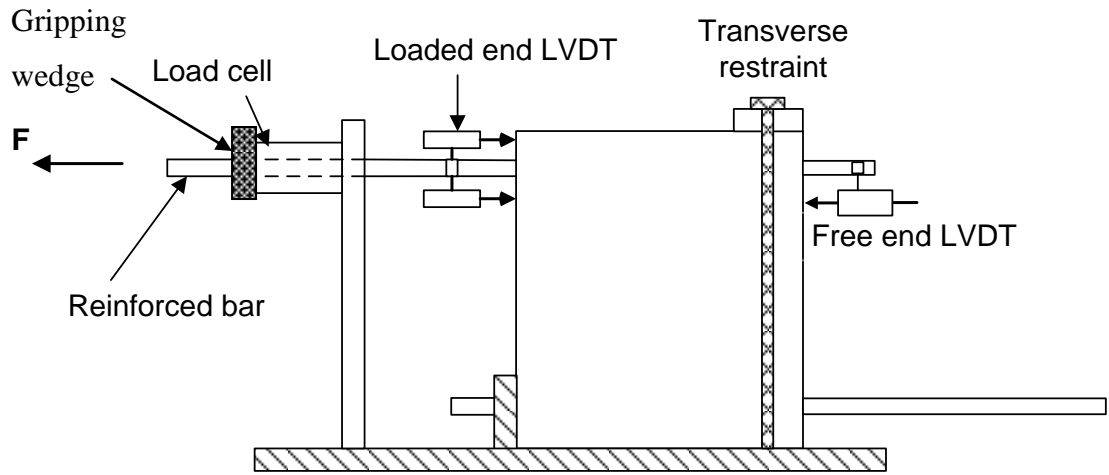


Figure 4.6: Bond test setup

#### 4.2.6 Corrosion rate measurement

Visual examination of the reinforcing bars after the bond test confirmed that corrosion was restricted to the bonded length. The actual degree of corrosion was measured using the gravimetric weight loss method where the weight of the reinforced bar was measured before and after the corrosion conditioning process. In determining the weight loss, the bars were removed from the tested specimens and the rust was cleaned with a wire brush; then each bar was soaked overnight in an acid solution with 12% acid hydrochloric concentration. During this cleaning process, the un-corroded reference bar was soaked together with the corroded bar to determine the mass loss from the erosion of metal during this process. The bar was then cleaned again with a wire brush and washed with distilled water. A 0.1M calcium hydroxide solution was sprayed on the bar to neutralize the acid. The bar was weighed after being dried in the laboratory. The percentage of mass loss for the bonded length of the bar was calculated using Equation 2.5:

$$\text{Mass loss } (m_{\text{loss}}) = \frac{G_0 - G}{g_0 l} \times 100\%$$

where

- $G_0$  - Initial weight of the test bar (g)
- $G$  - Final weight of the test bar (after cleaning the corrosion products) (g)
- $g_0$  - Weight per unit length of the test bar (g/mm)
- $l$  - Corroded length (mm)



As in Equation 2.7 in Chapter 2,  $\frac{\Delta m}{m_s} \times 100\%$  is the percentage of mass loss; thus, the percentage of section loss can be calculated as follows:

$$m_{loss} (\%) = A_{s_{loss}} (\%) \quad (4.2)$$

where  $m_{loss}$  is the mass loss from Equation 2.5 and  $A_{s_{loss}}$  is the section loss.

The corrosion penetration,  $x$  in millimetres, is calculated using the following equation:

$$x = r_s - \sqrt{(1 - m_{loss})(r_s^2)} \quad (4.3)$$

where  $r_s$  is the sound steel radius (mm) and  $m_{loss}$  is the mass loss from Equation 2.5.

### 4.3 References

- [4.1] P.S. Chana, *A test method to establish realistic bond stresses*, Magazine of Concrete Research, **42**, 151, 83-90 (1990)
- [4.2] D. Tang, *Influence of chloride-induced corrosion cracks on the strength of reinforced concrete*, Master Engineering Thesis, RMIT University (2007)
- [4.3] ASTM C496-90
- [4.4] M Saifullah, and L.A. Clark, *Effect of corrosion rate on the bond strength of corroded reinforcement*, Corrosion and Corrosion Protection of Steel in Concrete, Sheffield Academic Press, UK (1994)
- [4.5] K. Stanish, R.D. Hooton and S.J. Pantazopoulou, *Corrosion effects on bond strength in reinforced concrete*, ACI Structural Journal, **96**, 6, 915-921 (1999)
- [4.6] T. Vidal, A. Castel, and R.Francois, *Analyzing crack width to predict corrosion in reinforced concrete*, Cement and Concrete Research, **34**, 165-174 (2004)

## CHAPTER 5 – PRESENTATION AND DISCUSSION OF EXPERIMENTAL RESULTS

### 5.1 Introduction

This chapter is divided into two sections. Section 5.2 describes the measuring techniques used to quantify surface crack width, section loss, corrosion penetration, and bond strength and the parameters used in their measurements. All these experimental measurements are then tabulated and presented. Section 5.3 focuses on the analysis and discussion of the experimental results described in the previous section. The analysis of the experimental data starts with the average impressed current used in corrosion conditioning and the final amount of mass loss by each bar owing to corrosion. The analysis then focuses on the corrosion crack width and its relation to the main bar corrosion and proceeds to quantify the influence of corrosion on bond strength. Other parameters included in this investigation are cover thickness, bar location, casting position, and casting batch. The findings derived from these analyses are compared with the experimental results from previous investigations by other researchers and discussed accordingly. Through this comparison and discussion, the results of this study can be better justified.

### 5.2 Presentation of Experimental Results

#### *5.2.1 Measurement of surface crack width*

The average surface crack width is used in the analysis. This value was calculated based on the average of five individual measurements at 20 mm intervals along the length of the bar, recorded after the corrosion conditioning. An example of the measurement is shown in Figure 5.1, where  $w_{cr,tot}$  and  $w_{cr,max}$  are defined in Chapter 3.

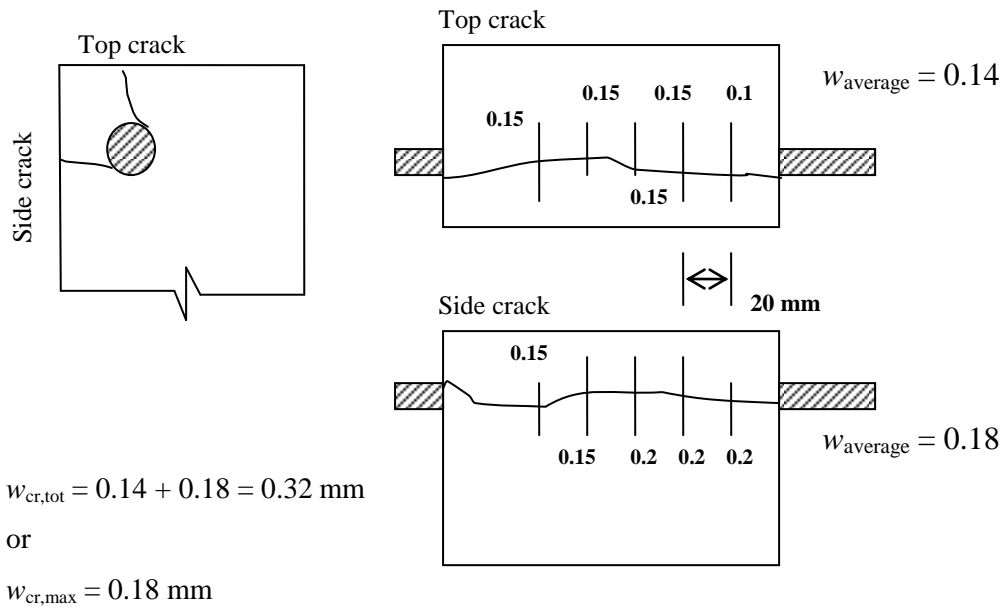


Figure 5.1: Surface crack measurement

### 5.2.2 Bar section loss and corrosion penetration

The impressed current values recorded on the data logger for each bar were integrated to obtain the total charge impressed on each bar over the conditioning period, which was then used to calculate theoretical section loss based on Equation 2.4. The total charge was divided by the duration of the applied current to obtain the average impressed current for each specimen over the entire duration of conditioning. Average current density was then obtained by dividing the average impressed current by the exposed surface area of the bar.

As discussed previously in Section 4.2.6, two corrosion measurements were used in this study. The section loss was calculated directly from the mass loss of the steel reinforcing bar in the bonded area by using Equation 2.5. The conversion from the mass loss to the section loss was based on Equation 4.2 and expressed as a percentage. The corrosion penetration is the reduction of reinforcing bar radius due to corrosion averaged over the bond area and was measured in millimeters and calculated from the section loss using Equation 4.3.

### 5.2.3 Bond test results

Bond strength ( $f_b$ ) was calculated from the recorded maximum force before the specimen failed. The conversion from the maximum bond force to the bond strength was carried out using the following equation:

$$f_b \text{ (MPa)} = \frac{P}{\pi \phi_b L} \quad (5.1)$$

where  $P$  is the maximum bond load (N);  $\phi_b$  is the main bar diameter (mm), and  $L$  is the bonded length (mm).

As mentioned in Chapter 4, a single LVDT was placed at the free end of the main reinforcing bar to measure the free-end slip. Typical graphs for bond load versus slip are plotted in Figure 5.2. The bottom-cast bars resist a higher load, which was reached at a markedly lower slip.

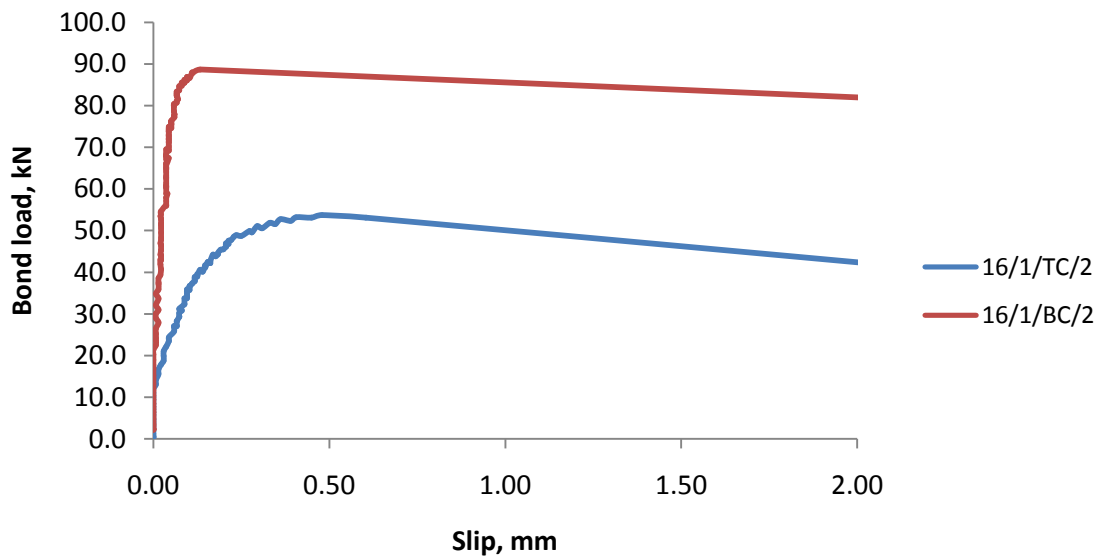


Figure 5.2: Bond slip diagram for the top cast and the bottom cast specimen (note: T = top-cast, B = bottom-cast, C = corner bar location)

#### **5.2.4 Failure mode of bond test**

The typical mode of failure for each type of specimen is shown in Figure 5.3 for the corner bar and in Figure 5.4 for the centre bar locations. The splitting mode of failure was observed for both sizes of the main bar and for both bar locations and casting positions. The same failure mode was observed by Chana [5.1] for a similar corner bar arrangement because of a small cover-to-diameter ratio and shielding of the bar by the PVC sleeve from transverse compression owing to the free-end reaction. However, some specimens failed in a pull-out mode with the concrete corbels between ribs sheared off, whereas some of the specimens reinforced with a 10 mm diameter bar failed due to yielding of the main bars. The failure mode for each specimen is recorded in Tables 5.1 to 5.4.

For the splitting failure mode, a longitudinal splitting crack had been observed before peak load was reached. In specimens with the corner bar location, the cracks appeared on the top and side faces, whereas in specimens with the centre bar location, the splitting cracks formed on the top face of the specimens.



Figure 5.3: Splitting failure for corner bar location (specimen 10/2.5/BC/2)



Figure 5.4: Splitting failure for centre bar location (specimen 16/1.6/TCe/2)

### ***5.2.5 Analysis of experimental results***

Results for all tested bars are presented in Tables 5.1 and 5.2 for control (i.e., uncorroded) specimens and Tables 5.3 and 5.4 for corroded specimens. Both control and corroded test data are grouped according to the casting batches. The section loss and corrosion penetration for corroded specimens were obtained from gravimetric measurements.

<b>Bar ID</b>	$\phi_b$ <b>(mm)</b>	<b>Cover to main bar, <math>c</math> (mm)</b>	$f_b$ <b>(MPa)</b>	<b>Failure mode</b>
10/1.6/TC/1	10	22	4.99	Splitting
10/1.6/BC/1	10	22	7.08	Pullout
10/1.6/TCe/1	10	22	6.97	Splitting
10/1.6/BCe/1	10	22	7.64	Yield
10/2.5/TC/1	10	31	5.39	Splitting
10/2.5/BC/1	10	31	8.61	Yield
10/2.5/TCe/1	10	31	6.54	Splitting
10/2.5/BCe/1	10	31	8.06	Yield
16/1.0/TC/1	16	22	4.79	Splitting
16/1.0/BC/1	16	22	5.34	Splitting
16/1.0/TCe/1	16	22	4.82	Splitting
16/1.0/BCe/1	16	22	6.64	Splitting
16/1.6/TC/1	16	31	5.35	Splitting
16/1.6/BC/1	16	31	5.71	Splitting
16/1.6/TCe/1	16	31	4.89	Splitting
16/1.6/BCe/1	16	31	6.25	Splitting
16/2.5/TC/1	16	46	5.63	Splitting
16/2.5/BC/1	16	46	6.75	Splitting
16/2.5/TCe/1	16	46	5.82	Splitting
16/2.5/BCe/1	16	46	6.75	Splitting

Table 5.1: Bond strength of control specimens - first batch (T = top-cast, B = bottom-cast, C = corner bar location, Ce = centre bar location)

<b>Bar ID</b>	$\phi_b$ <b>(mm)</b>	<b>Cover to main bar, <math>c</math> (mm)</b>	$f_b$ <b>(MPa)</b>	<b>Failure mode</b>
10/1.6/TC/2	10	16	3.70	Pullout
10/1.6/BC/2	10	16	7.48	Splitting
10/1.6/TCe/2	10	16	6.03	Splitting
10/1.6/BCe/2	10	16	8.74	Yield
10/2.5/TC/2	10	25	4.87	Splitting
10/2.5/BC/2	10	25	8.35	Pullout
10/2.5/TCe/2	10	25	6.10	Splitting
10/2.5/BCe/2	10	25	8.05	Yield
16/1.0/TC/2	16	16	3.50	Splitting
16/1.0/BC/2	16	16	5.78	Pullout
16/1.0/TCe/2	16	16	4.31	Splitting
16/1.0/BCe/2	16	16	7.16	Splitting
16/1.6/TC/2	16	25	4.42	Splitting
16/1.6/BC/2	16	25	6.90	Splitting
16/1.6/TCe/2	16	25	4.99	Splitting
16/1.6/BCe/2	16	25	7.24	Splitting
16/2.5/TC/2	16	40	6.89	Splitting
16/2.5/BC/2	16	40	8.56	Splitting
16/2.5/TCe/2	16	40	5.36	Pullout
16/2.5/BCe/2	16	40	8.02	Splitting

Table 5.2: Bond strength of control specimens - second batch (T = top-cast, B = bottom-cast, C = corner bar location, Ce = centre bar location)



Bar ID	$\varnothing_b$ (mm)	Average current density (mA/cm <sup>2</sup> )	Crack width (mm)		Section loss (%)	Corrosion Penetration (mm)	$f_b$ (MPa)	Failure mode
			$w_{cr,tot}$	$w_{cr,max}$				
10/1.6/F/TC/1	10	0.31	0.20	0.20	8.10	0.207	5.41	Sp
10/1.6/F/BC/1	10	0.49	0.37	0.37	9.78	0.251	5.93	Sp
10/2.5/F/TC/1	10	0.48	0.18	0.18	9.87	0.253	6.50	Sp
10/2.5/F/BC/1	10	0.29	0.30	0.30	8.09	0.207	7.51	Sp
10/1.6/F/TCe/1	10	0.35	0.00	0.00	4.53	0.115	7.08	Sp
10/1.6/F/BCe/1	10	0.37	0.00	0.00	5.31	0.134	8.20	Y
10/2.5/F/TCe/1	10	0.40	0.09	0.09	7.22	0.184	7.02	Sp
10/2.5/F/BCe/1	10	0.31	0.07	0.07	6.24	0.159	7.72	Y
10/1.6/S/TC/1	10	0.09	0.00	0.00	4.40	0.111	6.35	Sp
10/1.6/S/BC/1	10	0.08	0.00	0.00	9.90	0.254	6.79	Sp
10/2.5/S/TC/1	10	0.08	0.00	0.00	5.36	0.136	7.24	Sp
10/2.5/S/BC/1	10	0.08	0.00	0.00	4.50	0.114	8.27	Sp
10/1.6/S/TCe/1	10	0.08	0.00	0.00	5.42	0.137	5.85	Sp
10/1.6/S/BCe/1	10	0.09	0.10	0.10	6.32	0.161	6.44	Sp
10/2.5/S/TCe/1	10	0.09	0.00	0.00	3.57	0.090	8.57	Sp
10/2.5/S/BCe/1	10	0.09	0.00	0.00	2.64	0.066	8.32	Sp
16/1.0/F/TC/1	16	0.44	0.56	0.4	7.10	0.290	5.17	Sp
16/1.0/F/BC/1	16	0.46	0.68	0.36	7.24	0.296	5.31	Sp
16/1.6/F/TC/1	16	0.39	0.56	0.56	6.85	0.279	6.29	P
16/1.6/F/BC/1	16	0.33	0.74	0.74	6.19	0.252	5.86	Sp
16/2.5/F/TC/1	16	0.45	0.42	0.42	6.66	0.272	4.59	Sp
16/2.5/F/BC/1	16	0.33	0.68	0.68	6.42	0.262	5.37	Sp
16/1.0/F/TCe/1	16	0.38	0.19	0.19	4.94	0.201	5.29	Sp
16/1.0/F/BCe/1	16	0.17	0.11	0.11	3.64	0.147	5.85	P
16/1.6/F/TCe/1	16	0.27	0.00	0.00	3.87	0.157	4.54	Sp
16/1.6/F/BCe/1	16	0.18	0.20	0.2	3.66	0.148	6.02	Sp
16/2.5/F/TCe/1	16	0.23	0.18	0.18	4.05	0.164	5.12	Sp
16/2.5/F/BCe/1	16	0.27	0.42	0.42	4.91	0.200	6.06	Sp
16/1.0/S/TC/1	16	0.08	0.48	0.48	10.67	0.439	5.88	Sp
16/1.0/S/BC/1	16	0.08	0.22	0.22	7.54	0.308	5.24	Sp
16/1.6/S/TC/1	16	0.08	0.37	0.37	9.70	0.398	5.64	Sp
16/1.6/S/BC/1	16	0.08	0.37	0.37	7.70	0.315	6.59	Sp
16/2.5/S/TC/1	16	0.07	0.42	0.42	8.33	0.341	6.83	Sp
16/2.5/S/BC/1	16	0.08	0.41	0.41	7.31	0.299	6.66	Sp
16/1.0/S/TCe/1	16	0.07	0.09	0.09	7.29	0.298	5.78	Sp
16/1.0/S/BCe/1	16	0.08	0.00	0.00	6.89	0.281	6.18	Sp
16/1.6/S/TCe/1	16	0.08	0.18	0.18	7.94	0.325	6.55	Sp
16/1.6/S/BCe/1	16	0.08	0.12	0.12	5.16	0.210	5.91	Sp
16/2.5/S/TCe/1	16	0.06	0.17	0.17	6.20	0.252	6.06	Sp
16/2.5/S/BCe/1	16	0.07	0.16	0.16	5.13	0.209	6.89	Sp

Note: T - top-cast, B - bottom-cast, C - corner bar location, Ce - centre bar location,

F - fast, S - slow, Y - yield, P - pullout, Sp - splitting

Table 5.3: First batch of corroded specimens

Bar ID	$\varnothing_b$ (mm)	Average current density (mA/cm <sup>2</sup> )	Crack width (mm)		Section loss (%)	Corrosion penetration (mm)	$f_b$ (MPa)	Failure mode
			$w_{cr,tot}$	$w_{cr,max}$				
10/1.6/F/TC/2	10	0.47	0.36	0.19	11.70	0.302	6.82	Sp
10/1.6/F/BC/2	10	0.24	0.18	0.18	2.67	0.067	8.29	Y
10/2.5/F/TC/2	10	0.32	0.18	0.18	8.12	0.207	7.19	Sp
10/2.5/F/BC/2	10	0.31	0.36	0.36	8.06	0.206	7.12	Y
10/1.6/F/TCe/2	10	0.36	0.00	0.00	9.82	0.252	6.97	Sp
10/1.6/F/BCe/2	10	0.19	0.00	0.00	4.45	0.113	8.79	Y
10/2.5/F/TCe/2	10	0.31	0.10	0.10	9.66	0.248	8.07	Sp
10/2.5/F/BCe/2	10	0.21	0.05	0.05	3.60	0.091	8.57	Y
10/1.6/S/TC/2	10	0.09	0.30	0.30	5.43	0.138	5.08	Sp
10/1.6/S/BC/2	10	0.07	0.17	0.17	5.36	0.136	7.79	P
10/2.5/S/TC/2	10	0.07	0.09	0.09	3.58	0.090	8.10	Sp
10/2.5/S/BC/2	10	0.09	0.36	0.36	7.18	0.183	7.32	P
10/1.6/S/TCe/2	10	0.09	0.05	0.05	10.8	0.278	7.37	Sp
10/1.6/S/BCe/2	10	0.06	0.05	0.05	6.28	0.160	8.07	Sp
10/2.5/S/TCe/2	10	0.10	0.04	0.04	9.78	0.251	8.14	Y
10/2.5/S/BCe/2	10	0.07	0.04	0.04	4.51	0.114	7.99	Sp
16/1.0/F/TC/2	16	0.49	0.52	0.52	7.90	0.323	5.09	Sp
16/1.0/F/BC/2	16	0.46	0.31	0.31	7.49	0.306	6.18	Sp
16/1.6/F/TC/2	16	0.50	0.47	0.47	7.89	0.323	5.50	Sp
16/1.6/F/BC/2	16	0.25	0.68	0.68	6.67	0.272	0.00	-
16/2.5/F/TC/2	16	0.34	0.41	0.41	7.08	0.289	6.19	Sp
16/2.5/F/BC/2	16	0.21	0.68	0.68	5.34	0.217	4.62	Sp
16/1.0/F/TCe/2	16	0.34	0.21	0.21	6.18	0.252	5.41	Sp
16/1.0/F/BCe/2	16	0.29	0.21	0.21	6.42	0.262	6.71	Sp
16/1.6/F/TCe/2	16	0.23	0.11	0.11	5.39	0.219	6.26	Sp
16/1.6/F/BCe/2	16	0.12	0.20	0.20	4.05	0.164	6.90	P
16/2.5/F/TCe/2	16	0.24	0.28	0.28	6.04	0.246	5.21	Sp
16/2.5/F/BCe/2	16	0.16	0.28	0.28	4.90	0.199	7.02	Sp
16/1.0/S/TC/2	16	0.08	0.27	0.14	6.62	0.270	5.17	Sp
16/1.0/S/BC/2	16	0.08	0.71	0.71	4.68	0.190	6.98	P
16/1.6/S/TC/2	16	0.09	0.68	0.37	8.53	0.349	5.57	Sp
16/1.6/S/BC/2	16	0.07	0.94	0.94	7.22	0.295	6.93	Sp
16/2.5/S/TC/2	16	0.07	0.69	0.69	7.95	0.325	7.39	P
16/2.5/S/BC/2	16	0.06	0.75	0.75	5.99	0.244	7.49	Sp
16/1.0/S/TCe/2	16	0.07	0.08	0.08	5.99	0.244	5.81	Sp
16/1.0/S/BCe/2	16	0.04	0.14	0.14	4.04	0.164	6.57	Sp
16/1.6/S/TCe/2	16	0.07	0.11	0.11	4.92	0.200	6.19	Sp
16/1.6/S/BCe/2	16	0.08	0.19	0.19	8.54	0.350	7.25	Sp
16/2.5/S/TCe/2	16	0.08	0.25	0.25	4.73	0.192	4.57	Sp
16/2.5/S/BCe/2	16	0.04	0.45	0.45	5.31	0.216	7.02	Sp

Note: T - top-cast, B - bottom-cast, C - corner bar location, Ce - centre bar location,

F - fast, S - slow, Y - yield, P - pullout, Sp - splitting

Table 5.4: Second batch of corroded specimens

## 5.3 Interpretation and Discussion of Experimental Results

### 5.3.1 Effects of impressed current on corrosion process

The summary of average impressed current density for each batch is presented in Table 5.5. As can be seen, the average current for “fast” specimens is in the range of 0.3–0.4 mA/cm<sup>2</sup>, whereas for the “slow” current, the value is averaged at approximately 0.08 mA/cm<sup>2</sup>.

The coefficient of variation (CoV) of each current was then calculated, which shows that a higher CoV value is experienced for the “fast” current than for the “slow” current for both casting batches. During corrosion conditioning, a potentiometer was installed between the power supply and the reinforcing bar to control the amount of current. The problem with the “fast” specimens was that the current tended to decrease for an unknown reason. Therefore, the current was checked and corrected twice daily. The fluctuation of the current is reflected by the higher CoV value in the table.

Casting batch	$\varnothing_b$ (mm)	Impressed current	Average current (mA/cm <sup>2</sup> )	Standard deviation	Coefficient of variation CoV
1	10	“fast”	0.375	0.075	0.200
	16	“fast”	0.324	0.102	0.315
	10	“slow”	0.085	0.003	0.035
	16	“slow”	0.076	0.005	0.066
2	10	“fast”	0.300	0.092	0.307
	16	“fast”	0.302	0.125	0.414
	10	“slow”	0.081	0.015	0.185
	16	“slow”	0.070	0.015	0.214

Table 5.5: Average impressed current for different casting batches and bar diameters

The amount of the current was then used to calculate the theoretical mass loss using Faraday’s law per Equation 2.4. The actual mass loss was determined from the net weight of the main reinforcing bars after the cleaning process and calculated using Equation 2.5. Data from these two measurements were compared to determine the consistency and accuracy of the impressed current technique in generating corrosion of the main reinforcing bars. Figures 5.5 and 5.6 show the comparison of the measurements for different bar diameters and casting batches. As can be seen from the figures, although the

general trend is that the two measurements are correlated, the results for the 16 mm diameter bars are less scattered than those for the 10 mm diameter bars.

A large scatter in results is observed for the 10 mm diameter bars impressed with “slow” current for both batches. The observation from this plot contrasts with an apparently good degree of control exercised on the impressed current for this group of bars, as evidenced by the low CoV values shown in Table 5.5, especially for the casting batch 1. Moreover, most of the points for the 10 mm diameter bars with “slow” current in Figures 5.5 and 5.6 are below the line of perfect agreement (i.e., 45° line), which means that the gravimetric mass loss for these bars is less than its theoretical value that is calculated based on the impressed current. Three specimens in the second batch experienced a longer period of corrosion conditioning to allow for crack to appear. However, the actual mass losses in these specimens were far lower than expected, as shown in Figure 5.6.

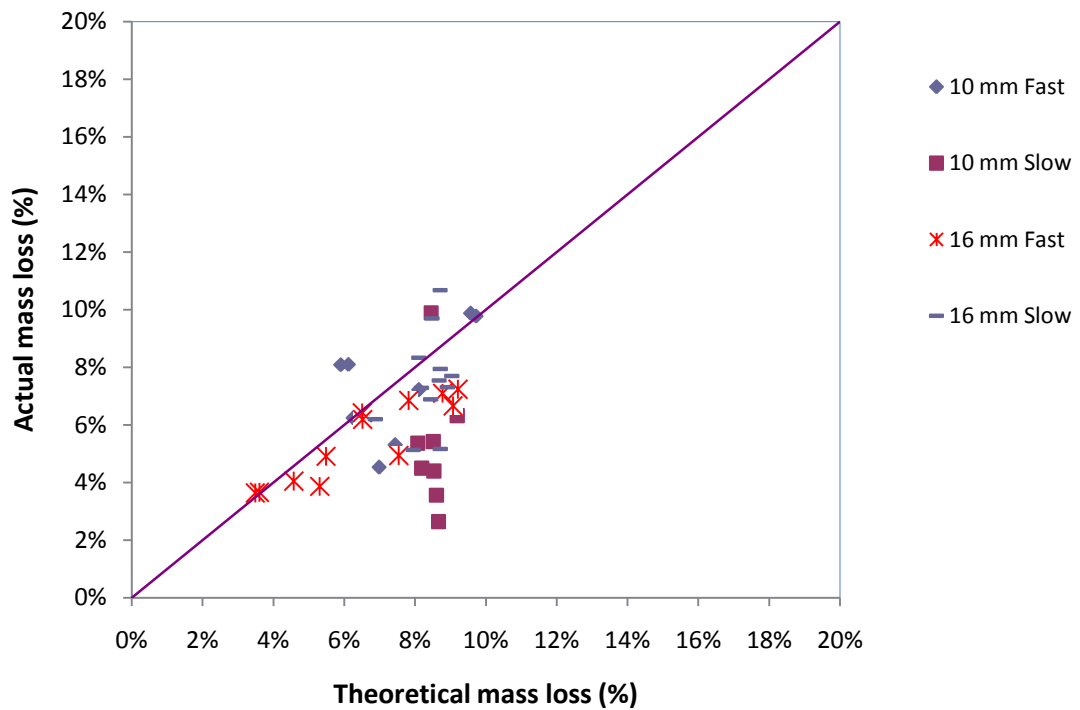


Figure 5.5: Actual versus theoretical mass loss of the first casting batch

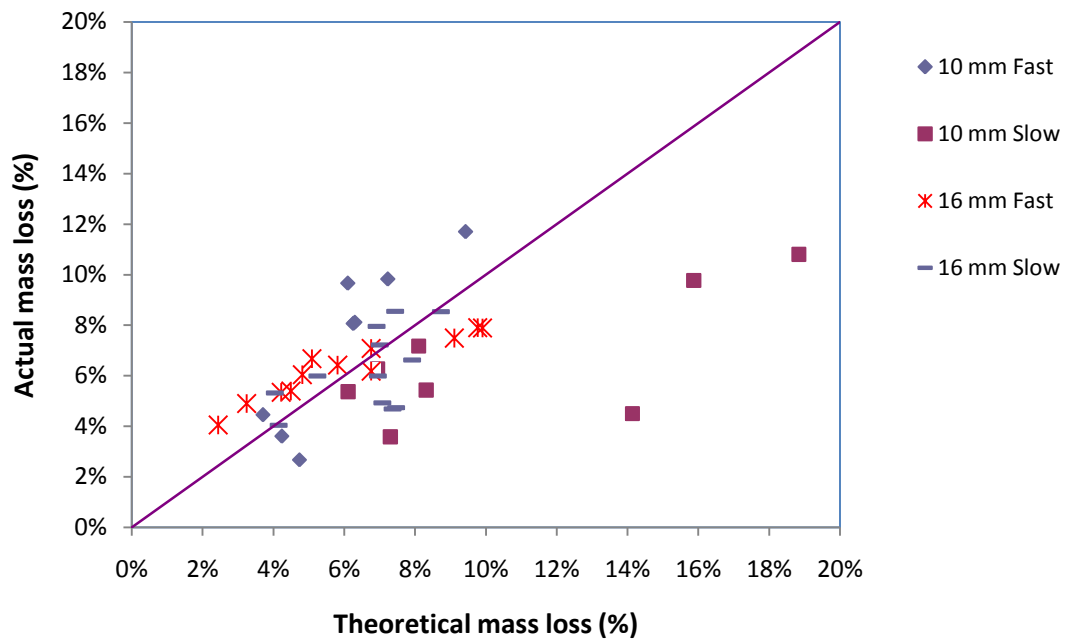
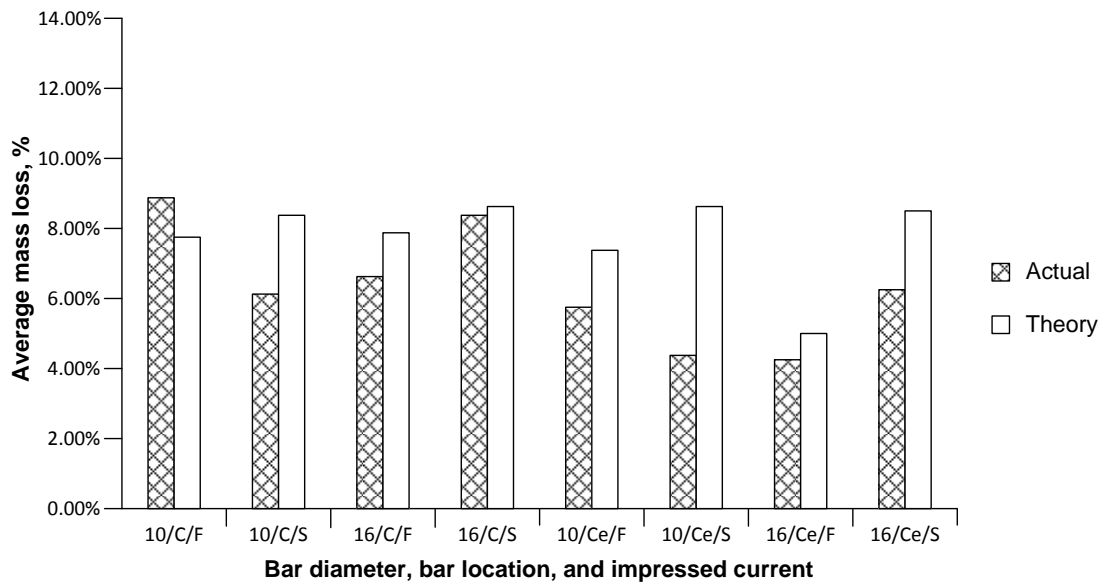
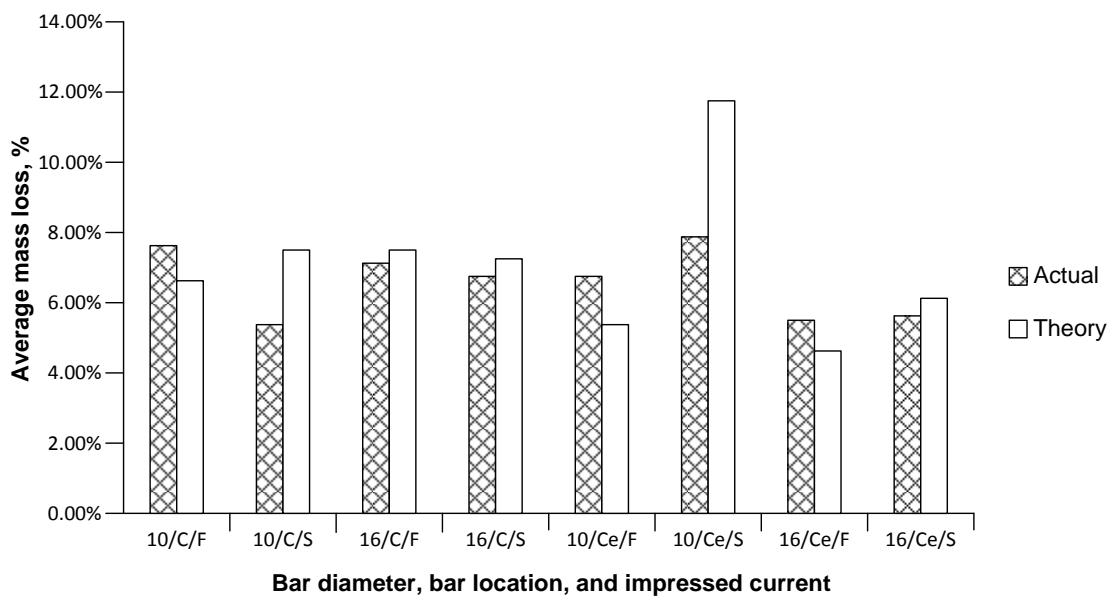


Figure 5.6: Actual versus theoretical mass loss of the second casting batch

The comparison of the theoretical versus average actual mass loss for different bar diameters and locations is presented in Figures 5.7(a) and (b) for the first and the second casting batches, respectively. Results show that most of the specimens have a higher theoretical mass loss compared with the actual mass loss for both casting batches. The largest differences between these two measurements are observed for the 10 mm diameter bars induced with slow current for which the theory and actual mass loss ratio ranges from 1.4 to 1.9. The difference between theoretical and actual mass loss was observed by previous researchers in their experimental works [5.2, 5.3]. According to Auyeung et al. [5.4], this difference was due to various factors, such as the need for electrical energy to initiate the corrosion, resistivity of concrete, composition of the bar, and electrical properties of minerals in concrete. However, in this study, this difference might result from the leaking of impressed current during the corrosion conditioning, thereby reducing the effectiveness of impressed current in accelerating the corrosion. The leakage occurred because the current was started after the specimens experienced a wetting process. In this wet condition, the impressed current can flow through an alternative path.



(a) First batch specimens



(b) Second batch specimens

Figure 5.7: Average theoretical and actual mass loss for different bar diameters, locations and impressed currents

To avoid any misinterpretation of the experimental data, the mass loss from the gravimetric method was used subsequently, because it showed the actual corrosion level of the main reinforcement. Therefore, the corrosion penetration and section loss used in the following analysis will be calculated based on the actual mass loss from gravimetric measurements.

### 5.3.2 Corrosion of main reinforcement

The gravimetric section losses from Tables 5.3 and 5.4, which were averaged by the bar diameter and casting position, are presented in Figures 5.8 and 5.9. The figures show the following trend in the section loss of the main reinforcement: most of the bars in the top-cast position had higher levels of corrosion than those in the bottom-cast position except of the 10-mm diameter bars in the first batch subjected to “slow” current. This trend can be explained by the known fact that the interface zone around top bars is more porous than that around bottom bars due to the plastic settlement. This condition permits easier access of water and oxygen to top bars and thus increases their corrosion level. The deviation from this trend of the top-cast 10-mm diameter bar “slow” specimens may be explained by the “leaking” of impressed current discussed in the previous section. These specimens had a very low current efficiency value where the ratio between the actual mass loss and the theoretical mass loss was only 56%. Moreover, no surface crack was observed in these top-cast specimens unlike in similar identical specimens in the second batch.

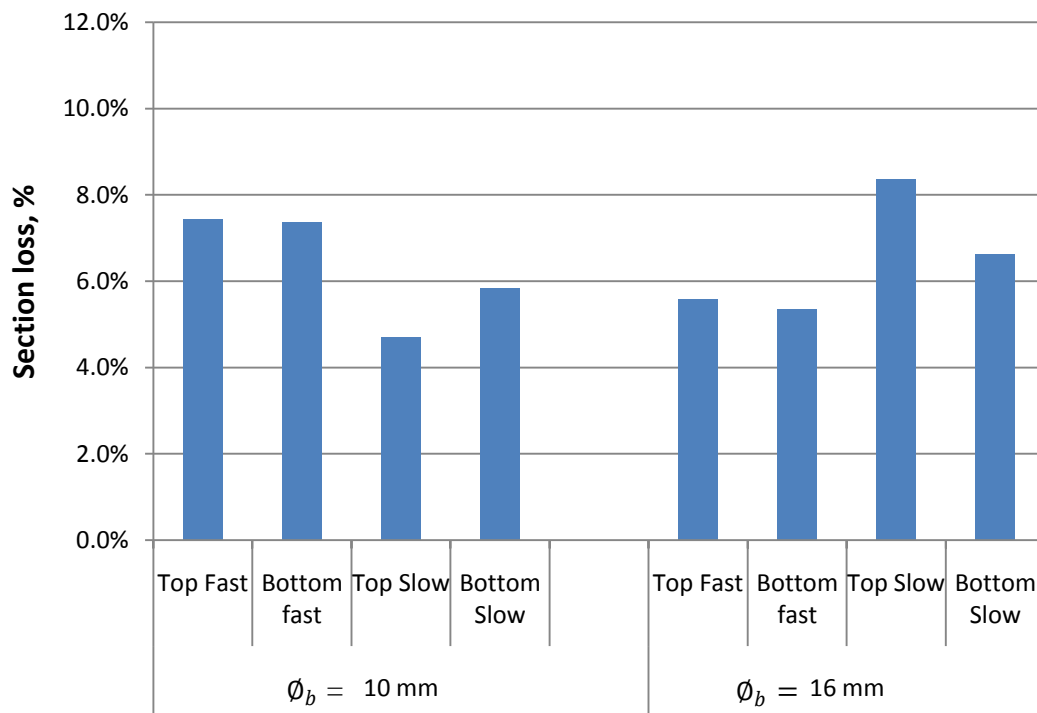


Figure 5.8: Average corrosion for the first batch

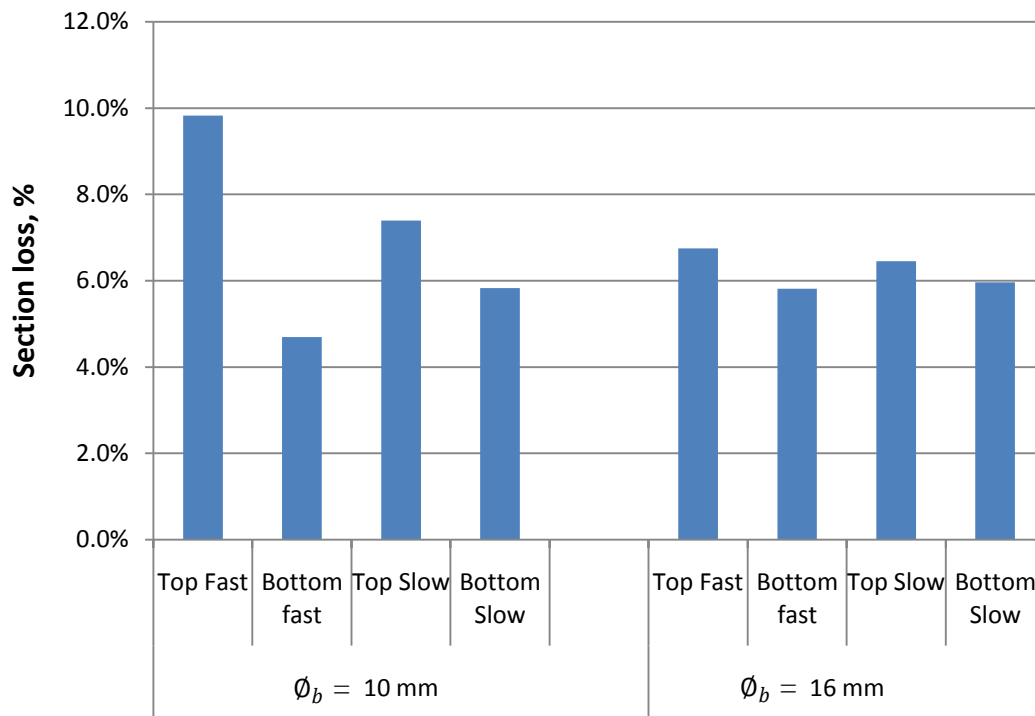


Figure 5.9: Average corrosion for the second batch

### 5.3.3 Corrosion-induced cracking

The expansion of rust products during the corrosion process led to the initiation and propagation of surface cracking. In this section, the discussion will start with the crack patterns and locations. Then, the relationship between the surface crack width and corrosion level measurements used in this study will be discussed.

#### 5.3.3.1 Crack pattern and location

In this study, from the 80 main reinforcing bars corroded at different locations and casting positions, 13 bars had no surface cracks even with a corrosion level of up to 9.9% of the section loss. Most of the “no surface cracking” cases were observed for the 10 mm diameter bars impressed with “slow” current. For the centre bar location, the surface cracks were parallel to the main bar (Figure 5.10) similar to those observed by other researchers. For the corner bar location, the cracks, either single or double, ran parallel to the bar on the near-concrete surface (Figure 5.11), again similar to those observed by other researchers. The influence of the bar diameter and cover thickness on the crack



pattern was negligible. Cracks on the adjacent faces were mainly observed for the top-cast corner bars.

Notably, some specimens as in Table 5.6 showed surface corrosion cracking along the transverse reinforcing bars, which were electrically isolated from the main bar using epoxy paint. As a result, no current was impressed through the transverse bars during the corrosion conditioning process. However, transverse cracking was still observed along the stirrups due to the corrosion of these bars. The amount of section loss on the main bar was unaffected by the presence of the corrosion on the transverse bars, whereas the actual corrosion on the main bar was higher than that theoretically predicted. Therefore, the stirrup corrosion might have resulted from the presence of chlorides in the concrete.

Specimen ID	Casting position	Batch	Current	Mass loss	
				Theory	Actual
10/2.5/F/TC	Top	2	"fast"	6.30%	8.12%
10/2.5/F/BC	Bottom	2	"fast"	6.26%	8.06%
16/2.5/F/TCe	Top	2	"fast"	4.81%	6.04%
16/1.6/F/TCe	Top	2	"fast"	4.49%	5.39%
16/1.6/F/BCe	Bottom	2	"fast"	2.44%	4.05%

Table 5.6: Theoretical and actual mass loss for specimens with corroded stirrups

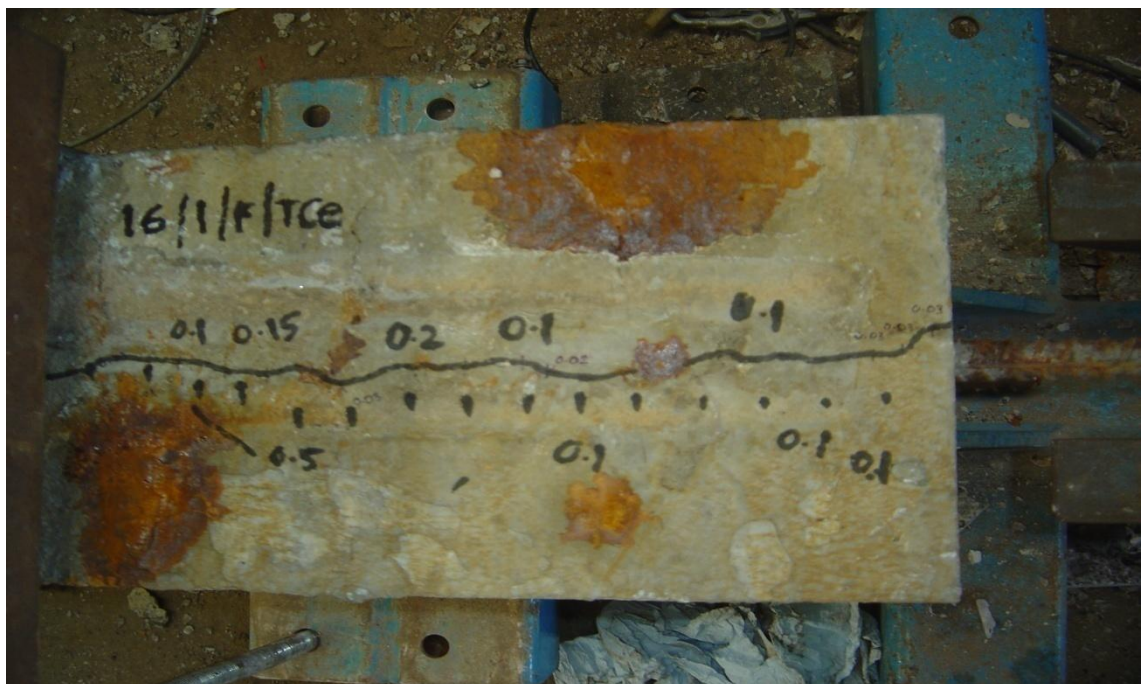


Figure 5.10: Longitudinal surface crack on centre bar location



Figure 5.11: Longitudinal surface crack on corner bar location

### ***5.3.3.2 Surface crack width***

#### ***5.3.3.2.1 Selection of crack width measure***

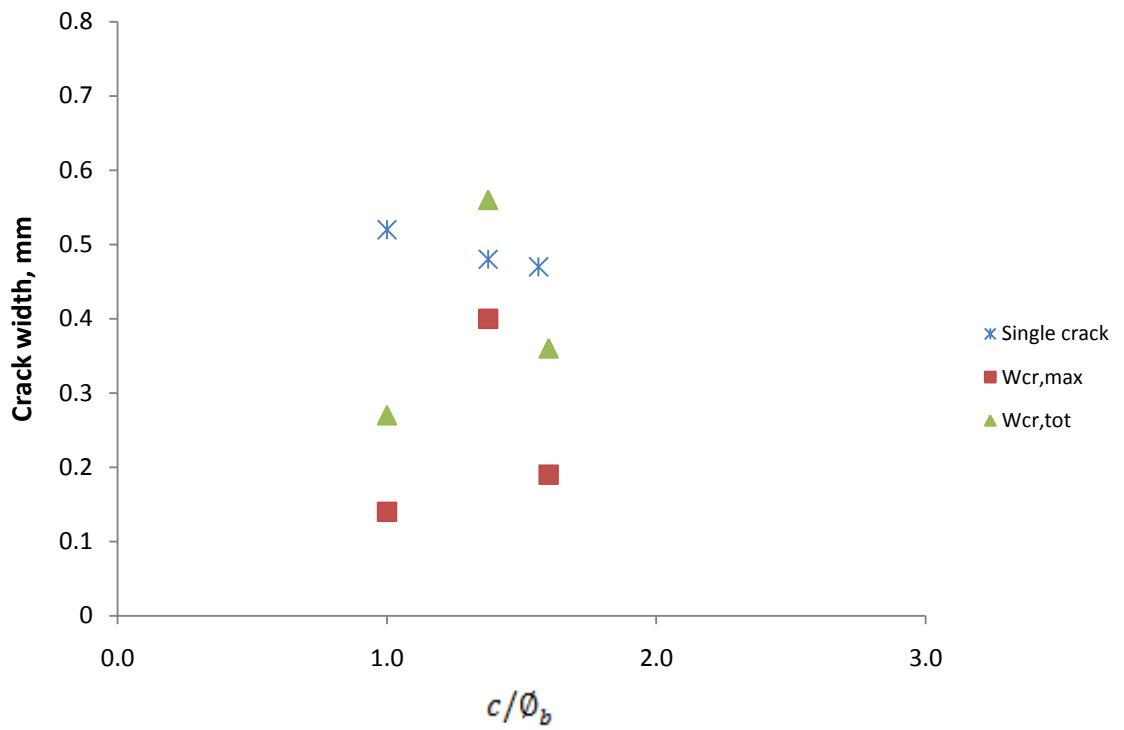
As discussed in Chapter 4 (Section 4.2.4) and shown previously in Tables 5.3 and 5.4, two measures of surface crack width ( $w_{cr,tot}$  and  $w_{cr,max}$ ) were used in this study. Out of the 80 tested bars, only six 16 mm diameter bars at corner locations had cracks on both adjacent faces and this crack pattern was not observed at the centre bar location. Hence, they had different values for the two measures. The equivalent crack width approach as used by Vidal et al. [5.5] and Khan et al. [5.6] was adopted in this study. In this approach, two different measurements were used to obtain an equivalent crack width, which was related to the degree of corrosion of the main reinforcing bar. Previous researchers used different approaches for the quantification of corrosion-induced cracks. Coronelli et al. [5.7] used maximum crack width when the comparison was made between the experimental results and FEM modeling on the influence of corrosion on cover cracking, whereas Zhao et al. [5.8] used the sum of the surface cracks from two different locations for a similar comparison. Therefore, to obtain a clear interpretation of the crack width measure to be used, a single-crack specimen was compared with a similar specimen that

had “two cracks,” as tabulated in Table 5.6. As for the two crack specimens, when the crack was quantified by  $w_{cr,max}$  (the maximum crack from two different sides of crack location), the value was lower than that of the actual crack in the single-crack specimens. Larger values of  $w_{cr,tot}$  correspond to a higher level of corrosion in the main reinforcing bars, whereas an opposite trend is observed for  $w_{cr,max}$ . However, the results in Table 5.7 are far from conclusive because the comparison was made for specimens with different impressed currents.

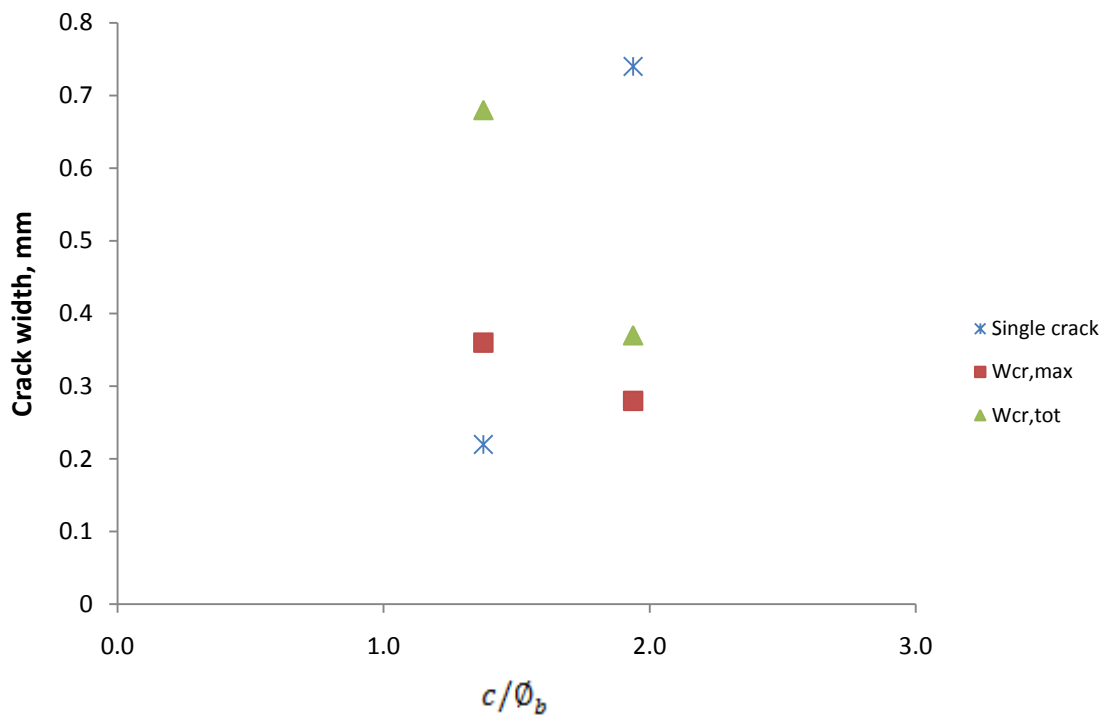
Bar ID	Crack width (mm)		Corrosion level (%)	$w_{cr,tot}$	$w_{cr,max}$
	Surface	Side			
10/1.6/F/TC/2	0.17	0.19	11.70	0.36	0.19
10/1.6/S/TC/2	None	0.30	5.43	0.30	0.30
Difference (%)			54.00	16.00	37.00
16/1.6/F/TC/2	None	0.47	7.89	0.47	0.47
16/1.6/S/TC/2	0.31	0.37	8.53	0.68	0.37
Difference (%)			8.00	31.00	21.00
16/1/F/TC/2	None	0.52	7.90	0.52	0.52
16/1/S/TC/2	0.13	0.14	6.62	0.27	0.14
Difference (%)			16.00	48.00	73.00

Table 5.7: Comparison between single crack and adjacent surface cracks

Further analysis was conducted as illustrated in Figure 5.12:  $w_{cr,max}$  and  $w_{cr,tot}$  for double-face crack specimens were plotted versus the  $c/\phi_b$  ratio and compared with the crack width in single-crack specimens for a top-cast and bottom cast corner bar location. For a given section loss, values of  $w_{cr,max}$  for the double-face crack specimens are lower than the crack widths observed in the single-crack specimens except of the bottom-cast bar with  $c/\phi_b$  ratio of 1.6 . In the first case, the values of  $w_{cr,tot}$  are closer to the single-crack width. Based on these observations, it can be concluded that the crack width for a double-face crack specimens to be better represented by  $w_{cr,tot}$  than by  $w_{cr,max}$ . Thus, further in this study,  $w_{cr,tot}$  is used as a crack measurement for double-face crack specimens.



a) Top-cast bar

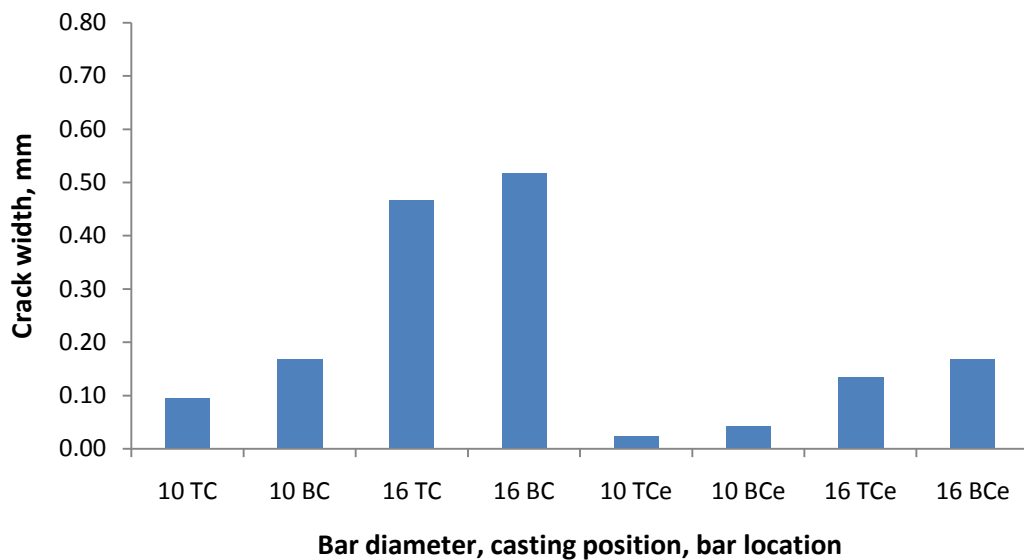


b) Bottom-cast bar

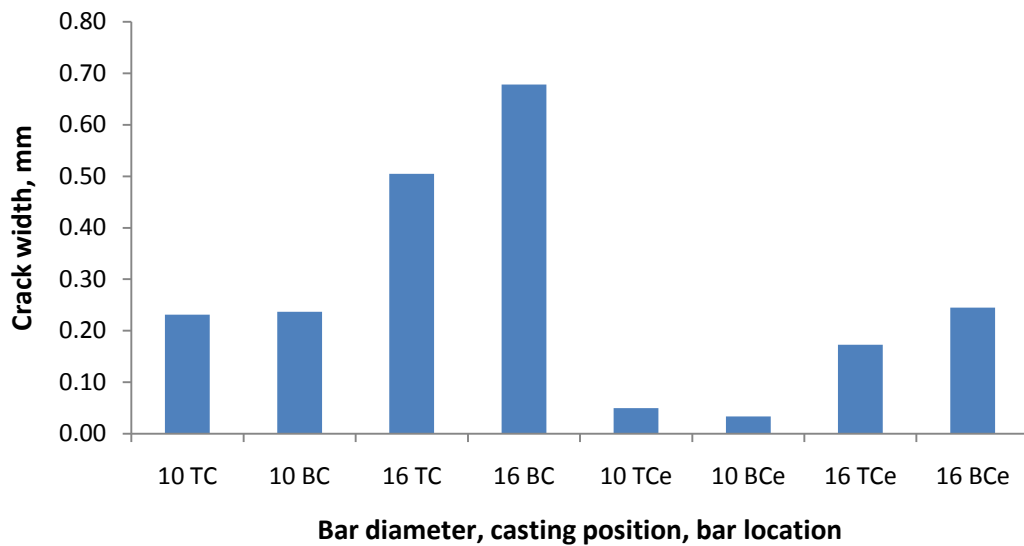
Figure 5.12: Comparison of  $w_{cr,max}$  and  $w_{cr,tot}$  with the crack width in single crack specimens

### 5.3.3.2.2 Influence of casting position on crack width

The average crack width along corroded reinforcing bar is plotted in Figures 5.13(a) and (b) for different casting batches. The plots show that the crack widths for the bottom-cast bars were wider than those for the top-cast bars, which occurred because of the different levels of the concrete compaction at these two positions. The top-cast bar was classified as a “poor” casting position by EN 1992-1-1:2004 [5.9] due to the plastic settlement of concrete, leading to poor compaction and voids underneath the bar [5.1]. Similar results were reported by Rodrigues et al. [5.10] and Tang [5.11] in their experimental works with and without link reinforcing bars. For the two different bar diameters used in this study, the specimens reinforced with 16 mm diameter bars had higher crack widths than the specimens with 10 mm diameter bars, whereas the corner crack width was wider than that of the centre crack. These trends are consistent for both casting batches.



a) First batch



b) Second batch

Figure 5.13: Surface crack width for different batches (T = top-cast, B = bottom-cast, C = corner bar location, Ce = centre bar location)

### 5.3.3.2.3 Effects of corrosion measurement on crack width

Given that two different corrosion measurements (i.e., section loss and corrosion penetration) are used in this study, an analysis was conducted to determine relationships between these two parameters and the surface crack width. One point that is worth mentioning is that the same loss of the bar section for two different bar diameters produces two different corrosion penetrations. To this point, results for both bar diameters in the second-batch specimens have been grouped according to the bar locations. The second batch was selected due to a similar  $c/\phi_b$  ratio for both bar diameters. To ensure a fair comparison, the groups were arranged to have the same average  $c/\phi_b$  ratio, whereas other aspects such as impressed current and casting position within each group were also the same. Figure 5.14 clearly shows that the 16 mm diameter bar corresponds more to higher crack widths than the 10 mm diameter bar. The crack width for the 16 mm diameter bar is two times higher than that for the 10 mm diameter bar at the corner bar location, and this difference increases to five times for the centre bar location. A similar trend is observed for the corrosion penetration, which for the 16 mm diameter bars is 1.3 times higher than that for the 10 mm diameter bars for the corner location and 1.2 times higher for the centre location. The trend is different for the section loss, where higher

values are observed for the 10 mm diameter bars. The ratios of the values for the 16 mm diameter bars to those for the 10 mm diameter bars are almost 0.8 and 0.7 for the corner and centre locations, respectively, which suggests that the relationship between the level of corrosion and the crack width for different bar diameters is better presented in terms of the corrosion penetration than the section loss.

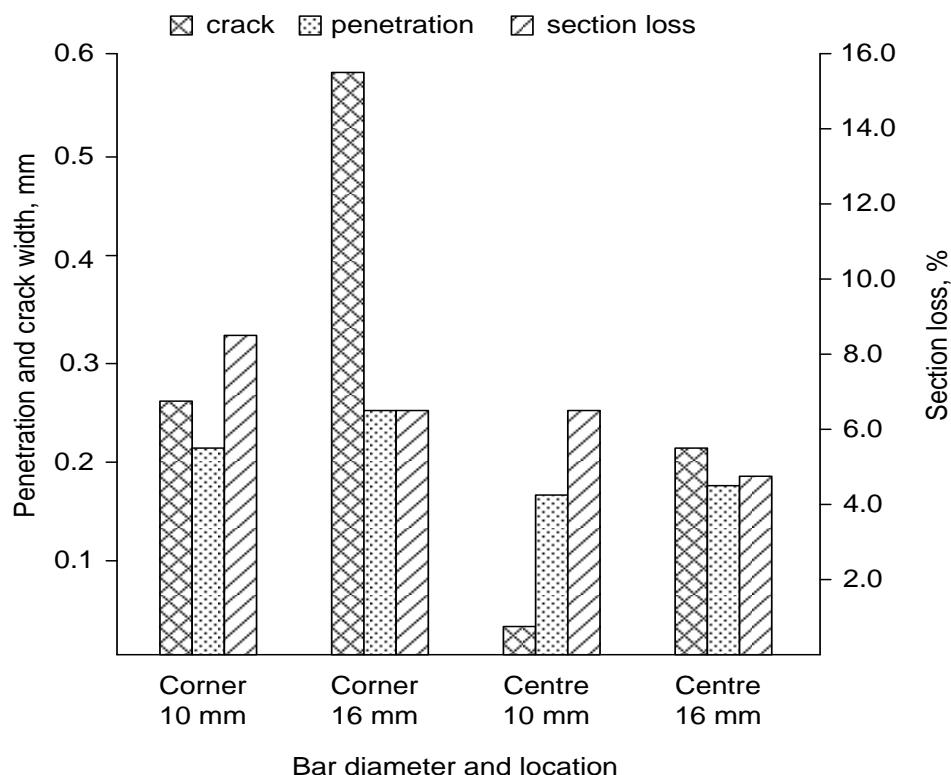
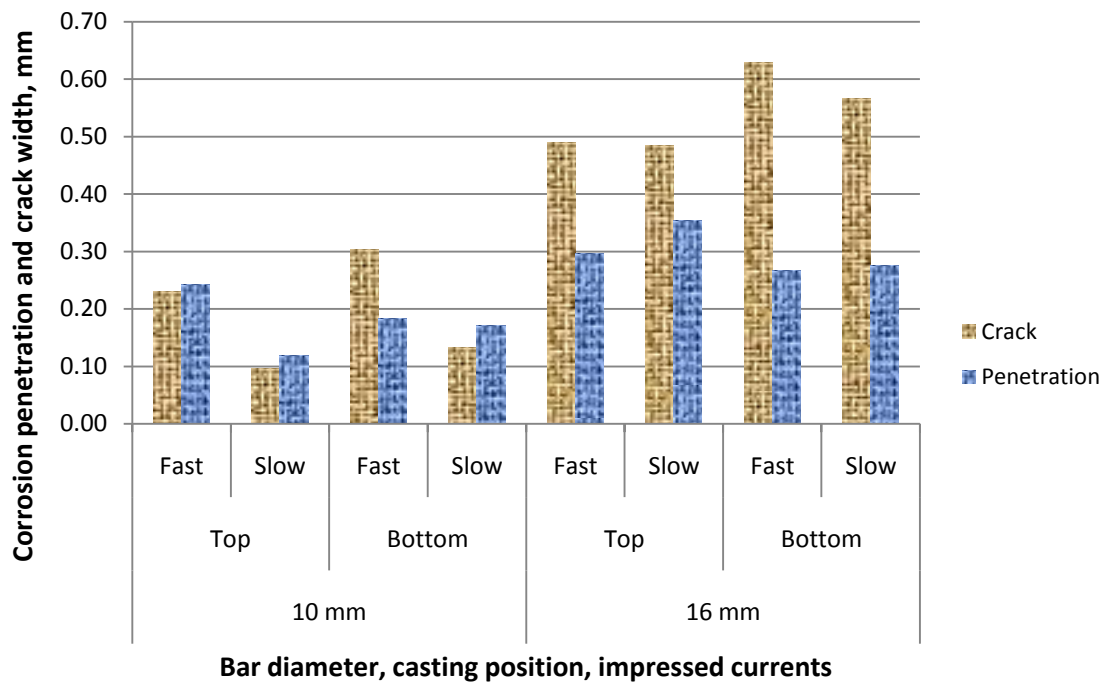


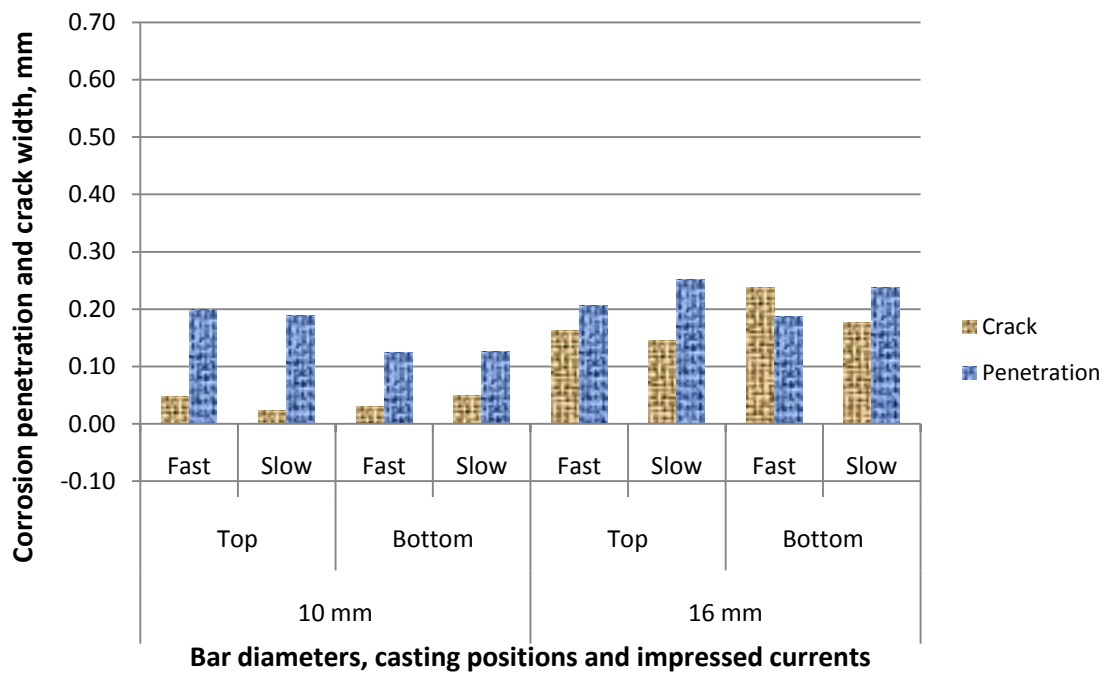
Figure 5.14: Mean crack width for two different corrosion measurements

#### 5.3.3.2.4 Influence of impressed current

The influence of the magnitude of impressed current on the surface crack width is shown in Figure 5.15, with the data presented separately for the two bar locations. It is clear from these two figures that the average crack width corresponding to the “fast” current, is higher than that for the “slow” current regardless of the bar location, casting position, or level of corrosion (the only exception is the bottom 10 mm diameter bar at the centre location). The differences vary from 1% to 58% and 10% to 52% for the corner and centre bar locations, respectively. The trend is similar to that observed by El Maaddawy and Soudki [5.12] in their experiments, which shows that the magnitude of impressed current significantly influences the final crack width in corroded specimens.



a) Corner bar location



b) Centre bar location

Figure 5.15: Crack width for different bar locations



### 5.3.4 Bond strength results

#### 5.3.4.1 Control uncorroded specimens

The values of the bond strength of uncorroded specimens given in Tables 5.1 and 5.2 are plotted in Figure 5.16. In general, bond strength increased with an increase in the cover-to-bar diameter ratio; centrally located bars developed higher bond strength than the corner ones; and the bond strength for the bottom-cast bars was higher than that for the top-cast bars.

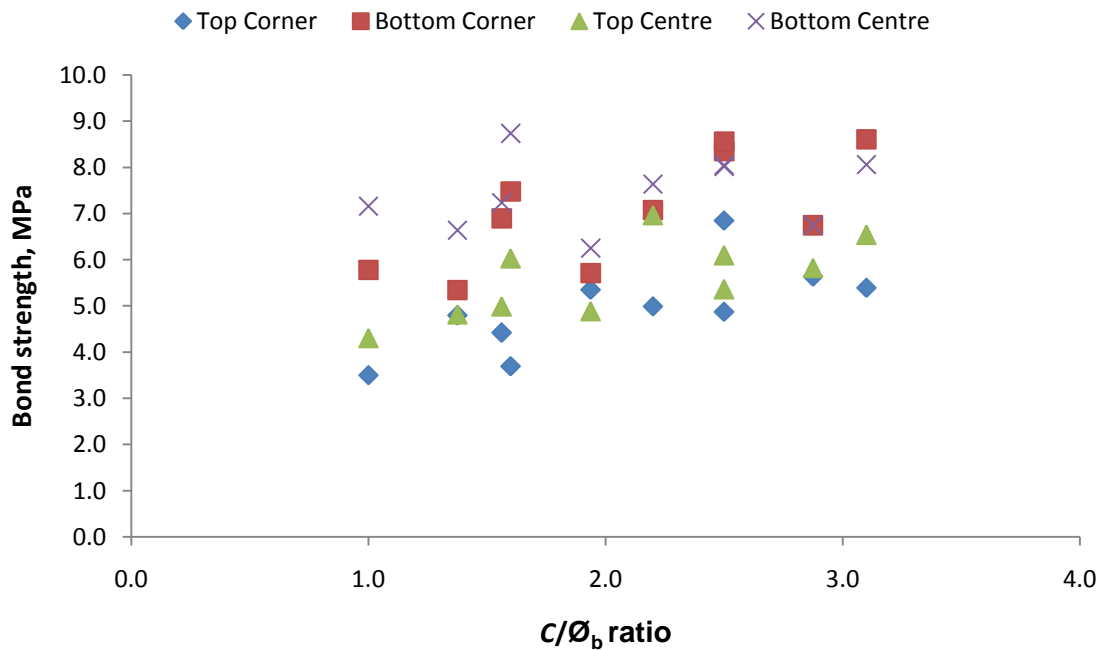


Figure 5.16: Influence of concrete cover on the control bond strength

These results were compared with bond strengths estimated by the modified bond model proposed by Canbay and Frosch [5.13] considering the cover thickness, main bar diameter, development length, and stirrup confinement. In this model, the bond strength is calculated based on the steel stress ( $f_s$ ) at splitting failure. For specimens confined by links,  $f_s$  can be determined using Equation 5.2

$$f_s = \frac{F_{splitting} + F_{stirrup}}{nA_b \tan \beta} \quad (\text{N/mm}^2) \quad (5.2)$$

where  $F_{splitting}$  is a splitting resistance (N),  $F_{stirrup}$  is the stirrup resistance (N),  $n$  is the number of bars being developed,  $A_b$  is the bar cross-sectional area (mm<sup>2</sup>), and  $\beta$  is the resultant force angle.

Given that only a single bar is considered,  $F_{splitting-side}$ ,  $F_{splitting-face}$ , and  $F_{stirrup}$  can be determined as follows [5.13]:

$$F_{splitting-side} = l_s^* (2c_{so}^*) 0.5\sqrt{f_c} \quad (5.3)$$

$$F_{splitting-face} = l_s^* \left[ 2c_b^* \left( 0.1 \frac{c_{so}}{c_b} + 0.9 \right) \right] 0.5\sqrt{f_c} \quad (5.4)$$

$$F_{stirrup} = N_{st} A_{st} \sigma_{st} \quad (5.5)$$

where  $l_s^*$  is the effective development length,  $c_{so}$  is the side cover,  $c_{so}^*$  is the effective side cover,  $f_c$  is the compressive strength of concrete cylinder,  $c_b$  is the clear face cover,  $c_b^*$  is the effective face cover,  $N_{st}$  is the number of stirrups within the development length,  $A_{st}$  is the cross-sectional area of stirrups, and  $\sigma_{st}$  is the stress in stirrups. Given that no data were available for the stress in stirrup in this study,  $\sigma_{st} = 62$  N/mm<sup>2</sup> was adopted as previously suggested by Canbay and Frosch [5.13].

For the corner bar location,  $c_{so} = c_b$  [Figure 5.17(a)] and  $F_{splitting-face} = F_{splitting-side}$ . For the centre bar location, the clear side cover,  $c_{so} = \frac{b - \phi_b}{2}$  [Figure 5.17(b)], where  $b$  is the width of the specimen, and  $\phi_b$  is the diameter of the main reinforcing bar.

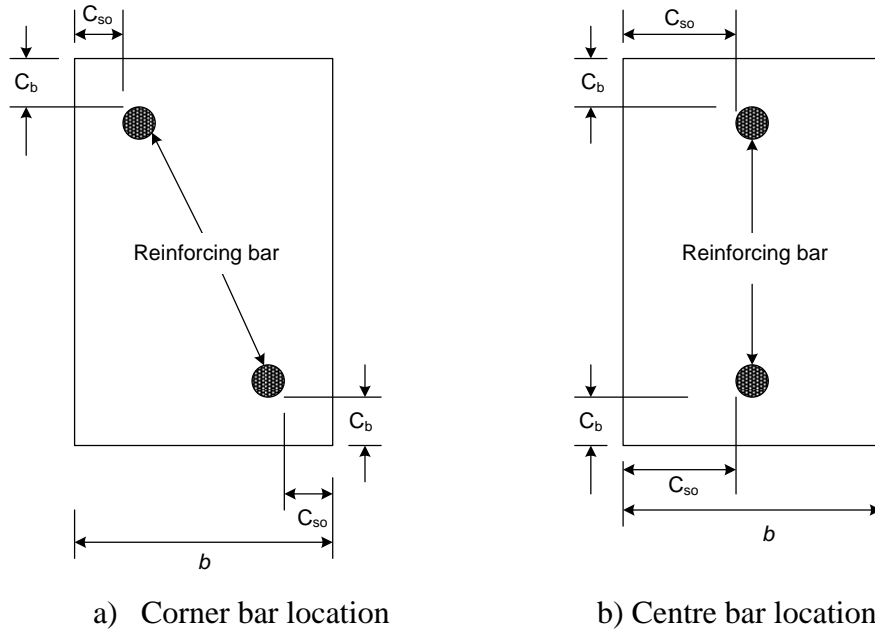


Figure 5.17: Clear concrete cover for different bar locations

The values for  $l_s^*$  and  $c_{so}^*$  are calculated based on the following equations [5.13]:

$$c_{so}^* = c_b^* = c \frac{0.77}{\sqrt{c/\phi_b}} \quad (\text{for corner bar location}) \quad (5.6a)$$

$$c_{so}^* = c_{so} \frac{0.77}{\sqrt{c/\phi_b}} \quad (\text{for centre bar location}) \quad (5.6b)$$

$$\text{where } \frac{0.77}{\sqrt{c/\phi_b}} \leq 1.0$$

$$l_s^* = l_d \frac{9.5}{(\sqrt{l_d/\phi_b})^4 \sqrt{f_{c,m}}} \quad (5.7)$$

where  $c$  is the main bar cover,  $\phi_b$  is the main bar diameter,  $l_d$  is the development length, and  $f_{c,m}$  is the mean cylinder compressive strength of concrete. In the above equations, the dimensions are in mm, and the forces are in N.

The steel stress is converted to bond strength,  $f_b$ , as follows:

$$f_b = \frac{f_s \phi_b}{4l_d} \quad (5.8)$$

The comparison between experimental results and analytical model is shown in Figure 5.18. In this comparison, the  $\beta$  value was considered equal to 20 degrees based on the value that was assumed previously by Canbay and Frosch [5.13]. A difference in this value will affect the bond strength; specifically, a greater  $\beta$  value will decrease the bond strength.

A linear increase in the bond strength with an increase in the cover-to-diameter ratio can be seen for both theoretical and experimental data. Furthermore, the casting positions and the bar locations significantly influence the bond strength. In particular, the bond strength of the bottom-cast bars is higher than that of the bars at the top-cast position. Bond strength is also higher for the bars at the central location compared with that of the bars at the corner location. Notably, the bond strength calculated from the Canbay and Frosch model (Equation 5.2) considered the bar location in the calculation as in Equation 5.3 and 5.4. Therefore, we can see the effects of the bar location on the bond strength both in theoretical and experimental results. For the corner bar location, the model provides a good estimation of bond strength for bottom cast including the influence of cover-to-diameter ratio on bond strength criteria. However, a similar trend is not observed for the

bottom-cast centre bar location, for which statistical analysis of the experimental data does not indicate a linear relationship between bond strength and cover-to-diameter ratio due to a very low  $R^2$  value.

On the basis of the regression analysis, the bond strengths that best fit the data for the corner bar location are as follows:

$$f_b = 0.9 \frac{c}{\phi_b} + 3.2 \quad \text{for top-cast bar} \quad (5.9)$$

$$f_b = 1.6 \frac{c}{\phi_b} + 3.9 \quad \text{for bottom-cast bar} \quad (5.10)$$

whereas for centre bar location

$$f_b = 0.9 \frac{c}{\phi_b} + 3.7 \quad \text{for top-cast bar} \quad (5.11)$$

$$f_b = 0.1 \frac{c}{\phi_b} + 6.8 \quad \text{for bottom-cast bar} \quad (5.12)$$

Table 5.8 summarises the ratio of measured to predicted bond strength based on the Canbay and Frosch model. In this analysis, only specimens that failed due to splitting were considered. For both bar locations, the predicted bond strength for top-cast bars is higher than that obtained in the tests (i.e., the average ratio is less than unity). This trend is expected because the Canbay and Frosch model was derived based on experimental results for bottom-cast bars, which overestimates the bond strength for the top-cast bars. The opposite trend is observed for the bottom-cast bars where the ratio is higher than 1, which shows that the model underestimates the experimental bond strength. This may occur due to the difference in specimen type and testing setup since a full-sized beam test was used previously, while in this study beam end-type specimens were used. However, the coefficient of variation of the measured to the predicted bond strength ratio for both bar diameters is still small, which suggests that the model gives a reasonably good estimation of bond strength in the test specimens. No comparison is made for the bottom-cast 10 mm diameter bars at the centre location due to the yielding failure type of all such specimens.

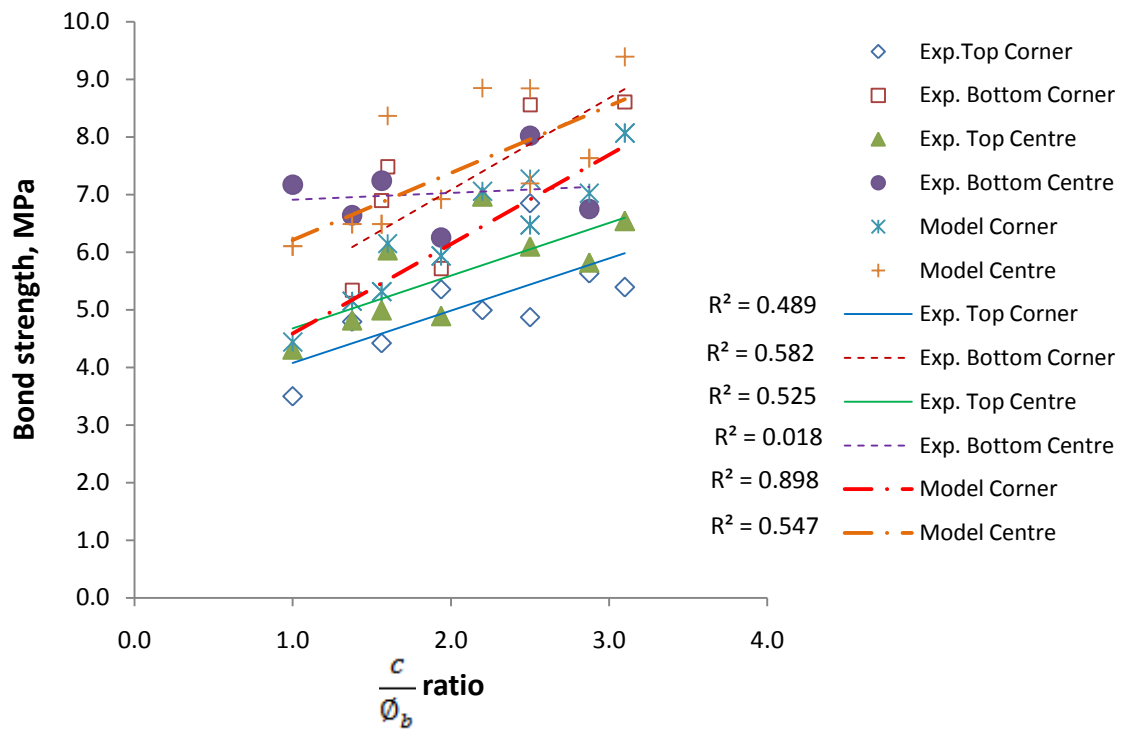


Figure 5.18: Bond strength from different  $c/\phi_b$  ratios

Bar diameter (mm)	Bar location	Casting position	Average	Standard deviation	CoV
10	Corner	Top	0.68	0.07	0.10
		Bottom	1.14	0.17	0.15
	Centre	Top	0.72	0.20	0.27
		Bottom	-	-	-
16	Corner	Top	0.89	0.03	0.03
		Bottom	1.16	0.17	0.14
	Centre	Top	0.74	0.16	0.22
		Bottom	1.04	0.12	0.12

Table 5.8: Summary of the measured to the predicted bond strength ratio

#### 5.3.4.2 Corroded specimens

Many corrosion parameters influence the reduction of bond strength in reinforced concrete members, according to previous research as described in Section 2.4.2. This section will discuss the influence of corrosion parameters used in this study on the bond strength.

#### 5.3.4.2.1 Bond failure mode

The bond tests on corroded specimens were conducted several days after completing corrosion conditioning, which would have been a sufficient time for any influence of the electrical current on the concrete immediately surrounding the bars to have dissipated, as discussed by Buenfeld and Broomfield [5.14]. Failure modes are shown in Figures 5.19 and 5.20 for the central and corner bar locations, respectively. The splitting-type failure was observed for both bar diameters, similar to the control specimens. However, some of the corroded specimens failed in the pullout mode as explained previously in Section 5.2.4. The failure modes for each bar were presented previously in Tables 5.3 and 5.4. For the splitting-type failure, existing corrosion cracks widened given the splitting in specimens with cracks, whereas for specimens without cracks, splitting cracks developed along the reinforcing bar during the loading test. Opening of the cracks reduced the confinement provided by the concrete cover and eventually resulted in splitting failure. However, several specimens reinforced with 10 mm diameter bars failed due to yielding of the bar. Thus, the bond strength calculated from the failure loads measured in these tests was considered a lower bound to the true strength.



Figure 5.19: Splitting failure on centre bar location



Figure 5.20: Splitting failure on corner bar location

#### **5.3.4.2.2 Bond strength**

For the control uncorroded specimens, the difference between the maximum and the minimum bond strength for the 10 mm and 16 mm diameter bars was 57% and 59%, respectively. For the corroded specimens, the difference was reduced to 39% for both bar diameters, which suggests that corrosion reduces the difference between the bond conditions in RC beams with similar dimensions and concrete properties.

The bond strengths of corroded specimens are presented in Tables 5.3 and 5.4 for the first and second batches, respectively. These strengths are plotted in Figure 5.21 versus the cover-to-bar-diameter ratio for the top-cast and the bottom-cast bars at both center and corner locations. In general, the bond strength of corroded specimens is still higher for the bottom-cast bars compared with that for the top cast at both locations. On the basis of linear regression analysis, no clear evidence of linear correlation was found between the bond strength and the cover-to-bar-diameter ratio for the corroded specimens. As can be seen, the analysis yielded very low  $R^2$  values, except for the top corner location. Even in this case,  $R^2$  is less than 0.3. The bond strength of corroded specimens ranges from 4 MPa to 9 MPa, and the values are still within the range of that in the control uncorroded

specimens (Tables 5.1 and 5.2), which indicates that for the corrosion levels considered in this experimental study, the bond strength in the specimens was not significantly affected by the presence of corrosion.

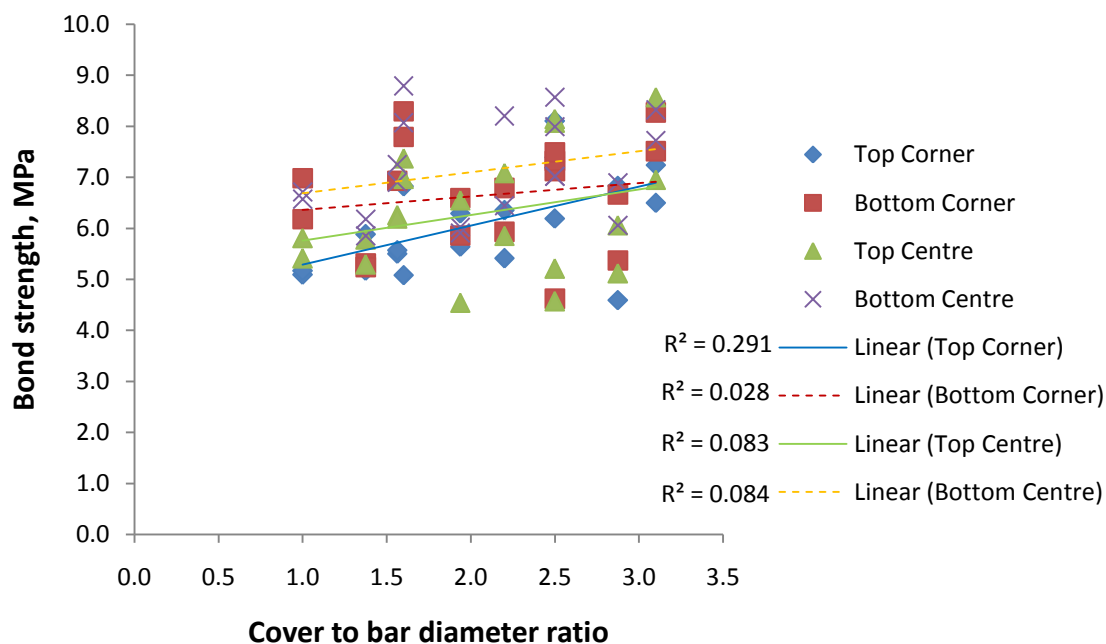


Figure 5.21: Corroded bond strength

Further analysis was conducted on the bond strength ratio between the two batches (separately for “fast” and “slow” impressed currents). Results are shown in Table 5.9. The ratio was calculated by dividing the bond strength of a specimen from the first batch to that of the specimen with similar identification from the second batch. The average bond strength ratios are similar for “fast” and “slow” currents for both bar diameters, which suggests that the bond strength values obtained for the two batches are consistent. The highest variation is observed for the 10 mm diameter bars with “slow” current that might result from the significant differences between theoretical and actual mass losses discussed previously in Section 5.3.1.

Bar diameter (mm)	10		16	
	“fast”	“slow”	“fast”	“slow”
Average	0.92	0.98	0.93	1.00
Standard deviation	0.08	0.17	0.15	0.15
Coefficient of variation	0.09	0.17	0.16	0.15

Table 5.9: First-batch to second-batch bond strength ratio



### 5.3.4.2.3 Effects of width of corrosion-induced crack on bond strength

The effect of corrosion-induced cracking on bond strength is presented in Figure 5.22 for 10 and 16 mm diameter bars for both casting positions. In general, the bond strength of the 10 mm diameter bars decreases with an increase in the corrosion-induced crack width. The trend is much less evident for the 16 mm diameter bars. This observation is confirmed by results of linear regression analysis that was conducted to check the correlation between the bond strength and the crack width based on the bar diameter and casting position. On the basis of the  $R^2$  values, a linear correlation between the bond strength and the corrosion-induced crack width is only evident for 10 mm diameter bottom-cast bars. For the rest of the cases, especially for the 16 mm diameter bars, the values of  $R^2$  are small, i.e., no sufficient evidence of a linear relationship between the bond strength and the corrosion-induced crack width is found, which indicates that the corrosion crack width does not strongly correlate with the final bond strength of corroded reinforcement, at least in the RC specimens tested in this study.

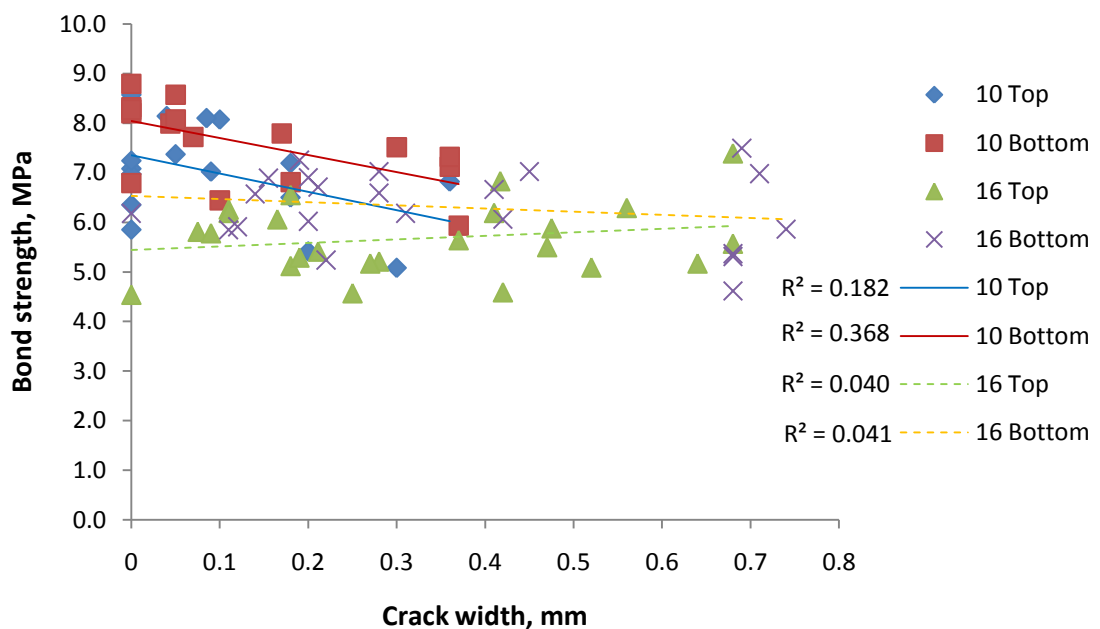


Figure 5.22: Influence of corrosion-induced crack width on bond strength

#### 5.3.4.2.4 Bond strength for different corrosion levels

The values of bond strength in the corroded specimens versus different corrosion measurements, namely, the corrosion penetration and the section loss, are presented in Figures 5.23 and 5.24, respectively. Linear regression analyses were carried out separately for the results obtained for two different impressed current densities (“fast” and “slow”) and casting positions (top and bottom) used in this study. The obtained regression lines indicate a trend that the specimens with higher corrosion penetration had lower bond strength than the specimens with lower corrosion penetration. This trend can be observed for both casting positions and impressed current densities. The results also indicate a linear correlation between the bond strength and the corrosion penetration for the bottom-cast bars for both “fast” and “slow” currents. However, when the bond strength is plotted against the section loss (Figure 5.24), the opposite trend is observed for top-cast bars impressed with “fast” current, i.e., their bond strength increases with an increase in the section loss. Moreover, according to the obtained values of  $R^2$ , the linear correlation between the bond strength and the section loss is weaker than that between the bond strength and the corrosion penetration. Hence, the change of the bond strength due to corrosion can be better described in terms of the corrosion penetration than of the section loss.

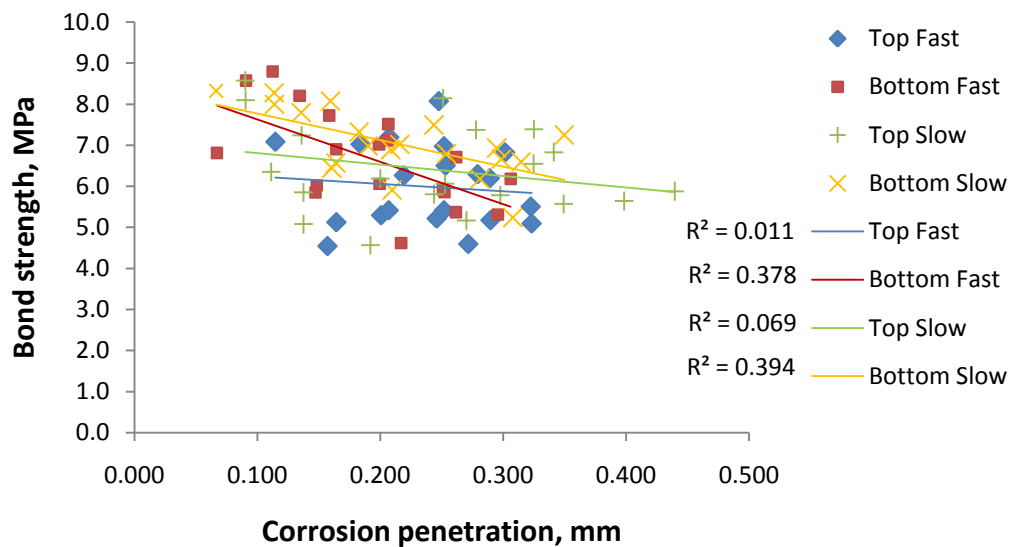


Figure 5.23: Corroded bond strength versus corrosion penetration

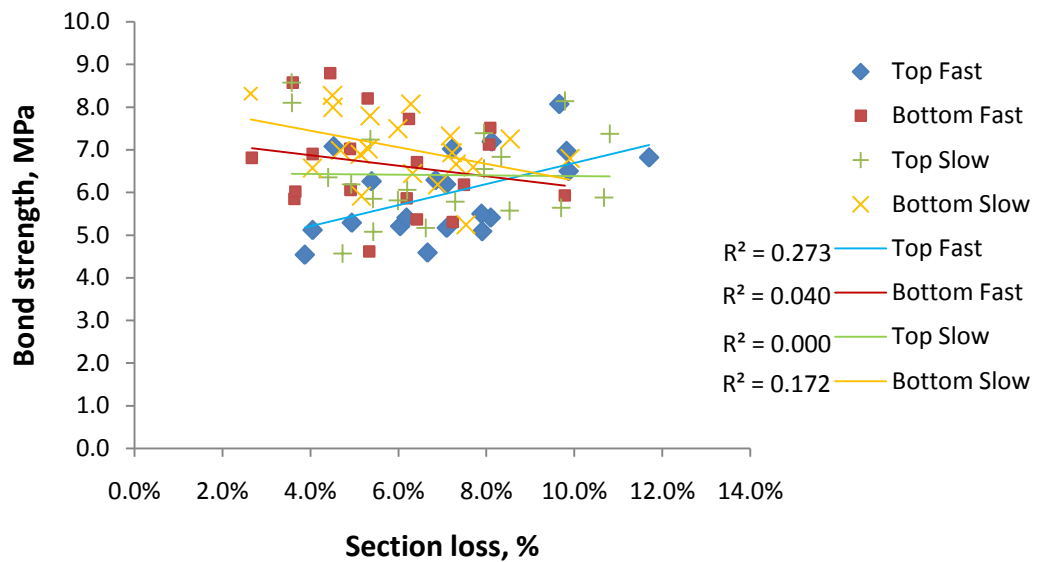


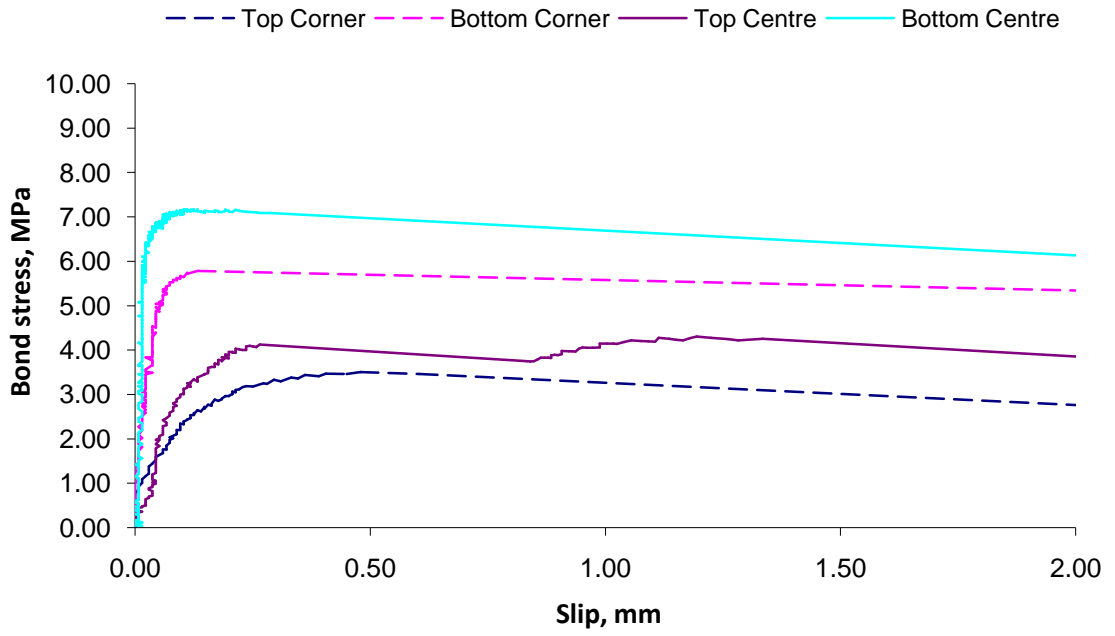
Figure 5.24: Corroded bond strength versus section loss

#### 5.3.4.2.5 Bond-slip behaviour

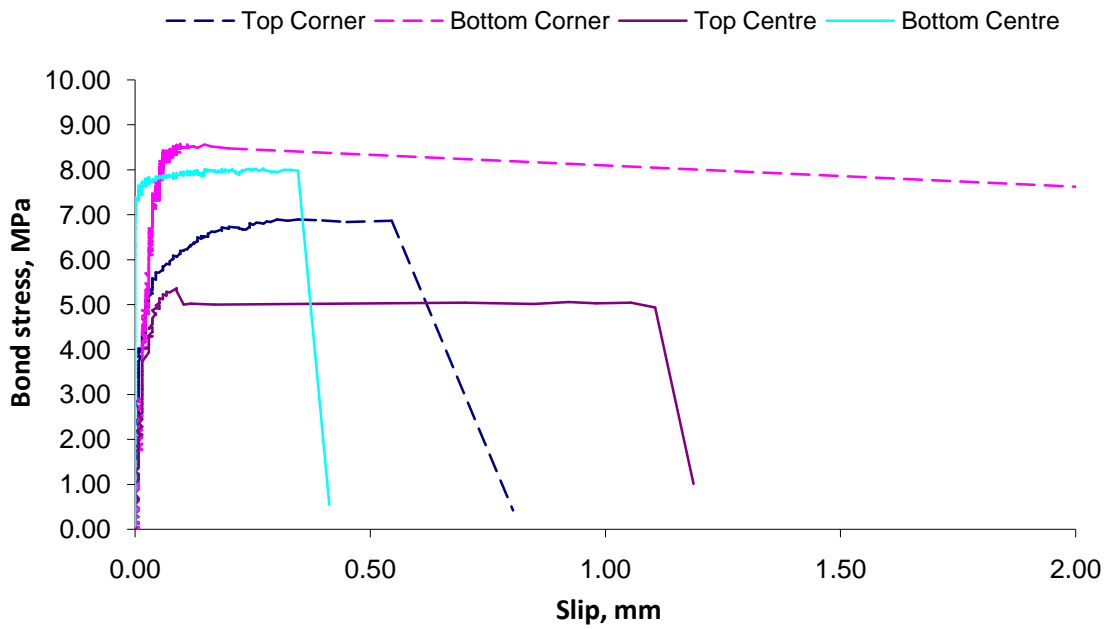
The bond–slip diagrams for the control specimens reinforced with 10 and 16 mm diameter bars are plotted in Figures 5.25 and 5.26 for different casting positions and bar locations. For both bar diameters and locations, the bond stiffness at the steel–concrete interface for the top-cast bars is lower than that for the bottom-cast bars because of different concrete compactions. The compaction for the top-cast bar is worse than for the bottom bar, and voids are located underneath the bar, thus reducing the bond stiffness between the steel and the concrete interface. A similar trend is observed for both  $c/\phi_b$  ratios.

However, for the corroded specimens, as depicted in Figures 5.27 and 5.28 for 10 and 16 mm diameter bars, respectively, in the presence of corrosion, the differences in the bond stiffness for different bar locations are much smaller than those for uncorroded bars. Furthermore, centre bar location specimens with the higher cover-to-bar-diameter ratio show a sudden loss of bond resistance, thus lowering the bond slip. Therefore, it can be concluded that corrosion changes the steel–concrete interface, thus influencing the stress–slip bond behavior. Some of the specimens reinforced with 10 mm diameter bars failed due to yielding of the main reinforcing bar, which resulted in a higher slip compared with the bond failure mode.

Figure 5.29 shows the comparison between relative bond end slip with corrosion penetration for different bar diameters and casting positions on both casting batches used in this study. Relative bond end slip is calculated by dividing the average corroded end slip to that of the corresponding average control end slip. From that figure, lower relative bond end slip is observed on the top cast bars than the bottom cast bars even with higher corrosion penetration as in 10 mm bars in the first batch specimens. This trend might suggest that the presence of corrosion products around the steel-concrete interface had changed its surrounding confinement. The rust products generated by the corrosion had filled the voids underneath the top-cast bars, which resulted in a firmer contact between the bars and the concrete and an increase in the bond stiffness. The bottom-cast bars had initially been surrounded by less-porous concrete than the top ones. Hence, the rust probably induced higher pressure on the concrete surrounding these bars, thereby loosening the grip of the concrete on the bars and increasing the slip. However, the similar trend is not observed on the second batch specimens with 10 mm reinforcing bars due to yield type bond failure on most of the bar in this group, thus influence the average slip value.



(a) 1.0  $c/\phi_b$  ratio



(b) 2.5  $c/\phi_b$  ratio

Figure 5.25: Bond stress-slip diagram for 16 mm diameter control specimens

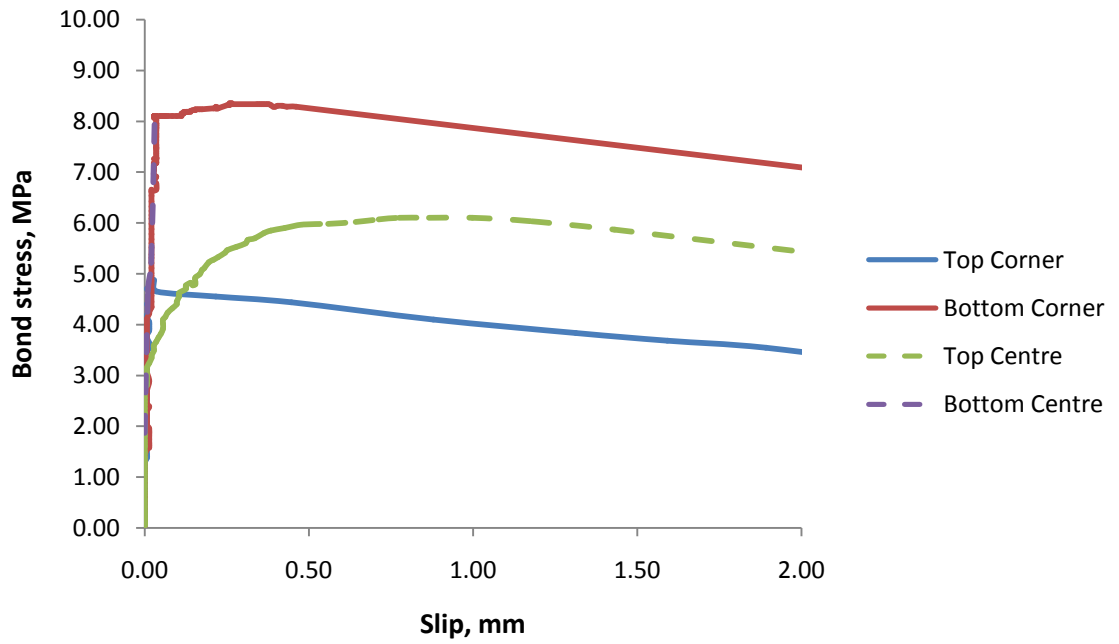
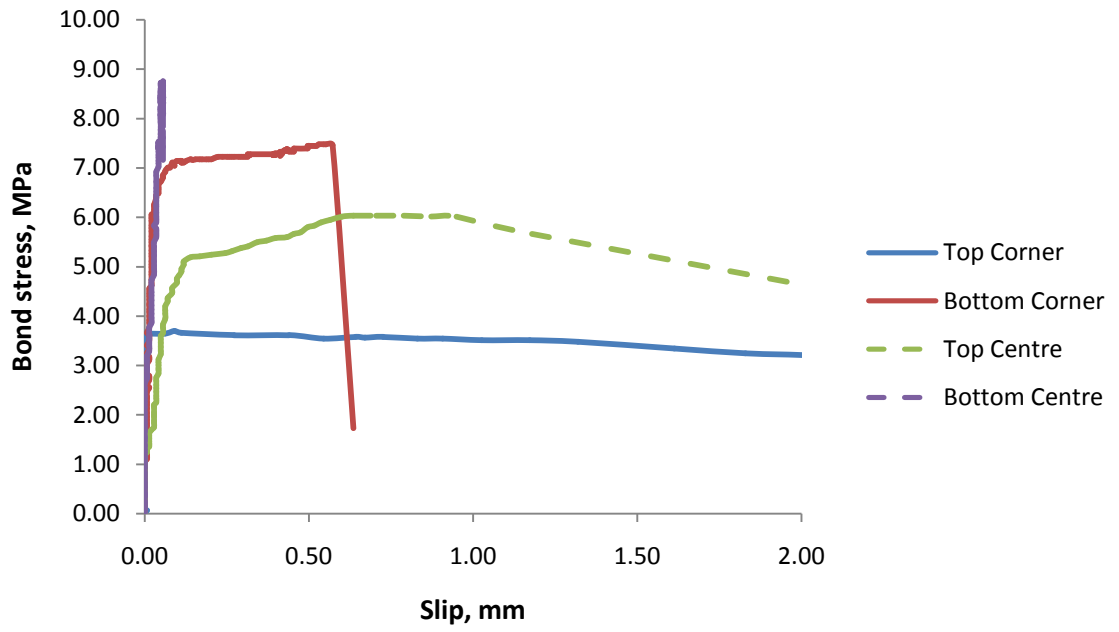
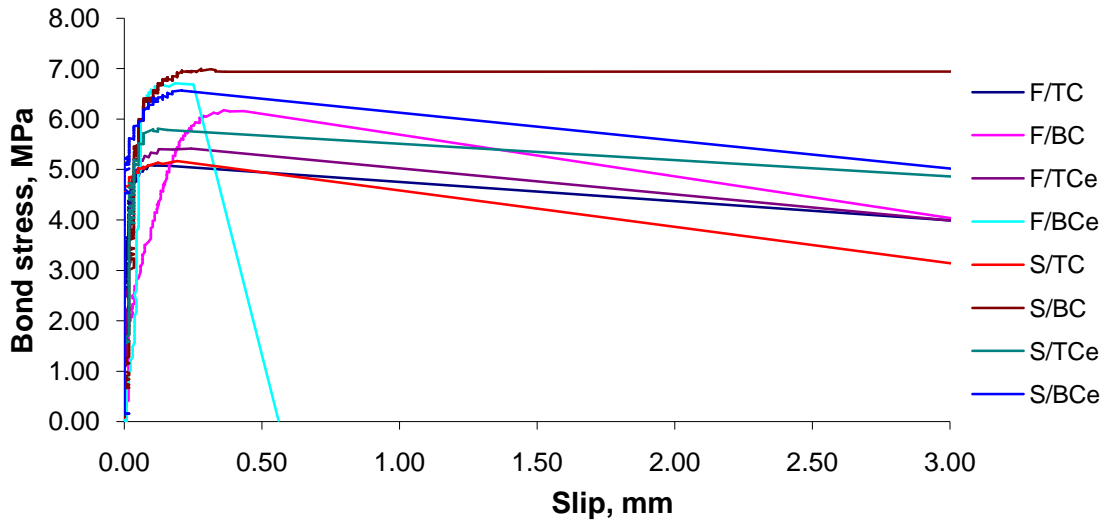
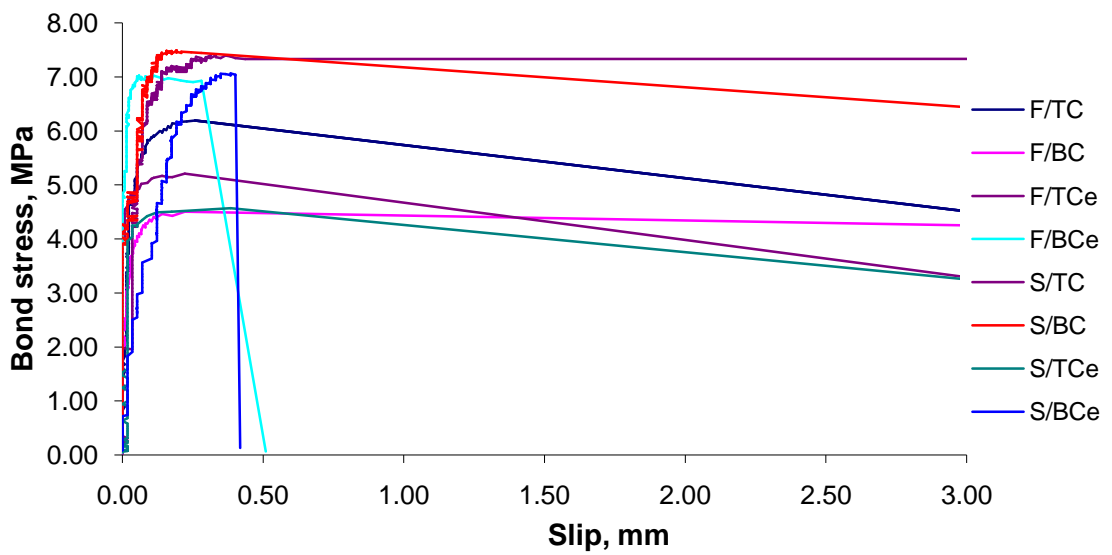


Figure 5.26: Bond stress-slip diagram for 10 mm diameter control specimen

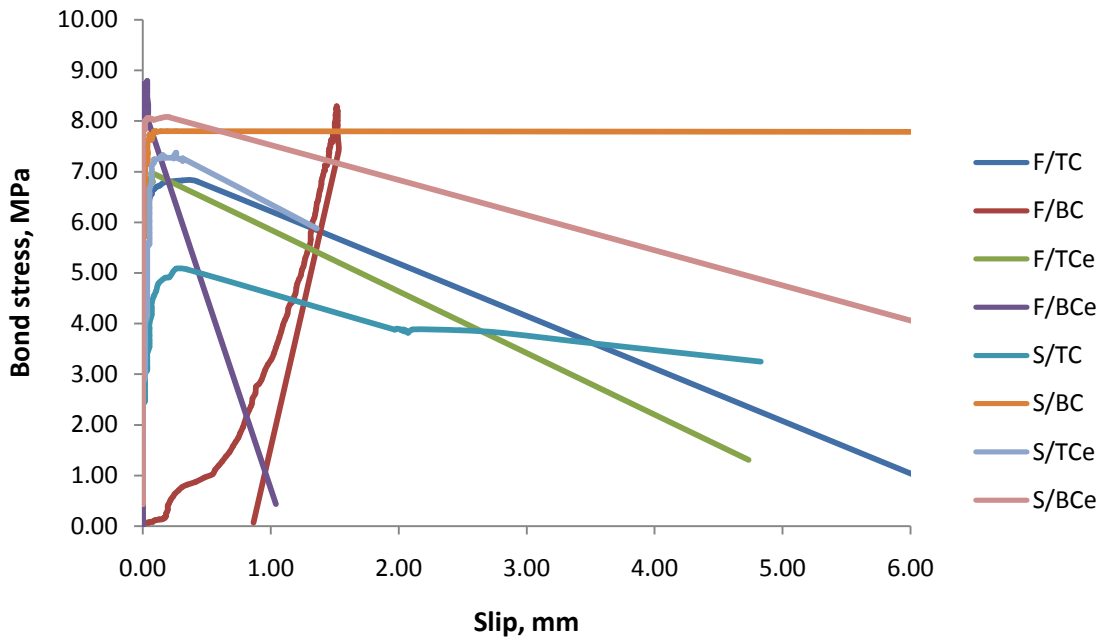


(a) 1.0  $c/\phi_b$  ratio

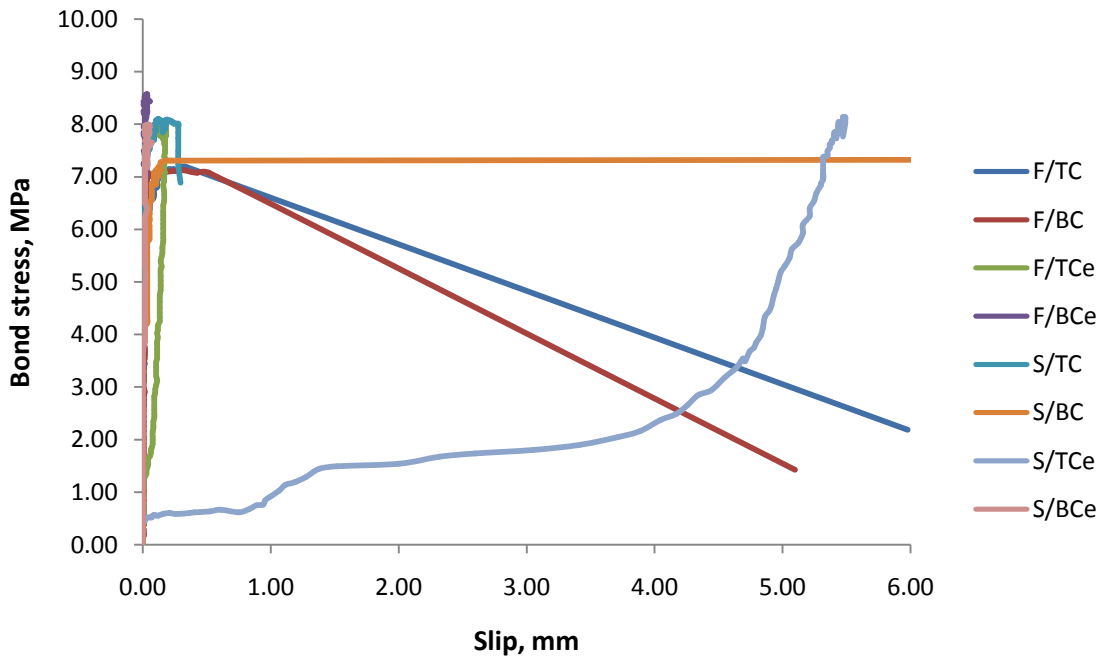


(b) 2.5  $c/\phi_b$  ratio

Figure 5.27: Bond stress-slip diagram for 16 mm diameter corroded specimens



(a) 1.6  $c/\phi_b$  ratio



(b) 2.5  $c/\phi_b$  ratio

Figure 5.28: Bond stress-slip diagram for 10 mm diameter corroded specimens



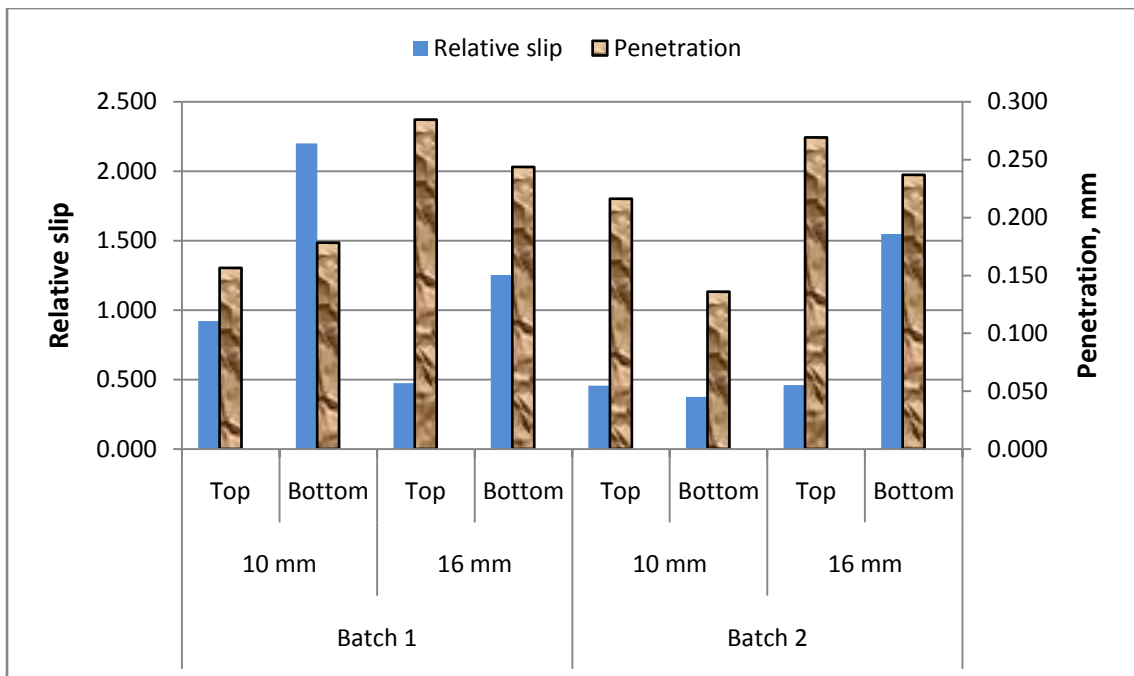


Figure 5.29: Relative bond slip versus corrosion penetrations

### 5.3.5 Influence of corrosion parameters on residual bond strength

Previous sections have discussed the influence of corrosion parameters on bond strength. However, the parameter that has the most influence on the bond strength reduction is still unclear. Up to now, different researchers have used different approaches to quantify the influence of corrosion on residual bond strength, i.e., the bond strength between concrete and corroded reinforcing bars.

In this section, the effects of corrosion on the residual bond strength are investigated. The main corrosion parameters used in this study will be compared with the residual bond strength, which is characterised by the bond strength ratio,  $f_{b,r}$ . The latter is determined as the ratio of the bond strength of a corroded specimen to that of the corresponding uncorroded control specimen. Thus, if the value of  $f_{b,r}$  is less than unity, then the bond strength has been reduced by corrosion.

Figure 5.30 shows the average  $f_{b,r}$  values for different bar diameters, casting positions, bar locations, and impressed current densities. Clear observations from this figure are as follows: (i) the bottom-cast bars have lower  $f_{b,r}$  values than the top-cast bars, with the majority of the latter values lower than 1; (ii) most of the specimens impressed with

“slow” current have higher  $f_{b,r}$  values than the specimens impressed with “fast” current with the differences less than 10%; (iii) most of the  $f_{b,r}$  values for the specimens with 10 mm diameter reinforcing bars are higher than those for the specimens with 16 mm diameter reinforcing bars; and (iv) no significant influence of the bar location on the  $f_{b,r}$  value can be observed.

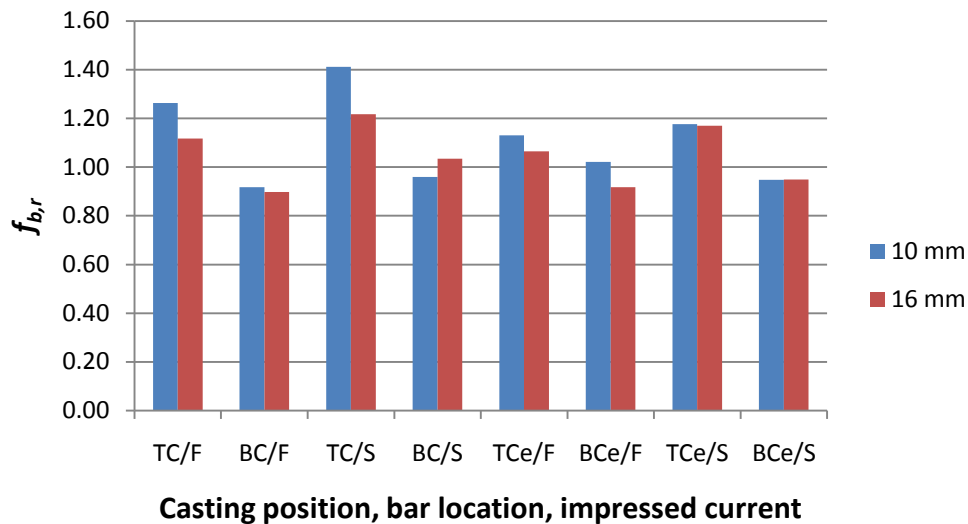


Figure 5.30: Average  $f_{b,r}$  value (note: T = top-cast, B = bottom-cast, C = corner bar location, Ce = centre bar location, F = “fast”, S = “slow”)

Further analysis was conducted to examine the influence of the corrosion parameters on the residual bond strength and determine which corrosion parameter correlated best with the residual bond strength. First, the average corrosion penetration and the section loss for different cover-to-bar-diameter ratios and bar diameters are compared with the average  $f_{b,r}$  value. As can be seen in Figure 5.31, although the average corrosion level, which is quantified either by the corrosion penetration or the section (mass) loss, is higher for the top-cast bars than for the bottom-cast bars, higher average  $f_{b,r}$  values for the top-cast position were also observed, which showed that the steel–concrete interface was crucial in determining the effect of corrosion on the bond strength. As discussed previously, the number of voids around the top-cast bars is larger than those around the bottom ones, which leads to lower values of the initial bond strength and higher corrosion losses. However, the reduction of the bond strength for the top bars is smaller than that for the bottom ones. In fact, in most cases (except of the 16 mm diameter bar and  $c/\phi_b = 2.5$ ), the residual bond strength even increases (i.e.,  $f_{b,r} > 1$ ) because more corrosion products are needed to fill the voids around the top-cast bars. While the corrosion products are

filling the voids, the confinement around the bars improves, thereby resulting in higher bond strength (see Section 2.4.2). Similar results are mainly observed for other  $c/\phi_b$  ratios as well (Figure 5.32).

With regard to the different  $c/\phi_b$  ratios, the  $f_{b,r}$  values for the two ratios are similar for the specimens with 10 mm diameter bars at the same casting positions. However, for the specimens with 16 mm diameter bars, these values are higher for the lower  $c/\phi_b$  ratio (Figure 5.31). Similar results are observed for other  $c/\phi_b$  ratios (Figure 5.32). Possible explanation is that the concrete compaction is higher for thicker covers; thus, fewer corrosion products are needed to cause the same degradation of bond for these covers compared with thinner ones.

Therefore, the influence of corrosion on the residual bond strength may be concluded to mainly depend on the casting position of the reinforcing bar, to a lesser degree on the thickness of the concrete cover (which influences the compaction level) and much less on the level of the corrosion itself, at least on the basis of the test results obtained in this study.

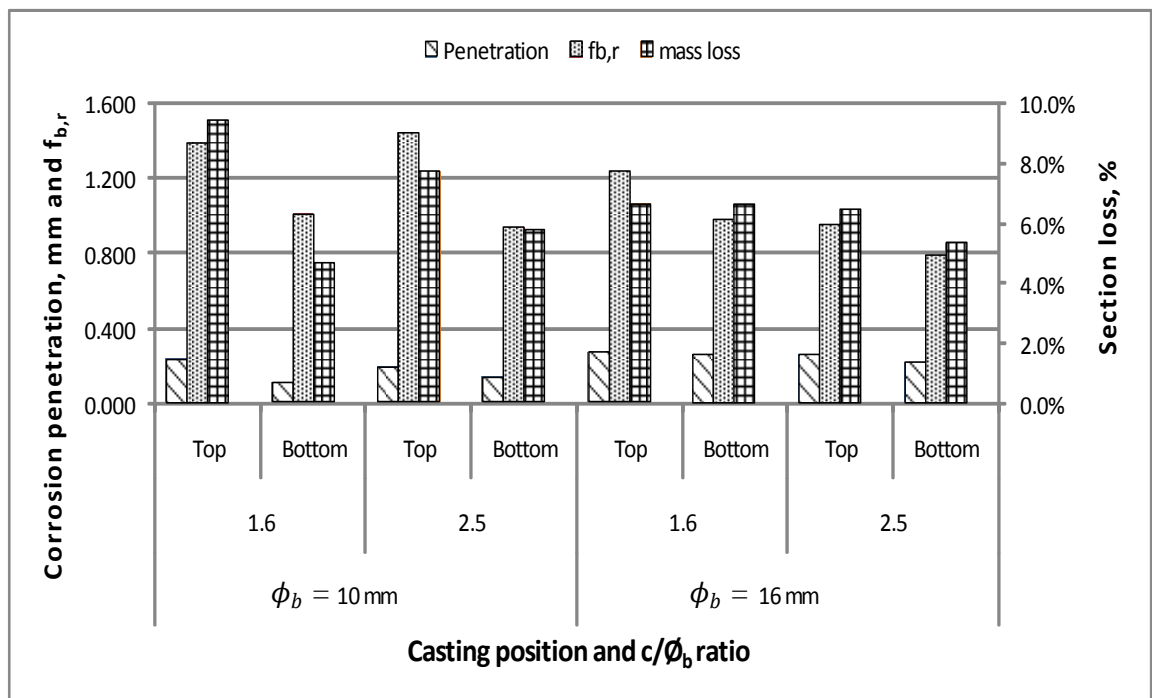


Figure 5.31: Average  $f_{b,r}$  for  $c/\phi_b$  ratio of 1.6 and 2.5

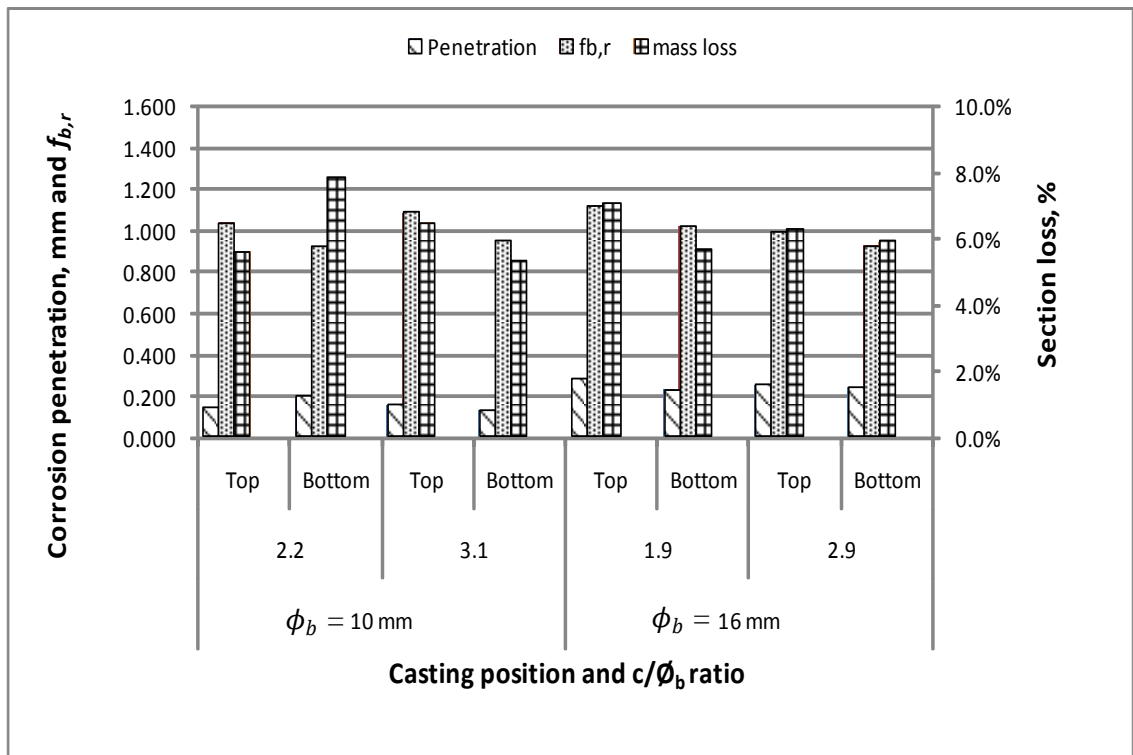


Figure 5.32: Average  $f_{b,r}$  for various  $c/\phi_b$  ratios

The second part of the analysis examines the influence of crack width on the  $f_{b,r}$  value, as shown in Figures 5.33 and 5.34. As can be seen, higher average widths of the cracks along the bottom-cast bars compared with those along the top-cast bars correspond to lower average  $f_{b,r}$  values for the bars at the bottom-cast position. This trend is consistent for both bar diameters (except for the 10 mm diameter bar with  $c/\phi_b$  ratio of 1.6). As discussed previously, the presence of corrosion-induced cracking reduced the confinement provided by the surrounding concrete to the reinforcing bars, thus reducing the bond strength. This phenomenon is more important for the bottom-cast bars because the degree of concrete compaction around these bars is higher than that around the top-cast bars. Therefore, on the basis of this observation, the crack width, especially along the bottom-cast bars, may be used as an indicator of the residual bond strength of corroded reinforcement.

Thus, the values of  $f_{b,r}$  were plotted against the widths of cracks along the bottom-cast bars to check if any correlation exists between these two parameters (Figure 5.35). Linear regression analysis shows a reasonably good correlation between the  $f_{b,r}$  values and the crack widths ( $w_{cr}$ ) with the  $R^2$  value slightly above 0.5. However, for the top-cast bars, no linear correlation is found between the crack width and the  $f_{b,r}$  value with the  $R^2$  value as

low as 0.01. The corresponding linear relationship between these two parameters for bottom-cast bars is as follows:

$$f_{b,r} = 1.0 - 0.344w_{cr} \quad (5.13)$$

This result also indicates that the residual bond strength should be similar or even higher to that of uncorroded bars at the same casting position when no corrosion-induced crack is observed on the surface of the concrete along these bars. This can be seen from the  $f_{b,r}$  values of close to 1 or even higher for the corroded specimens having no corrosion-induced crack as presented in Table 5.10.

Bar ID	Casting position	$\phi_b$ (mm)	Crack (mm)	$f_{b,r}$
10/2.5/S/Bce	Bottom	10	0	1.03
10/2.5/S/BC	Bottom	10	0	0.96
10/1.6/F/Bce	Bottom	10	0	1.06
10/1.6/S/BC	Bottom	10	0	0.96
10/2.5/S/Tce	Top	10	0	1.31
10/2.5/S/TC	Top	10	0	1.34
10/1.6/S/TC	Top	10	0	1.27
10/1.6/F/Tce	Top	10	0	0.98

Table 5.10:  $f_{b,r}$  value for corroded specimens with zero surface crack

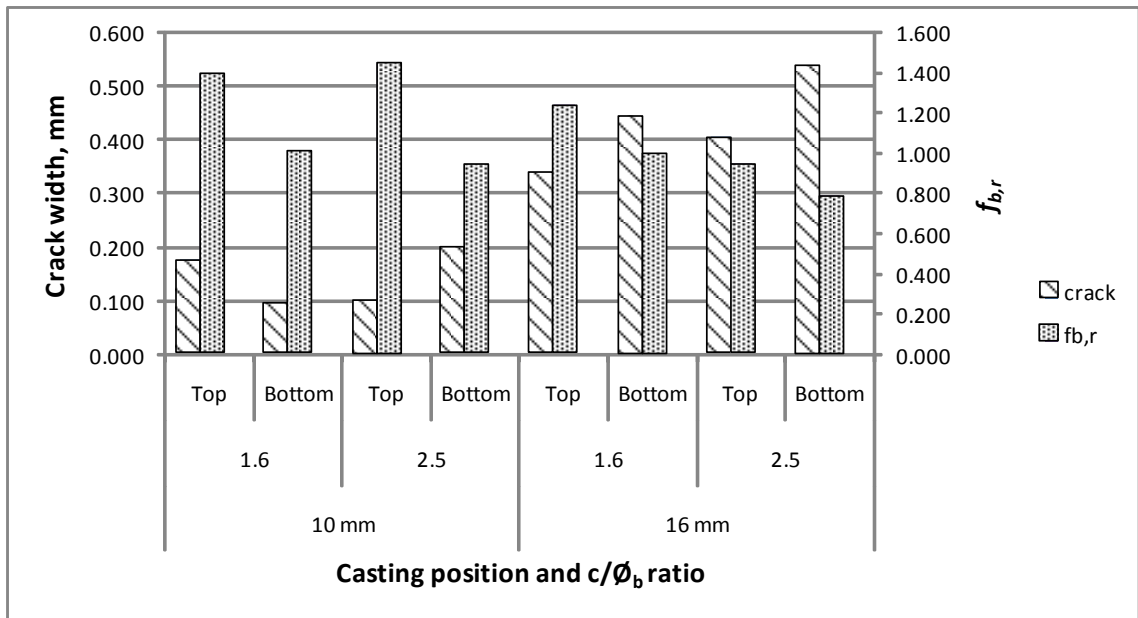


Figure 5.33: Average crack width versus average  $f_{b,r}$  value for  $c/\phi_b$  ratios of 1.6 and 2.5

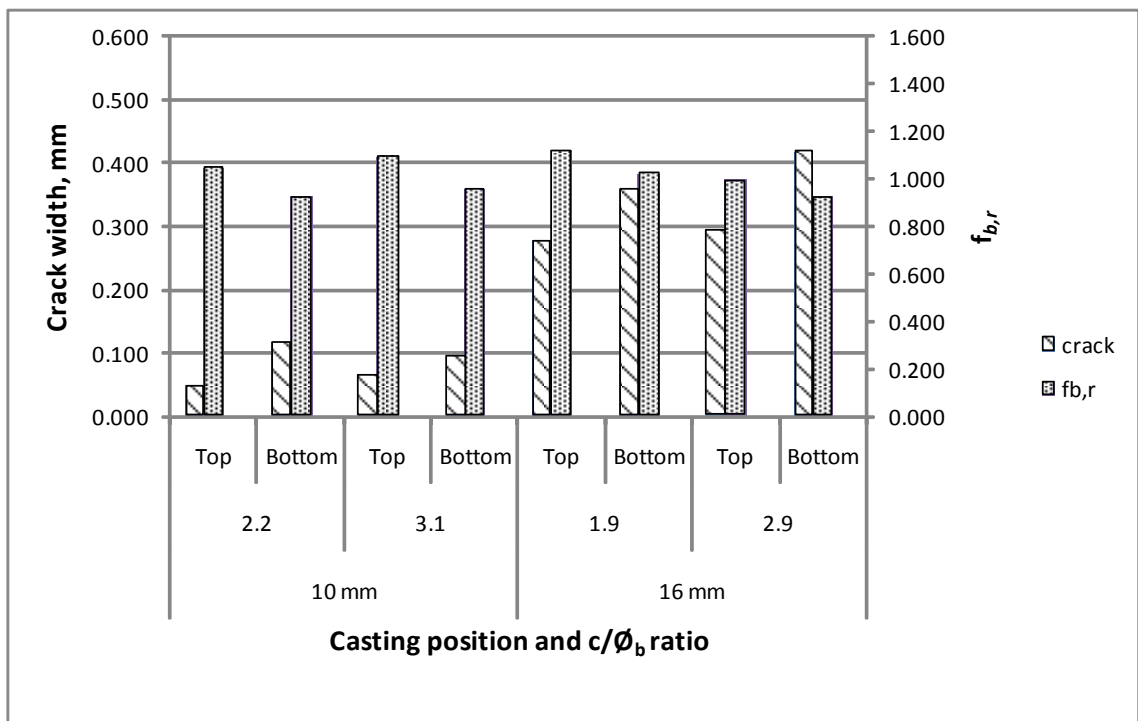


Figure 5.34: Average crack width versus average  $f_{b,r}$  value for various  $c/\phi_b$  ratios

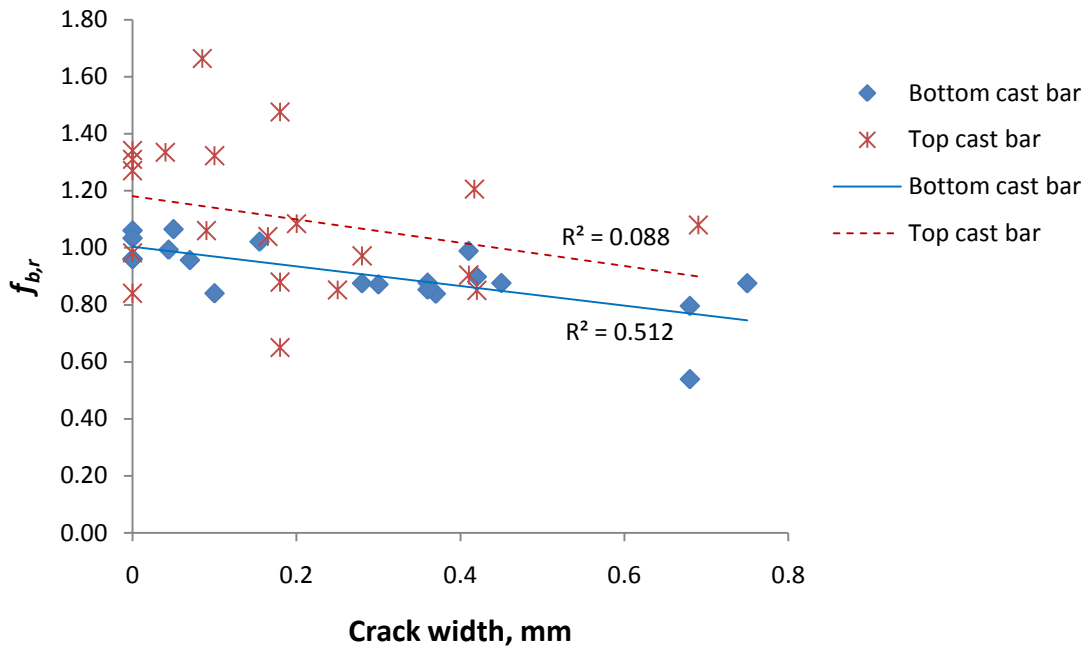


Figure 5.35:  $f_{b,r}$  versus crack width for the bottom and the top cast bar

#### 5.4 Summary of Experimental Results

This chapter discussed the results from the experimental work on the total of 60 beam end-type specimens. Impressed current combined with dry and wet cycles was used in corrosion conditioning of the main reinforcing bar. The average current efficiency varied from 56% to 128%, which reflected the difference between actual and predicted mass loss. The corrosion levels of the reinforcing bars varied from 2.64% to 11.7% of the section loss.

On the basis of the average gravimetric measurements of corrosion, most of reinforcing bars at the top-cast position, regardless of the impressed current, experienced higher corrosion, as measured by the section loss, than those at the bottom-cast position.

The average surface crack width along the bottom cast bars was wider than that along the bars at the top-cast position, with ratios of 1.3 and 1.2 for 10 and 16 mm diameter bars, respectively. The bars at the corner location had wider cracks than those at the centre location for a given corrosion penetration. Wider crack width was observed for the specimens corroded under a “fast” current compared with those corroded under a “slow” current. The latter trend is consistent for both bar locations.

The corrosion penetration correlated better than the percentage of section loss with the width of corrosion-induced cracks.

Bond strength for control uncorroded specimens increased with an increase in the cover-to-bar-diameter ratio. The bars at the bottom-cast position developed higher bond strength than those at the top-cast position, and the bond strength of centrally-located bars was higher than that of the corner bars.

Both corrosion measurements used in this study did not correlate well with the residual bond strength. In some cases, in particular for bars at the top-cast position, corrosion led to an increase in the bond strength compared to uncorroded control specimens.

There is a reasonably good linear correlation between the bond strength and the width of corrosion-induced crack along bottom-cast reinforcing bars. With an increase of the crack width the bond strength decreased. No such correlation has been observed for top-cast bars.

## 5.5 References

- [5.1] P.S. Chana, *A test method to establish realistic bond stresses*, Magazine of Concrete Research, **42**, 151, 83-90 (1990)
- [5.2] J.G. Cabrera, *Deterioration of concrete due to reinforcement steel corrosion*, Cement and Concrete Composite, **18**, 47-59 (1996)
- [5.3] K.K. Aligizaki, *Concrete cover cracking as a function of rebar corrosion: Theoretical and experimental studies*, International Corrosion Conference Series, Corrosion 2006, 063341-0633410 (2006)
- [5.4] Y. Auyeung, P. Balaguru and L. Chung, *Bond behavior of corroded reinforcement bars*, ACI Materials Journal, 87, 2, 220-231 (1990)
- [5.5] T. Vidal, A. Castel and R. Francois, *Analyzing crack width to predict corrosion in reinforced concrete*, Cement and Concrete Research, 34, 165-174 (2004)



- [5.6] I. Khan, R. Francois and A. Castel, *Prediction of reinforcement corrosion using corrosion induced cracks width in corroded reinforced concrete beams*, Cement and Concrete Research, **56**, 84-96 (2014)
- [5.7] D. Coronelli, K. Hanjari and K. Lundgren, *Severely Corroded RC with Cover Cracking*, Journal of Structural Engineering, **139**, 2, 221-232 (2013)
- [5.8] Y. Zhao, J. Yu, B. Hu and W. Jin, *Crack shape and rust distribution on corrosion-induced cracking concrete*, Corrosion Science, **55**, 385-393 (2013)
- [5.9] BS EN 1992-1-1, Eurocode 2: Design of concrete structures – Part 1-1: general rules and rules for building, London: British Standard Institution (2004)
- [5.10] J. Rodriguez, L.M. Ortega and J. Casal, *Corrosion of reinforcing bars and service life of reinforced concrete structures: Corrosion and bond deterioration*, International Conference on Concrete across Borders, Odense Denmark, **2**, 315-326 (1994)
- [5.11] D. Tang, *Influence of chloride-induced corrosion cracks on the strength of reinforced concrete*, Master Engineering Thesis, RMIT University (2007)
- [5.12] T.A. El Maaddawy and K.A. Soudki, *Effectiveness of impressed current technique to simulate corrosion of steel reinforcement in concrete*, Journal of Materials in Civil Engineering, **15**,1, 41-47 (2003)
- [5.13] E. Canbay and R.J. Frosch, *Bond strength of lap-spliced bars*, ACI Structural Journal, **102**, 4, 605-614 (2005)
- [5.14] N.R. Buenfeld and J.P. Broomfield, *Influence of electrochemical chloride extraction on the bond between steel and concrete*, Magazine of Concrete Research, **52**, 79-91 (2000)

## CHAPTER 6 – CONCLUSIONS AND RECOMMENDATIONS

### 6.1 Conclusions

From the analysis of experimental data and the discussion of results, the following conclusions can be drawn:

- (i) On the basis of the average gravimetric measurements of corrosion, most of reinforcing bars at the top-cast position, regardless of the impressed current, experienced higher corrosion than those at the bottom-cast position. A comparison between the actual and theoretical mass losses shows that the effectiveness of impressed current was either lower or higher than 100% even though good control of the current was maintained throughout the test.
- (ii) Casting position produced a significant effect on the width of corrosion-induced cracks. The average surface crack width along the bottom cast bars was wider than that along the bars at the top-cast position, probably, due to differences in the compaction of the top and bottom concrete covers.
- (iii) The selection of impressed current to accelerate the corrosion process should be made with caution, especially when corrosion-induced cracking of the concrete cover is studied. According to the presented experimental results, a higher current rate led to wider corrosion-induced cracks than a slower one. The corrosion penetration correlated better than the percentage of section loss with the width of corrosion-induced cracks.
- (iv) Bond strength on control uncorroded specimens increased with an increase in the cover-to-bar-diameter ratio. Reinforcing bars at the bottom-cast position developed higher bond strength than those at the top-cast position. The bond of 10 mm diameter reinforcing bars was stronger than that of 16 mm diameter bars.
- (v) For both casting positions, the reduction of the bond strength of the corroded specimens was not strongly controlled by the amount of corrosion. Some of corroded top-cast bar specimens had higher bond strength compared to that of similar uncorroded specimens.
- (vi) A good agreement between the crack width and the residual bond strength was observed only for reinforcing bars at the bottom-cast position, where the residual bond strength decreased with an increase in the crack width.

## 6.2 Recommendations for Future Research

- (i) The level of corrosion in tests should be extended beyond 10% of mass loss to further examine the influence of corrosion on residual bond strength.
- (ii) The influence of corrosion-induced crack width on residual bond strength needs to be further studied since the crack width can possibly be used as a control parameter to determine the residual bond strength. It is important to note that the crack width can be easily measured when corrosion occurs in a reinforced concrete structure.
- (iii) The effect of the impressed current rate on the deterioration of reinforced concrete specimens, e.g., residual bond strength, corrosion-induced crack width, etc., needs to be further investigated to improve the credibility of accelerated corrosion tests.
- (iv) An experimental study can be performed to compare the effects of chloride- and carbonation-induced corrosion on residual bond strength.
- (v) Using beam end-type specimens, an experimental study can be undertaken to examine the influence of stirrup corrosion on bond strength.
- (vi) In this research, the numerical analysis is limited only to studying the relationship between the corrosion penetration and the crack width. Further numerical studies can be conducted to investigate the effect of corrosion penetration on bond strength.